

2015

Supercapacitive Swing Adsorption of Carbon Dioxide

Berenika Agnieszka Kokoszka
Lehigh University

Follow this and additional works at: <http://preserve.lehigh.edu/etd>

 Part of the [Chemistry Commons](#)

Recommended Citation

Kokoszka, Berenika Agnieszka, "Supercapacitive Swing Adsorption of Carbon Dioxide" (2015). *Theses and Dissertations*. 2666.
<http://preserve.lehigh.edu/etd/2666>

This Dissertation is brought to you for free and open access by Lehigh Preserve. It has been accepted for inclusion in Theses and Dissertations by an authorized administrator of Lehigh Preserve. For more information, please contact preserve@lehigh.edu.

Supercapacitive Swing Adsorption of Carbon Dioxide

by

Berenika Kokoszka

A Dissertation

Presented to the Graduate and Research Committee

Of Lehigh University

In Candidacy for the Degree of

Doctor of Philosophy

in

Chemistry

Lehigh University

May 18, 2015

©2015 Copyright
Berenika Kokoszka

Approved and recommended for acceptance as a dissertation in partial fulfillment of the requirements for the degree of Doctor of Philosophy

Berenika Kokoszka
Supercapacitive Swing Adsorption of Carbon Dioxide

12/05/2014

Defense Date

04/14/2015

Approved Date

Dissertation Director
Kai Landskron

Committee Members:

Kai Landskron

James Roberts

Dmitri Vezenov

Mark Snyder

ACKNOWLEDGMENTS

Working on the Ph.D. had been a wonderful and often overwhelming experience. It is hard to say whether it had been grappling with the topic itself which had been the real learning experience, or grappling with how to write papers, give talks, work in a group, stay up until the birds start singing, and stay focus.

In any case, I am indebted to many people for making my Ph.D. an unforgettable experience. I would not have been able to complete this journey without the aid and support of countless people over the past five years.

First and foremost I would like to express my special appreciation and thanks to my advisor Professor Kai Landskron, who has been a tremendous mentor for me and whose expertise, understanding, and patience, added considerably to my graduate experience. I would like to thank him for encouraging my research, for allowing me to grow as a research scientist and for providing me with the opportunity to complete my PhD thesis. His advice on both research as well as on my career have been priceless. I appreciate all his contributions of time, ideas, and funding to make my Ph.D. experience productive and stimulating. The joy and enthusiasm he has for his research was contagious and motivational for me, even during tough times in the Ph.D. pursuit. His guidance helped me in all the times of research and writing of this dissertation. Thank you Professor Kai for everything. I could not imagine having a better advisor for my Ph.D study.

I would also like to thank my committee members, Professor Jim Roberts, Professor Dmitri Vezenov and Professor Mark Snyder for serving as my committee members even at hardship. I also want to thank them for letting my defense be an enjoyable moment, and for their brilliant comments and suggestions. Here I would like to especially thank to Professor Jim Roberts whose academic support, input and personal cheering are greatly appreciated. Thank you. I would also like to thank the other two committee members of my proposal defense, Professor Daniel Zeroka and Professor Wojciech Misiolek for their time and great support.

The members of the Landskron group have contributed immensely to my personal and professional time at Lehigh. The group has been a source of friendships as well as good advice and collaboration. I would like to acknowledge honorary group member Cong Liu who was not only my officemate, but also best friend at Lehigh and without who I may not have gotten to where I am today, at least not sanely. His insights and comments were invaluable over the years, and I look forward to a

continuing friendship with him in the future. We've laughed together and he's also been kind when I needed to cry. When others doubted, he remained a fan. When I became too serious, his humor and friendly sarcasm allowed me to laugh and lightened my perspective. In addition, I have been very privileged to get to know Guido Pez. I learned a lot from him about life, research, how to tackle new problems and how to develop techniques to solve them. He was always willing to help and give his best suggestions. A very special thanks also goes out to Dr. Paritosh Mohanty, the group past postdoc, without whose motivation and encouragement I would not have a good start in this group. I could not have wished for a better group.

My gratitude is also extended to Dr. Rebecca Miller. She was one of the first friendly faces to greet me when I began this doctoral program and has always been a tremendous help no matter the task or circumstance. I couldn't have completed all the required paperwork and delivered it to the correct place without her. Thank you Dr. Miller, you shall always be remembered as a smiling face, a warm and friendly heart and one of the few who assisted me in completing my doctoral program.

I must also acknowledge Dr. Aliana Lungu. Her love, support, and belief in me were a treasure. She also gave me many precious memories and made a special place in my heart. Thank you.

The dissertation would not have come to a successful completion, without the help I received from the staff of the Chemistry Department. I am very grateful especially to Jane Derbenwick, JoAnn DeSalvatore, Marge Sawyers and Sharon Zurick who were always so helpful and provided me with their assistance throughout my Ph.D. journey. Thank you for keeping your door open and available for all the times when I needed it, for your support, heart and friendship which I will never forget.

And thank you to all the wonderful people from Lehigh University who have helped me enormously and who I did not mention here.

My Ph.D. study would not have been possible without many people at Warsaw University. The influence of those with whom I worked before coming to Lehigh University is also very important to me. My MS advisors Professors Pawel Kulesza and Dr. Iwona Rutkowska and Professor Jan Augustynski at Warsaw University provided me the great foundations that allowed me to believe in myself and come to US to start and successfully finish my Ph.D. I am also grateful to Dr. Jadwiga Stroka and my friend Ania Dobrzeniecka who were my biggest support during my MS studies at

Warsaw University. Life blessed me with the opportunity to meet my polish best friends Karolina Anczkiewicz and Mariola Lasia. Without their friendship I would feel very lonely. The creativity, determination and sense of joy with which they respond to life's challenges has led me to seek this in others. Even though the ocean separates us, thinking about them always brings a warm smile.

Lastly, I would like to thank my family for all their love and encouragement. For my Mom who raised me by herself with a love of science and supported me in all my pursuits. She has taught me about hard work and self-respect, about persistence and about how to be independent. She is a great role model of resilience, strength and character. She has always expressed how proud she is of me and how much she loves me. I too am proud of her and love her very much. I am grateful for her and for the 'smart genes' she passed on to me. Dziekuje kochana Mamusiu. And most of all I would like to thank for my loving, supportive, encouraging, and patient partner Przemek whose faithful support during the final stages of this Ph.D. is so appreciated. Through his love, patience, support and unwavering belief in me, I've been able to complete this long dissertation journey. He is my biggest fan and supporter. He has taken care of whatever needed tending to without complaining, just so I could focus on completing my dissertation. He has patiently endured many, many long hours alone while I worked on my dissertation. Thank you.

In addition, these acknowledgements would not be complete if I did not mention my 1 and a half year-old son, Nathan who was born before this dissertation was completed. He has been a twinkle in my eye since he was born and this dissertation I dedicate to him. Thank you for not only being such a good little baby that past nineteen months, and making it possible for me to complete what I started but also for helping me to realize that working on my thesis should not be the most important thing that I was doing in my life. You are my biggest love Nathanku.

Table of Contents

List of Figures.....	xi
List of Tables.....	xvi
List of Abbreviations.....	xvii
List of Appendices.....	xviii
Abstract.....	1
Chapter 1 Introduction.....	2
1.1. Global warming and CO ₂ level in atmosphere	2
1.2. Flue gas composition	3
1.3. Carbon Capture & Sequestration(CCS).....	4
1.3.1. Post-combustion CO ₂ Capture (PCC).....	6
Chapter 2 Literature review on carbon capture technologies.....	9
2.1. Chemical Absorption of CO ₂	9
2.1.1. Amine-based Chemical Absorption (Amine Scrubbing)	10
2.1.2. Aqueous Ammonia-based Absorption.....	15
2.1.3. Carbonate-Based Systems.....	18
2. 2. Physical Adsorption of CO ₂	19
2.2.1. Criteria for adsorbents used for CO ₂ capture.....	21
2.2.2. Pressure Swing Adsorption.....	24

2.2.3. Temperature Swing Adsorption.....	27
2.2.4. Electric Swing Adsorption.....	30
2.3. Disadvantages of current carbon capture technologies.....	31
Chapter 3 Theory of Supercapacitors.....	34
3.1. Introduction to Supercapacitors and their principles and properties.....	34
3.1.1. Basic scientific principles and construction of an EDLC.....	36
3.1.2. Concept of Electrical Double Layer (EDL).....	40
3.1.3. Electrolytes for SCs.....	47
3.2. What is activated carbon (AC).....	48
Chapter 4 Characterization methods.....	53
4.1. Physicochemical characterization.....	53
4.1.1. Gas adsorption-desorption technique.....	53
4.1.2. Scanning Electron Microscopy (SEM).....	61
4.1.3. Transmission electron microscopy (TEM).....	64
4.2. Electrochemical characterization.....	68
4.2.1. Cyclic Voltammetry (CV).....	70
4.2.2. Galvanostatic Charge-Discharge (GCD).....	73

Chapter 5 Introduction to Supercapacitive Swing Adsorption (SSA)	76
5.1. The origin of SSA.....	76
5.2. The main hypotheses of SSA.....	79
5.3 Advantages of SSA.....	83
Chapter 6 Materials, reagents and experimental setup	85
6.1. Materials and chemicals.....	85
6.2. Experimental setup for the SSA experiments.....	85
6.3. Preparation of electrodes for the SSA experiments.....	88
6.4. Equipment used for the characterization of the prepared electrodes	89
Chapter 7 Results of the SSA experiments	93
7.1. SSA effect during CV and GCD experiments.....	93
7.2. SSA effect at different potentials.....	102
7.3. Reproducibility of the SSA effect.....	107
7.4. SSA effect vs. reverse-charging of the working electrode.....	108
7.5. The influence of electrode infiltration on the SSA effect.....	111
7.6. Scalability of the SSA effect	113
7.7. The gas selectivity of the SSA effect.....	115
7.8. Dependence of the SSA effect on CO ₂ partial pressure.....	121
7.9. SSA effect in thermodynamic equilibrium.....	123

7.10. SSA effect at different temperatures.....	125
7.11. Possible mechanisms for SSA.....	127
Chapter 8 Summary and Conclusions	
8.1. Summary.....	130
8.2. Results of SSA experiments vs. hypotheses of SSA	131
8.3. Conclusions	132
References	135
Appendix	
Appendix A.....	150
Appendix B.....	155
Vita	157

LIST OF FIGURES

Figure 1.1. Schematic of CO₂ capture processes and systems.....5

Figure 1.2. Process technologies for post combustion CO₂ capture.....7

Figure 2.1. A general scheme for an absorption process.....10

Figure 2.2. MEA absorption benchmark process.....13

Figure 2.3. Conceptual design of an ammonia-based carbon capture process.....17

Figure 2.4. Scheme of PSA.....25

Figure 2.5. Pressure effect on adsorbate loading.....26

Figure 2.6. Scheme of TSA.....28

Figure 2.7. Temperature effect on adsorbate loading.....29

Figure 3.1. Hierarchical classification of supercapacitors.....35

Figure 3.2. Electrostatic capacitor topology.....37

Figure 3.3. Representation of a symmetric EDLC in its charged state.....39

Figure 3.4. Scheme of the electrical double-layer: a) Helmholtz model, b) Gouy-Chapman model, and c) Stern model.....43

Figure 3.5. Electrode electrolyte interface at a negatively charged pore.....44

Figure 3.6. Electrode electrolyte interface at a positively charged pore.....	45
Figure 3.7. Typical distribution of charges at the interface and its electrode potential before and after charging.....	46
Figure 3.8. A double layer model including layers of solvent.....	47
Figure 3.9. Schematic representation of the microstructure of activated carbons.....	49
Figure 3.10. Schematic representation of an activated carbon granule.....	50
Figure 4.1. The IUPAC classification of isotherms.....	54
Figure 4.2. Types of hysteresis loops.....	56
Figure 4.3. Schematic illustration of SEM setup.....	64
Figure 4.4. Schematic illustration of TEM setup.....	68
Figure 4.5. Comparison of cyclic voltammograms of various capacitors.....	72
Figure 4.6. Typical charge and discharge curves for a supercapacitor.....	74
Figure 5.1. Preliminary design for electric field swing adsorption (EFSA) cell.....	77
Figure 5.2. Scheme of the hypothesized SSA mechanism.....	82
Figure 6.1. Custom made glass pressure cell used for SSA experiments.....	87
Figure 6.2. Schematic illustration of an SSA cell.....	88
Figure 6.3. A photo of the Autosorb-1 instrument at Lehigh University.....	90

Figure 6.4. A photo of the Hitachi 4300SE/N microscope at Lehigh University.....	90
Figure 6.5. A photo of the JEOL JEM-2000FX microscope at Lehigh University.....	91
Figure 6.6. A photo of the Gamry Potentiostat model 3000 at Lehigh University.....	92
Figure 7.1. Pressure changes observed during CV experiments at different scan rates a) 1 mV/s, b) 0.2 mV/s, c) 0.05 mV/s.....	95
Figure 7.2. CV curves for the 3.7 g BPL carbon monoliths in asymmetric configurations.	97
Figure 7.3. Pressure changes observed during cathodic GCD experiments at different constant current a) 10 mA, b) 2mA.....	98
Figure 7.4. Pressure changes observed during anodic GCD experiments at 10 mA constant current.....	101
Figure 7.5. Pressure changes at different voltages a) 0.53 V, b) 0.77 V, c) 1.02V and d) 1.22 V.....	102
Figure 7.6. Pressure changes during subsequent repetitions of the same experiment.....	107
Figure 7.7. Pressure changes observed during anodic charging with the constant voltage power supply.....	109
Figure 7.8. Pressure changes observed during cathodic-anodic half cycles.....	110
Figure 7.9. Pressure changes observed for 3.7 g BPL carbon monoliths after being used for a longer time.....	111

Figure 7.10. Comparison of pressure changes during GCD experiment at 2 mA constant current within 0 V to 1 V potential range done at different times: a) 2 nd day of experimental setup, b) 23 rd day of experimental setup.....	112
Figure 7.11. Pressure changes for three different masses of electrodes: a) 0.2 g, b) 3.7 g and c) 7.5 g.....	113
Figure 7.12. Pressure changes during GCD (cathodic) at 2mA constant current within 0V to 1.20V potential range.....	117
Figure 7.13. Pressure changes during 1 hour cathodic half cycles in pure N ₂	119
Figure 7.14. Pressure changes during 1 hour cathodic half cycles in pure He.....	120
Figure 7.15. Pressure changes during 1 hour cathodic half cycles in pure CO ₂	122
Figure 7.16. Pressure changes in thermodynamic equilibrium for 15% CO ₂ and 85% N ₂ gas mixture gas mixture	123
Figure 7.17. Pressure changes in thermodynamic equilibrium in pure CO ₂	124
Figure 7.18. Pressure changes at different temperatures.....	126
Figure A1. N ₂ isotherm of BPL carbon at 77 K.....	151
Figure A2. CO ₂ adsorption isotherm for BPL HSAC electrodes at three different temperatures.....	151
Figure A3. TEM images of BPL carbon.....	152

Figure A4. Cyclic Voltammetry curves for electrodes with different masses of HSAC..153

LIST OF TABLES

Table 7.1. Adsorption of CO ₂ depending on voltage value.....	105
Table 7.2. Change in gas composition during SSA experiment with 3.7 g and 7.5 g electrodes.....	116
Table 7.3. Change in gas composition during SSA experiment with 7.5 g electrodes....	118

LIST OF ABBREVIATIONS

- SSA: Supercapacitive Swing Adsorption
- EIA: Energy Information Administration
- IPCC: Intergovernmental Panel on Climate Change
- CCS: Carbon Capture & Sequestration
- PCC: Post-combustion CO₂ Capture
- PSA: Pressure Swing Adsorption
- TSA: Temperature Swing Adsorption
- ESA: Electric Swing Adsorption
- MEA: Monoethanolamine
- AC: Activated Carbon
- DL: Double Layer
- EDLC: Electrochemical Double Layer Capacitor
- SC: Supercapacitor
- HSAC: High Surface Area Carbon
- IL: Ionic Liquid
- SEM: Scanning Electron Microscopy
- TEM: Transmission Electron Microscopy
- CV: Cyclic Voltammetry
- GCD: Galvanostatic Charge-Discharge
- ESR: Equivalent Internal Series Resistance

LIST OF APPENDICES

Appendix A - compositional, structural and electrochemical characterization of the prepared BPL carbon pellets and monoliths

Appendix B – Calculations of the relationship between pressure and composition change

Abstract

Carbon capture is essential for reduction of carbon dioxide (CO₂) pollution from flue gas which is emitted during fossil fuel combustion. The flue gas is mainly composed of 15% CO₂ and 85% N₂ and it requires high selectivity for gas purification. Some methods have been developed for carbon capture such as Pressure Swing Adsorption (PSA) and Temperature Swing Adsorption (TSA). Unfortunately, these techniques use a lot of energy during the desorption step that reduces power generation efficiency. An ideally effective carbon capture technique needs to promote CO₂ adsorption and desorption at the proper times during the separation cycles, without incurring a large parasitic energy load. A new gas adsorption technique is presented, Supercapacitive Swing Adsorption (SSA), in which CO₂ is either actively adsorbed or desorbed by repeated capacitive charge and discharge of supercapacitor carbon electrodes and energy used in adsorption can principally be recovered upon desorption. It is shown that reversible adsorption/desorption of CO₂ from a 15% CO₂ and 85% N₂ gas mixture can be achieved when an electrically conducting high surface area porous carbon material is brought into contact with carbon dioxide gas and an aqueous sodium chloride electrolyte. When the supercapacitor carbon electrodes are charged, the electrolyte ions are spontaneously organized into an electric double layer at the surface of each porous carbon electrode. The presence of this double layer leads to reversible, selective adsorption and desorption of the CO₂ as the supercapacitor is charged and discharged. Moreover, it is also shown that SSA has the ability to separate CO₂ from N₂, with a high selectivity for CO₂ and only a weak dependence on the CO₂ partial pressure in a CO₂/N₂ gas mixture. The amount of adsorbed CO₂ scales with applied voltage and with the mass of the porous carbon sorbent, which is inexpensive, robust and environmentally friendly. The effect barely depends on temperature.

1. Introduction

1.1. Global warming and CO₂ level in atmosphere

With the rapid increase of the global population and the industrialization of more and more countries, the consumption of energy is explosively growing. It is expected that the world energy consumption will grow by 56 percent between 2010 and 2040 according to the Energy Information Administration (EIA) [1]. Currently over 85% of the global energy demand is being supported by the burning of fossil fuels (coal, oil and natural gas) [2]. The reasons for this skewed reliance on fossil fuels as the primary energy source is due to the inherent energy density, abundance, and the economic dependence of modern society on the acquisition and trade of these resources. Fossil fuels will continue to play an important role in the future, mainly in power generation and industrial manufacturing. The burning of these fossil fuels releases large amounts of flue gases including carbon dioxide (CO₂) into the atmosphere, which causes long-range environmental problems [3]. Consumption of fossil fuels produces nearly 30 Pg (petagrams) of carbon dioxide annually. About three-fourths of the increase in atmospheric carbon dioxide is attributed to burning of fossil fuels [3]. Carbon dioxide is one of the greenhouse gases that enhances radiative forcing, a measure of the influence a factor has in altering the balance of incoming and outgoing energy in the Earth-atmosphere system [3]. The term “Greenhouse Effect” was first coined by French physicist Joseph Fourier in 1824. The greenhouse effect is the absorption of infrared radiation by the atmospheric gases resulting in the trapping of heat, which results in heating of Earth’s surface [4].

Greenhouse gases include carbon dioxide (CO₂), water vapor (H₂O), ozone (O₃), methane (CH₄), nitrous oxide (N₂O), and chlorofluorocarbons (CFCs) [3]. Since the beginning of

the industrial period, the concentrations of the anthropogenic greenhouse gases (CO_2 , CH_4 , N_2O , CFC-11 (CCl_3F) and CFC-12 (CCl_2F_2)), have increased. Of those gases, CO_2 is the principal greenhouse gas of interest because of “its large current greenhouse forcing, its substantial projected future forcing, and its long persistence in the atmosphere” [5].

The amount of carbon dioxide has risen by more than a third since the industrial revolution from 280 parts per million (ppm) by volume to 368 ppm in 2000 [2], and 388 ppm in 2010 [2]. According to the Intergovernmental Panel on Climate Change (IPCC) [3], the atmosphere may contain up to 570 ppm of carbon dioxide in 2100 causing a rise of approximately 1.9°C in the mean global temperature, and an increase of 3.8 m in the mean sea level [6]. Therefore reducing anthropogenic CO_2 emission and lowering the concentration of greenhouse gases in the atmosphere has quickly become one of the most urgent environmental issues of our age.

1.2. Flue gas composition

Flue gases refer to the emissions of combustion product gases resulting from the burning of fossil fuels such as coal, oil, and natural gas that exits to the atmosphere *via* a “flue” which may be a pipe, channel or chimney [7].

Typically, more than two-thirds of the flue gas is nitrogen since ambient air contains about 75 volume percent of gaseous nitrogen (N_2) [7]. The next largest part of the flue gas is carbon dioxide (CO_2) which can be as much as 3% to 30% volume percent of the flue gas according to the respective industrial facilities [7]. It also contains water vapor (H_2O) created by the combustion of the hydrogen in the fuel with atmospheric oxygen. Much of the “smoke” seen exiting from flue gas stacks is this water vapor forming a fog cloud as it

contacts cool air and condenses into water droplets. The flue gas may also contain a small percentage of air pollutants such as particulate matter, carbon monoxide (CO), nitrogen oxides (NO_x), sulfur oxides (SO_x) and mercury [7]. The nitrogen oxides are derived from the nitrogen in the ambient air as well as from any nitrogen-containing compounds in the fossil fuel. The sulfur oxides are derived from any sulfur-containing compounds in the fuels. The particulate matter, sometimes termed black carbon, is composed of very small particles of solid materials and very small liquid droplets which give some flue gases their smoky appearance [7].

1.3. Carbon Capture & Sequestration (CCS)

In general, there are several approaches that can be adopted to reduce the total carbon dioxide emission into the atmosphere such as a reduction in energy intensity (Total Primary Energy Consumption per Dollar of gross domestic product (GDP) [1]) by the efficient use of energy, a reduction of carbon intensity (metric tons of CO₂ emitted for each unit of energy supplied [1]) by using alternatives to fossil fuels such as hydrogen and renewable energy, and enhancement of carbon dioxide sequestration by developing new carbon capture technologies [8]. From the three approaches above, the most promising approach is carbon capture from point source emissions such as power plants.

According to the IPCC Carbon Capture and Sequestration (CCS) is a “*process consisting of the separation of CO₂ from industrial and energy-related sources, transport to a storage location and long-term isolation from the atmosphere.*”[9]

It is expected that by the time of 2020, the number of operational CCS projects is estimated to be 100 globally, which will grow to over 3000 by 2050 [10]. Carbon Capture and

Sequestration encompasses the removal and sequestration of CO₂ from industrial low CO₂ level containing streams, the generation of high concentrated CO₂ streams, and the transport and storage of compressed CO₂. In this context, it should be noted that CCS is more suitable and economically feasible for large point sources – fossil fuel or biomass energy facilities, natural and synthesis gas production, refineries, steel or cement plants – than for small, dispersed emission sources.

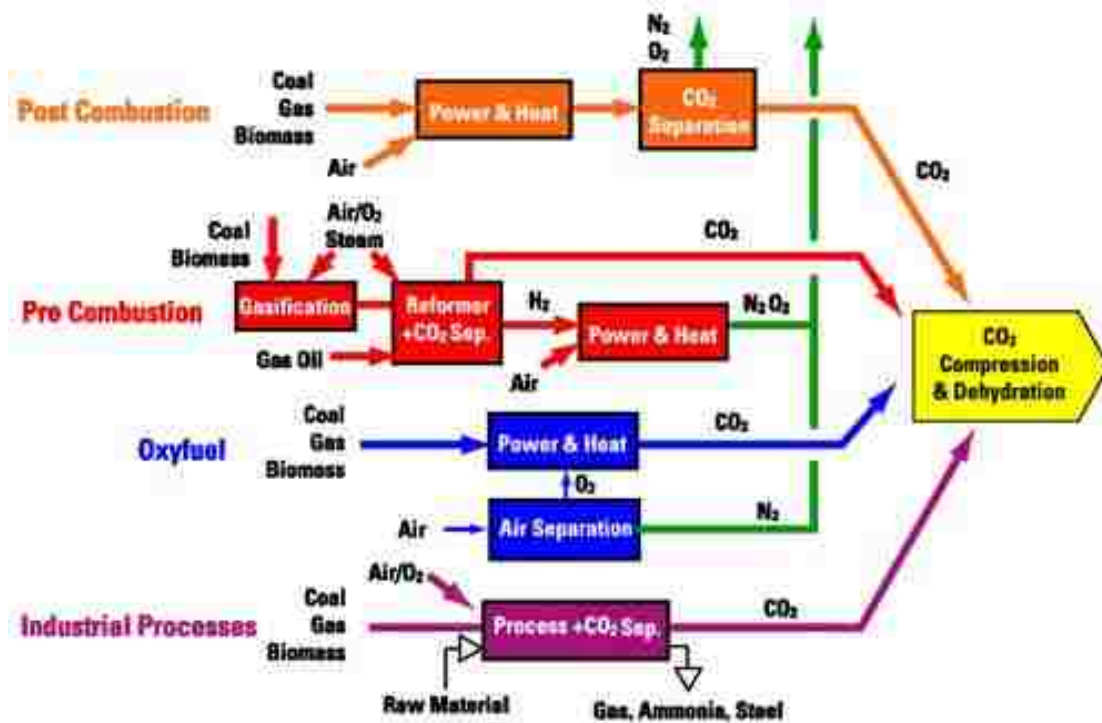


Figure 1.1. Schematic of CO₂ capture processes and systems [9].

Currently, three types of CCS processes are being developed that could be applied to industries with large CO₂ emissions. A schematic representation of every capture system is illustrated in Figure 1.1. The primary fuel (coal, natural gas, oil or biomass) in *pre-combustion* systems undergoes a process of partial oxidation to form syngas and finally produces separate streams of CO₂ for storage and hydrogen (H₂) which is used as a fuel.

Oxyfuel combustion is still in the demonstration phase and needs more investigation. High purity oxygen is used to combust with fuels instead of air. This results in producing the flue gas with H₂O and high CO₂ content that is readily captured, however, at the cost of increased energy requirement in the separation of oxygen from air. *Post-combustion* is basically used to sequester CO₂ from flue gases produced by the combustion of a primary fuel. Compared to other options, post-combustion capture of CO₂ is more economically favored for existing power plants because retrofitting existing plants with post-combustion CO₂ capture is expected to be easily conducted and associated with relatively little cost, while an integrated power plant system would suggest more profound adjustment [10]. Several techniques to capture CO₂ in post-combustion power plants are under scope. The most studied one is amine scrubbing [11-14]. Also, Pressure Swing Adsorption (PSA) [15-17], Temperature Swing Adsorption (TSA) [18] and Electric Swing Adsorption (ESA) [19] deserves more attention.

1.3.1. Post-combustion CO₂ Capture (PCC)

Current anthropogenic CO₂ emission from stationary sources comes from combustion systems such as power plants, cement kilns, steel and iron production plants. For these large-scale processes, the direct combustion of fuel with air in a combustion chamber has been the most economic strategy to make use of energy contained in the fuel. Therefore, the practical importance of the post-combustion capture systems becomes evident when confronted with the reality of today's CO₂ emission sources.

This method involves the removal of carbon dioxide from the combustion reaction product stream, the flue gases, before emission to the atmosphere. Post-combustion CO₂ Capture is a downstream process and is an extension to the flue gas treatment process for NO_x and

SO_x removal. However removal of carbon dioxide is more challenging because of its relatively higher quantities in the gas stream (typically 5-15% v/v, depending on the fuel being used) [2], low partial pressure of carbon dioxide in the flue gas, and relatively high temperature of flue gases [20]. Despite these challenges, PCC is a promising technique because it can be retrofitted to existing units [21].

There are several technologies for post-combustion carbon dioxide capture which can be categorized as conventional or new emerging technologies. These include: (a) adsorption; (b) physical absorption; (c) chemical absorption; (d) cryogenics separation and (e) membranes. Figure 1.2 shows classification of various separation technologies available for post combustion capture.

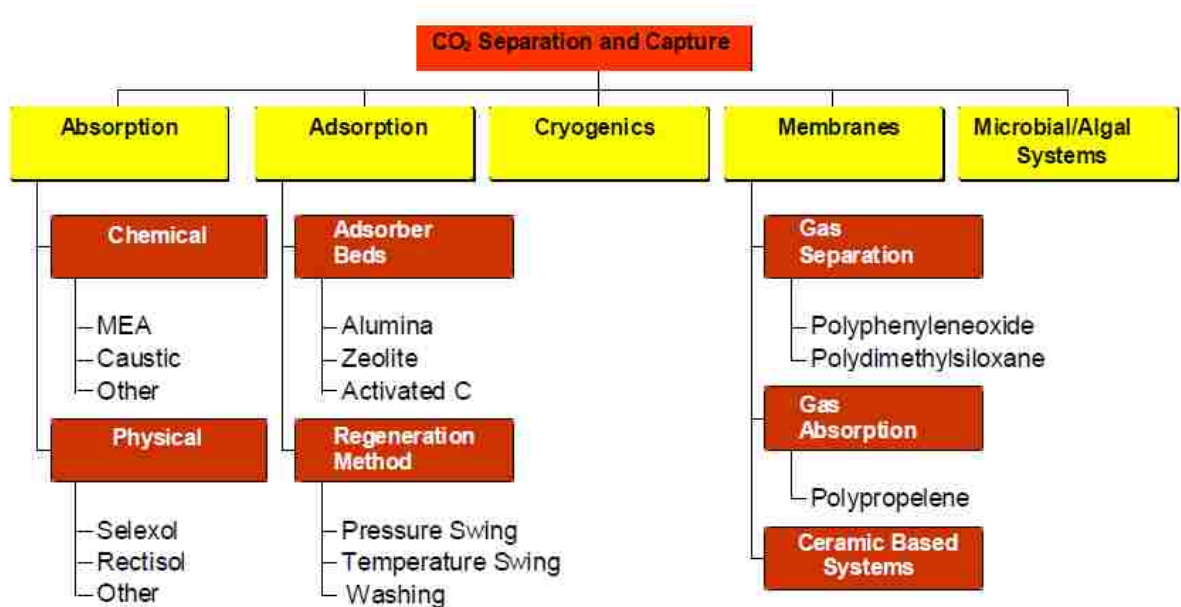


Figure 1.2. Process technologies for post combustion CO₂ capture [22].

Among these technologies, chemical absorption using aqueous alkanolamine solutions is proposed to be the most applicable technology for CO₂ capture before 2030 [23]. At this point in time, chemical absorption offers high capture efficiency and selectivity, and the

lowest energy use and costs when compared with other existing post-combustion capture processes. Gas separation based on adsorption, in which the selection of an adsorbent is the key for CO₂ separation, has also been well developed. These two techniques will now be further discussed in more detail in Chapter 2. Moreover, there is a lot of research on membranes for CO₂ separation, both in natural gas processing and also for CCS application. The use of membranes in natural gas processing is growing and they have an especially strong position in offshore platforms because of the smaller size of the membrane system as well as various other advantages [24]. However, for PCC applications which have a fairly low CO₂ content, no membrane technology seems to be able to compete with for example amine systems what has been the conclusion of several studies [25-27].

There is also physical absorption where solvent combines less strongly with CO₂ than a chemical solvent. The absorptive capacity of these solvents increases with external gas pressure and decreases with temperature. Hence, CO₂ can be separated from such solvents mainly by reducing the pressure in the desorber, significantly reducing the energy requirements in the desorption process. The main physical solvents that could be employed are cold methanol (Rectisol process), dimethylether of polyethylene glycol (Selexol process), propylene carbonate (Fluor process) and sulpholane [28]. In physical absorption, CO₂ is physically absorbed in a solvent according to Henry's Law, which means that they are temperature and pressure dependent with absorption occurring at high partial pressures of CO₂ and low temperatures. The solvents are then regenerated by either heating or pressure reduction. The advantage of this method is that it requires relatively little energy, but the CO₂ must be at high partial pressure. Hence, physical absorption is not economical for gas streams with CO₂ partial pressures lower than 15vol%.

2. Literature review on carbon capture technologies.

2.1. Chemical Absorption of CO₂

In absorption methods the gas separation is achieved by putting the flue gas in physical contact with an absorbent which is capable of capturing CO₂ [29]. In PCC applications the gas separation is achieved with absorbents which are able to form chemical compounds with CO₂. Chemical absorption involves the reaction of CO₂ with a chemical solvent to form an intermediate compound which may be regenerated by the application of heat producing the original solvent and a CO₂ stream. The selectivity of this form of separation is relatively high. In addition, a relatively pure CO₂ stream can be produced [9]. More precisely, in this process there is a solvent which can react with CO₂, but not other flue gas components such as N₂. Carbon dioxide is separated from the flue gas by passing the flue gas through a continuous scrubbing system which captures most of the CO₂ while the other gases can pass through. The system consists of an absorber and a desorber (see Figure 2.1 [29]). Absorption processes utilize the reversible chemical reaction of CO₂ with an aqueous alkaline solvent, usually an amine. When all CO₂ is captured, the sorbent with the CO₂ is taken to another vessel (called the desorber). In the desorber, the absorbed CO₂ is stripped from the solution and a pure stream of CO₂ is sent for compression while the regenerated solvent is sent back to the absorber. The CO₂ is released by a chemical reaction (chemical desorption) or by a change in temperature or pressure (physical desorption). Then the CO₂ is removed from the process and can be processed further and the sorbent can be recycled in the same way as before. However, a small part of the solvent is always destroyed and degraded, which means that a little solvent has to be added and a little removed. Because the absorption process is exothermic, the desorption process requires energy to be added

to the system what leads to the main energy penalty on the power plant. In addition, energy is required to compress the CO_2 to the conditions needed for storage and to operate the pumps and blowers in the process. Optimal conditions for an absorption process are low temperature and high pressure [23]. One example for an absorption process is amine scrubbing, which is discussed in more detail.

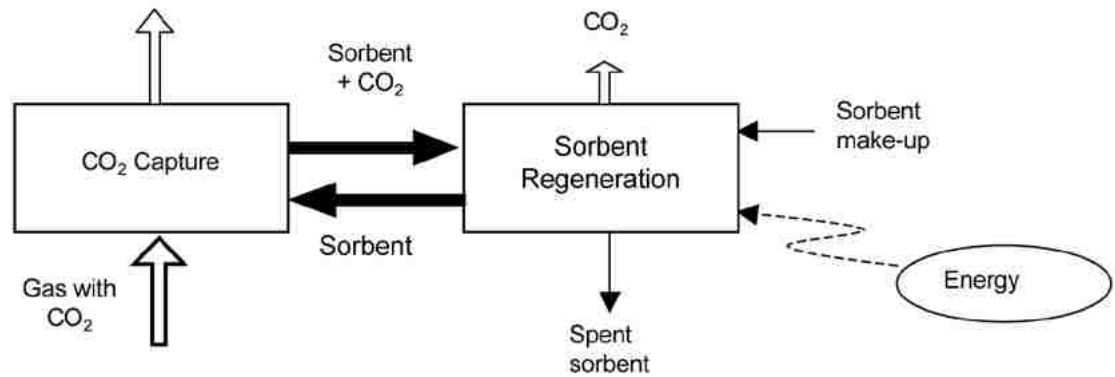


Figure 2.1. A general scheme for an absorption process [29].

2.1.1. Amine-based Chemical Absorption (Amine Scrubbing)

At this moment the most developed and well known acid gas treating processes are amine-based. Rao and Rubin [22] show that amine based CO_2 absorption systems are the most suitable for combustion based power plants: for example, they can be used for dilute systems and low CO_2 concentrations, the technology is commercially available, it is easy to use and can be retrofitted to existing power plants. Amine scrubbing refers to a number of commercial technologies that use various primary, secondary or tertiary alkylamines to remove acidic components including CO_2 or H_2S from gas mixtures [30]. Amines are chemical derivatives of ammonia (NH_3), in which at least one of the hydrogen atoms has been replaced with a chain of carbon and hydrogen atoms, such as an alkyl or aryl group

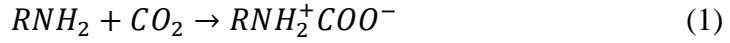
[31]. Most of the amines which can be used for PCC and other carbon dioxide removal processes are alkanolamines containing at least one hydroxyl group (-OH) and one amino group (-NH₂, -NHR or -NR₂) in which R denotes the alkyl group that can replace a hydrogen atom attached directly to the nitrogen. In general, the hydroxyl group serves to reduce the vapor pressure and increase the water solubility, while the amino group provides the necessary alkalinity in water solutions to cause the absorption of acidic gases, such as CO₂. Amine absorbers (scrubbers) are commercially available as large scale technologies for post-combustion separation of carbon dioxide from flue gases. Amines are available in three forms: primary (two hydrogen atoms attached directly to the nitrogen - including monoethanolamine (MEA), diglycolamine (DGA)), secondary (only one hydrogen atom attached directly to the nitrogen - including diethanolamine (DEA), di-isopropylamine (DIPA)), and tertiary (no hydrogen atoms - including triethanolamine (TEA) and methyl-diethanolamine (MDEA)) [31]. Each of them possesses advantages and disadvantages. Primary amines are usually the most alkaline. Different amines have different reaction rates with respect to CO₂ and other acid gases. In addition, different amines vary in equilibrium absorption characteristics for the various acid gases and have different sensitivities with respect to solvent stability and corrosion factors. For example, to enhance the reaction rate, primary amines are most preferable followed by secondary then tertiary [31]. For regeneration energy and loading capacity the most preferred type would be tertiary, followed by secondary, and then primary [21]. Generally, primary amines have been the traditional solvent of choice for carbon dioxide absorption and acid gas removal at low partial pressures. The most applied amine for CO₂ capture until now is MEA. Primary amines, like MEA, are very reactive to CO₂, resulting in relatively small capture plants and

very high CO₂ recovery. However, at the same time primary amines are generally more difficult to regenerate.

Historically, separating CO₂ from flue gas started in the 1970s, not because of concern about the greenhouse effect, but as a potentially economic source of CO₂, mainly for enhanced oil recovery (EOR) operations. In the late 1970s and early 1980s, several commercial CO₂ capture plants were constructed in the U.S [32]. Then in September 1996, the first commercial CO₂ absorption facility for CO₂ sequestration started in Norway [32]. All these plants capture CO₂ with processes based on chemical absorption using a MEA-based solvent which is considered the most mature technology.

Currently, amine treatment is still the leading alternative for CO₂ separation in natural gas processing, especially when the gas flows are large, and CO₂ concentration and partial pressure are fairly low [24]. These conditions closely resemble the requirements that a good post-combustion carbon capture technology must meet. It is therefore understandable that amine-based systems are thought likely to play an important role in decreasing the carbon dioxide emission of conventional power plants.

The underlying principle of amine-scrubbing is the exothermic, reversible reaction between a weak acid such as CO₂ and a weak base such as an alkylamine. The flue gas to be treated is contacted by the aqueous alkylamine solution in an absorbing column or vessel in which a soluble salt is formed from the reaction between the CO₂ and the alkylamines and the reaction can be easily reversed, which allows continuous operation [28] In more detail, CO₂ reacts with aqueous MEA primarily by means of an intermediate zwitterion [33]:



The intermediate zwitterion then reacts with another mole of MEA to form a carbamate salt:



This is an exothermic reaction and 72 KJ of thermal energy are released per mole of CO₂ absorbed by the MEA solution. The flue gas, depleted of CO₂, is then released to the atmosphere. The alkylamine solution is recycled to the absorbing unit while the CO₂ is made ready for transportation by dehydrating and compressing it [14]. A schematic of the process is shown in Figure 2.2 [34]. Generally, the unit in which the carbon dioxide is absorbed from the flue gas is called an absorber, and the unit releasing CO₂ is called a desorber or stripper. The operation pressure is close to 1.0 bar and the temperatures in the absorber and stripper are generally in the ranges of 40–60°C and 120–140°C, respectively.

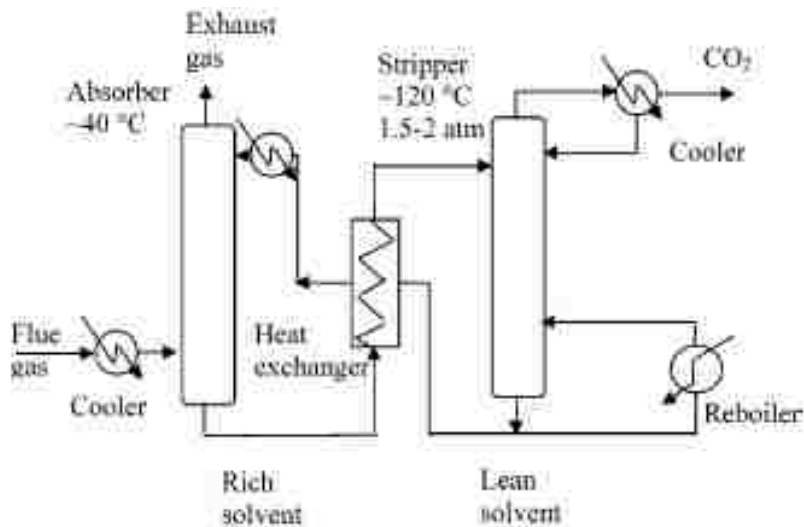


Figure 2.2. MEA absorption benchmark process [34].

The flue gas entering the process at close to atmospheric pressure and required operating temperature of typically 40 - 50 °C is bubbled through a packed absorber column (amine scrubber) containing 25-30% aqueous monoethanolamine (MEA) solution. The flue gas containing CO₂ enters a packed bed absorber from the bottom and contacts counter-currently with a CO₂-lean MEA. The amine absorbs carbon dioxide to form a carbamate species. Flue gas exiting the top of the absorber is washed with water to reduce the entrained solvent droplets and then vented to the atmosphere. Following the absorption process, the rich solvent (high content of carbon dioxide reaction product) passes through a desorber column (stripping column) that operates at 100 - 140 °C and marginally at a higher pressure than the absorber in order to release thermally the carbon dioxide with high purity (over 99%) which may be later compressed for commercial utilization or storage [36]. It has been estimated that up to 80% of total cost in the CO₂ absorption/regeneration cycle is due to the regeneration procedure [12]. After regeneration, the CO₂-lean absorbent is pumped back to the absorber for cyclic use.

Despite the improvements to the amine-based system for post-combustion carbon dioxide chemical absorption, amine scrubbing technologies still have a number of challenges and disadvantages. Some of these disadvantages include that the process in general requires large equipment size and intensive energy input, there is a low carbon dioxide loading capacity, high equipment corrosion rate, and amines are subject to degradation in the presence of oxygen, SO₂, NO₂ and HCl, which makes for additional requirements for solvent recovery and waste stream disposal [2].

Alternate solvents that eliminate or minimize the problems associated with amines are under development. An improved solvent should have higher CO₂ absorption capacity,

faster CO₂ absorption rate, low vapor pressure, high degradation resistance, and low corrosivity. A number of energy efficient proprietary solvents have been studied based on either sterically hindered amines or formulated amines. PSR solvents developed at the University of Regina, Saskatchewan, Canada [37], use proprietary mixtures of simple and hindered amines designed specifically for CO₂ capture from flue gas. Compared with MEA, both higher amine concentrations and rich mole/mole loadings are possible. Key features claimed are lower regeneration temperature, lower solvent circulation rate and reduced degradation and corrosion. One of the advantages of the PSR solvent is its flexibility, i.e., its various ingredients enable it to be optimized to meet the needs of specific tasks. The key features of the PSR solvents are lower solvent circulation rate, lower regeneration temperature, lower solvent degradation rate and lower corrosion rate [37].

2.1.2. Aqueous Ammonia-based Absorption

Although the processes based on chemical absorption with MEA or diethanolamine (DEA) are the most widely used technology for the capture of CO₂ from flue gas, they are still too expensive in the absence of regulations requiring CO₂ capture for large-scale applications such as the sequestration of CO₂ from power plants. The aqueous ammonia-based absorption process is similar in operation to the amine systems. However, the reaction of ammonia and its derivatives with CO₂ has the advantage of having a lower heat of reaction than the equivalent amine based reactions, what results in significant energy efficiency improvements and cost reductions compared to an amine based absorption system [21].

Ammonia (NH₃) is a chemical compound consisting of nitrogen and hydrogen, and it is widely used in the fertilizer and other chemical industries and also as a refrigerant and a

cleaning or neutralizing agent. It is in fact, one of the most important chemicals produced in the world, not only financially but also because ammonia and its derivatives play a vital role in the food production chain as fertilizers [38]. The large production volumes mean that ammonia is cheap compared to the alternative chemicals for carbon dioxide absorption. In CO₂ capture, ammonia systems work similarly to the amine-based systems [21].

The application of aqueous ammonia as an absorption agent, as used e.g. in natural gas conditioning was declining in the end of the 20th century. However, recently processes based on this solvent are regaining interest as a possible substitute for aqueous MEA based processes for CO₂-capture from flue gas. The reasons for this are the claimed advantages of aqueous ammonia over e.g. MEA, when applied as a solvent for flue gas treatment. Potentially, the aqueous ammonia process has a higher loading than MEA, is less corrosive, not sensitive to oxygen levels [39] and can also react with SO₂ and NO_x [40] without the need to remove heat stable salts as with MEA. This makes possible the simultaneous capture of all three major acid gases (SO₂, NO_x and CO₂) plus HCl and HF [41] in one capture-installation, which would facilitate or even promote the use of cheap high-sulphur coal for fuelling power plants [42]. Another advantage of the aqueous ammonia process according to some authors is the possibility to produce fertilizers such as ammonium sulphate ((NH₄)₂SO₄) and ammonium nitrate (NH₄NO₃).

This process has been developed by Alston Power Systems and the Electric Power Research Institute (EPRI, United States). The process consists mainly of a packed bed absorber (scrubber) and a solvent regeneration column (Figure 2.3 [43]).

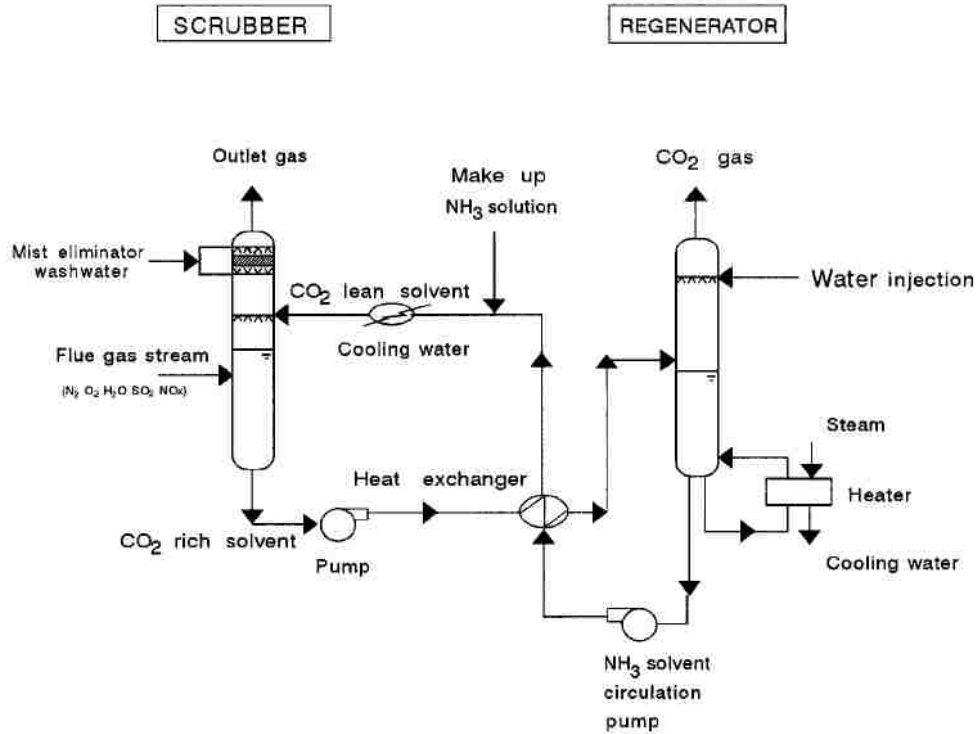
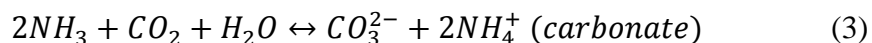
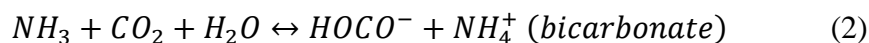


Figure 2.3. Conceptual design of an ammonia-based carbon capture process [43]. The resemblance to Figure 2.2 can be easily seen.

Prior to CO₂ absorption, the flue gas is cooled down using chilled water and a series of direct contact coolers. Then, the flue gas enters the absorber column at near-freezing conditions (0 - 10° C) in which the cooled flue gas flows counter currently to the absorbent slurry (ammonium carbonate and ammonium bicarbonate). When CO₂ is absorbed in aqueous ammonia, the following (overall) reactions between ammonia and carbon dioxide can take place [44]:



The main reason behind the use of a low operating temperature is to allow high CO₂ loading of the solvent slurry and to reduce ammonia slip. In the regenerable aqueous ammonia process, the absorption by-products are thermally decomposed to release CO₂ from the solution of ammonium compounds. The regenerator column operates at temperatures > 120° C and pressures > 2 MPa which produces a high pressure CO₂ stream causing a reduction in the energy requirement for the subsequent compression and delivery of the CO₂ product stream for storage. Although the aqueous ammonia absorption process has many advantages over the conventional amine based absorption process, it is still subject to an extensive development program. There are several drawbacks and concerns regarding aqueous ammonia chemical absorption process such as the high volatility of ammonia (boiling point -33 °C), cooling the flue gas to the 0-10° C range, the limited rate of the reaction between aqueous ammonia and carbon dioxide, the risk of precipitation of some of the reaction products (e.g. ammonium bicarbonate) and loss of ammonia during the regeneration process because of the elevated temperature [45].

2.1.3. Carbonate-Based Systems

Carbonates are salts of carbonic acid (H₂CO₃) and they contain the carbonate ion CO₃²⁻. Carbonate-based carbon capture systems are based on the ability of a soluble carbonate to react with CO₂. This reaction forms bicarbonate which releases the CO₂ when heated, thus reverting to carbonate [21]. In other words, the process is very similar to the amine or ammonia systems described above.

Carbonate systems actually preceded amine systems in CO₂ separation. As early as the beginning of the 20th century, sodium carbonate (Na₂CO₃) solutions were used in dry ice

factories to separate CO₂ from flue gas [46]. However, the introduction of amines for the same purpose led to rapid decline in the use of carbonates. The main reasons were that the CO₂ absorption is faster in amine systems and it is easier to achieve very high removal efficiencies with them. However, the lower total energy requirement for carbonate systems applies even at normal pressure and temperature, which has led to renewed interest in carbonate systems in recent years. The heat of reaction of CO₂ absorption by aqueous sodium carbonate is only a third of the heat of reaction for MEA [46]. Several additives to increase the CO₂ absorption rate, such as amines, glycine and arsenious acid, usually referred to as promoters or activators, were discovered in the 1930s [47]. Carbonates also have other advantages because they are environmentally safe, non-volatile and do not degrade. Despite some promising test results, overall development of carbonate systems for PCC applications still lags behind that of amine systems [21].

2.2. Physical Adsorption of CO₂

As discussed in the previous sections there are several challenges and shortcomings in terms of the recent carbon capture technologies. Therefore, there is a crucial need for developing an alternative capture technology that can both lower the operation cost and have significant advantages for energy efficiency.

Adsorption, in general can be defined as a process in which the molecules or atoms of a single or multi-component fluid system in liquid, gas or even a super-critical phase tends to concentrate at the surface of a solid, under the effect of intermolecular interactions among fluid (adsorbate) and solid (adsorbent). The difference between absorption and adsorption is that in adsorption the adsorbed molecules remain on the surface of the sorbent

whilst in absorption the absorbed component enters into the bulk of the solvent or a solid to form a solution. If the strength of the interactive forces between the adsorbent and fluid system is very strong, resulting in an electron transfer driven bonding, the phenomena is called chemisorption or chemical adsorption. On the other hand physisorption, or physical adsorption results when the surface forces between the adsorbent and the adsorbate are rather weak and involve only weak-natured electrostatic interactions. There are several former works that explain this phenomenon in detail [48-63]. The adsorption can be affected by changing either the pressure (Pressure Swing Adsorption, PSA) or the temperature (Temperature Swing Adsorption, TSA), i.e., the degree of adsorption increases with pressure and decreases with temperature and these two processes are further discussed in the following paragraphs.

An adsorbent is a material to which different gases are attracted with varying degrees. These materials take the form of very high surface area porous pellets or beads. In general, adsorbents used for CO₂ capture from flue gas can be a physisorbent and chemisorbent. The physisorbents for CO₂ capture mainly include activated carbon, alumina, metallic oxides, metal-organic frameworks (MOFs) and zeolites [64-67]. The chemisorbents, mainly refer to a few solid adsorbents obtained through the incorporation of specific functional groups (mainly amine functionalized adsorbents) resulting in enhancing chemical reaction effect between CO₂ molecules and adsorbents but chemical adsorption is generally undesirable in CO₂ capture as the bonds are too strong to be easily broken by for example pressure change [68].

Adsorption systems operate in a three step cycle: adsorb CO₂, during which the preferentially adsorbed species (CO₂) are picked up from the feed, purge (remove impure

gases) and evacuate (remove/desorb CO₂), during which the adsorbed species are removed from the adsorbent, thus "regenerating" the adsorbent for use in the next cycle. This process is very similar to that described in Figure 2-1. Adsorption processes possess potential advantages compared to the other capture technologies (i.e. chemical absorption processes) including less regeneration energy required, greater capacity, and selectivity and ease of handling.

2.2.1. Criteria for adsorbents used for CO₂ capture

Because adsorption occurs on the surface of the adsorbent, the quantity of material adsorbed is directly related to the area of surface available for adsorption, and the usual adsorbents are prepared in such a way as to have a large surface area per unit weight. The most important characteristic of a sorbent is, in fact, the quantity of sorbate that a given quantity of sorbent can hold at the operating temperatures and pressures. As the CCS application requires that CO₂ is separated from the flue gas, which is a mixture of gases, it is equally important that the sorbent is selective for CO₂. In other words, the adsorbent needs to adsorb plenty of CO₂ but it should not adsorb much of any of the other gases [2]. More precisely, a suitable adsorbent for CO₂ capture from flue gas should satisfy several important criteria to compete with the present technologies, including [68, 69]:

- 1) high CO₂ adsorption capacity (loading) – simply stated, it is the amount of adsorbate taken up by the adsorbent , per unit mass (or volume) of the adsorbent; the CO₂ equilibrium adsorption capacity represented by its adsorption isotherm is a very important criterion in order to evaluate new adsorbents in terms of the capital cost of the capture system. With the knowledge of the adsorption equilibrium

capacity the amount of the adsorbent required can be obtained, and consequently the volume of the absorber vessels. The suitable adsorbent for CO₂ capture from flue gas should at least exhibit a CO₂ adsorption capacity of 2 - 4 mmol/g at ambient pressure [68];

- 2) high selectivity for CO₂ - the adsorption selectivity of the adsorbent is defined as the ratio of the CO₂ capacity to other bulk gas components (i.e. N₂ and O₂) what is one of the main properties of adsorbent material, because it has a direct impact on the purity of the CO₂ captured;
- 3) fast adsorption/desorption kinetics - a good adsorbent should exhibit fast adsorption/desorption kinetics under the operating conditions. Fast kinetics may not only shorten the cycle operation time, but also to some extent reduce the amount of solid sorbents needed to capture a given volume of flue gas;
- 4) the stability during repeated adsorption/desorption cycling - stability is a crucial property of an adsorbent because it determines the life time of the adsorbents and the frequency of their replacement. An ideal sorbent is expected to be used under real flue gas environment for hundreds of thousands of operation cycles without significant performance deterioration. On one hand, CO₂ capture sorbents should retain the appropriate working capacity and selectivity during their whole lifetime in order to reduce the frequency of material replacement. On the other hand, the sorbents should demonstrate enough structural and morphological strength to persist under operating conditions, such as high volumetric flow rate of the flue gas, vibration, and temperature and mechanical abrasion. A good adsorbent should

tolerate the presence of moisture and other impurities in the feed (i.e. water vapor, O₂ and SO₂).

- 5) mild regeneration conditions - the interaction between CO₂ molecules and porous sorbent media should be in the optimal range, which could be also represented and measured by the heat of adsorption. Heats of adsorption, a measure of the energy required for regeneration, are normally in the range of -25 to -50 kJ/mol for physisorption and -60 to -90 kJ/mol for chemisorption [69]. Too strong bonding results in the higher adsorption capacity at low partial pressure but requires more energy which makes the regeneration difficult and costly;
- 6) low operating cost – cost is the most subtle characteristic to discuss because it may vary from week to week and from sales representative to sales representative, even for the same exact material,

The major physical adsorbents reported for CO₂ adsorption include activated carbons, inorganic porous materials such as zeolites and hydrotalcites [67], but activated carbon (AC) has a number of attractive characteristics over other physical adsorbents, such as its high adsorption capacity, high hydrophobicity, low cost, and low energy requirement for regeneration [70]. Activated carbons present a series of advantages as CO₂ adsorbents: they are inexpensive, insensitive to moisture, have high CO₂ adsorption capacity at ambient pressure and, moreover, they are easy to regenerate, and they have well developed micro and mesoporosities [65, 71-73].

When the adsorbent is put in contact with a flowing gas, an equilibrium state is achieved after a certain time. This equilibrium establishes the thermodynamic limit of the adsorbent loading for a given gas composition, temperature, and pressure [50]. Information about the

adsorption equilibrium of the different species is vital to design and model adsorption processes [64–78]. The time required to achieve the equilibrium state may be also important, particularly when the size of the pores of the adsorbent are close to the size of the molecules to be separated [79-82].

In an adsorption process, the adsorbent used is normally shaped into spherical pellets or extruded. Alternatively, it can be shaped into honeycomb monolithic structures resulting in reduced pressure drop of the system [83]. The feed stream is put into contact with the adsorbent that is normally packed in fixed beds. The less adsorbed component will break through the column faster than the other(s). In order to achieve separation, before the other component(s) breaks through the column, the feed should be stopped and the adsorbent should be regenerated by desorbing the adsorbed compound. Since the adsorption equilibrium is given by specific operating conditions (composition, T (temperature) and P (pressure)), by changing one of these process parameters it is possible to regenerate the adsorbent. Different adsorption methods are often named after the condition which is changed during the process. The two main methods relevant for CO₂ capture are TSA and PSA and the magnitude of the required T or P change, of course, depends on the sorbent used.

2.2.2. Pressure Swing Adsorption

Pressure Swing Adsorption processes are usually employed for gas-solid system exhibiting physisorption, in which both fast adsorption and desorption at the adsorbent surface is realized by changing the pressure levels inside the bed. More precisely, PSA is a technology used to selectively separate a specific gas from a mixture of gases by

microporous or mesoporous solid adsorbents at a relatively high pressure, *via* gas-solid contact in a packed column, in order to produce a gas stream enriched in less strongly adsorbed components of the feed gas [84]. The adsorbed components are then desorbed from the solid by lowering their gas-phase partial pressures inside the column to enable adsorbent re-usability. Desorbed gases, as a result, are enriched in the more strongly adsorbed components of the feed gas (Figure 2.4 [85]). No external heat is generally used for the desorption step. So it can be said that in PSA the total pressure of the system “swings” between high pressure during the feed and low pressure during regeneration [86, 87].

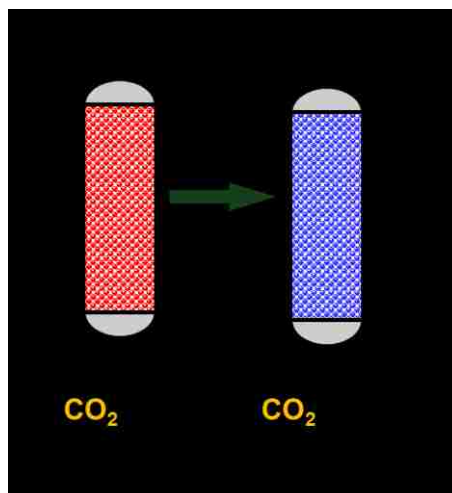


Figure 2.4. Scheme of PSA [85].

Figure 2.5. shows schematically the effect of pressure on the adsorption equilibrium of a single adsorbate. For any given partial pressure of the adsorbate in the gas phase, an increase in pressure leads to an increase in the quantity adsorbed. A relatively modest increase in pressure can cause a relatively large increase in loading.

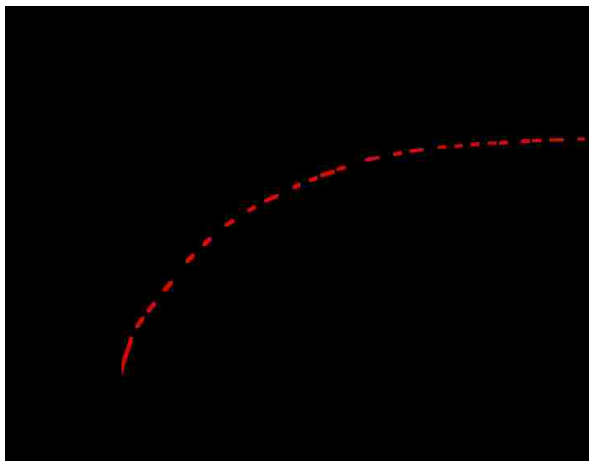


Figure 2.5. Pressure effect on adsorbate loading [85].

While a PSA process carries out adsorption at superambient pressure and desorption at near-ambient pressure level, a vacuum swing adsorption (VSA) process undergoes adsorption at near-ambient pressure, while desorption is achieved under vacuum.

The first patent application in which PSA technology was described, was presented by Charles Skarstrom (Skarstrom cycle) in the 1950s [88]. Skarstrom's apparatus was called the heatless air dryer and was used to remove water vapor from air. The cycle involves only 2 beds (columns) performing the following four basic steps:

1. Cocurrent Pressurization with feed,
2. Adsorption with feed,
3. Countercurrent blowdown
4. Countercurrent purge with product

In this cycle, in the feed step, air is fed to the first column at a pressure higher than atmospheric. The adsorbent initially used (zeolite 5A) was selective to nitrogen, making the exiting stream richer in oxygen. When the adsorbent packed in the first column is

saturated and cannot adsorb more nitrogen, the feed is directed to the second column. In order to release part of the nitrogen adsorbed in the first column, the flow direction is reversed and the total pressure of the column is reduced by venting to atmosphere. In the blowdown step, nitrogen is desorbed from the adsorbent and released and at the end of this step, the gas phase inside the column is rich in nitrogen. To additionally remove nitrogen from the column, a purge step (or light gas recycle) is used. The purge consists of recycled part of the enriched air from the other column which is flowing by the pressure differential between the two columns.

Since the invention of PSA, the process has been applied in many different industries. A PSA system usually comprises two or more adsorbent-filled beds interconnected to each other *via* a network of switch valves, which in turn controls the simultaneous operation of product purification and adsorbent regeneration steps. Therefore, a multiple bed assembly is used to ensure a constant supply of product, while the other beds are in the regeneration mode.

It has been demonstrated that PSA technology can be used not only for CO₂ [15, 89] removal but in a large variety of other applications like hydrogen purification [90-95], air separation [96-104], or noble gases (He, Xe, Ar) purification [105–107] and so forth.

2.2.3. Temperature Swing Adsorption

Temperature Swing Adsorption is another technique used for regenerating a bed of adsorbent that is loaded with a gas mixture. The TSA process is based on adsorption at lower temperature and regeneration at an elevated temperature (Figure 2.6 [85]).

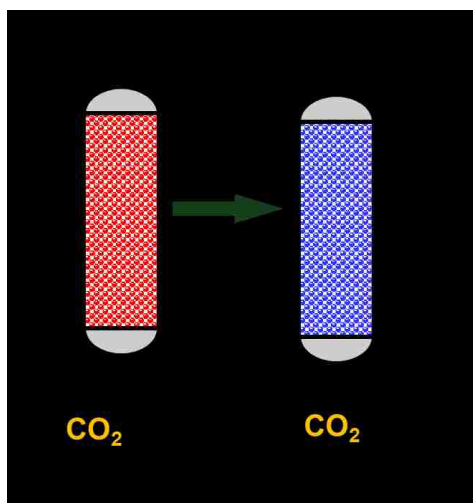


Figure 2.6. Scheme of TSA [85].

A TSA operation usually employs the following three basic steps.

1. Adsorption or production step at low temperature;
2. Heating the bed for desorption of impurities;
3. Cooling the bed back to the adsorption conditions.

The adsorption capacity of an adsorbent at higher temperature is lower than at lower temperatures. The saturated adsorbent is being regenerated at high temperatures of 110-280°C (depending on the required dewpoint, the process parameters, the gas composition and the used material) [18]. There are several possibilities to introduce heat into the adsorber: heating ambient air, heating part of the feed gas, heating part of the product gas, heating a separate inert gas. The regeneration time is in general longer than in PSA. The Figure 2.7 [108] shows schematically the effect of temperature on the adsorption equilibrium (Type I isotherm) of a single adsorbate.

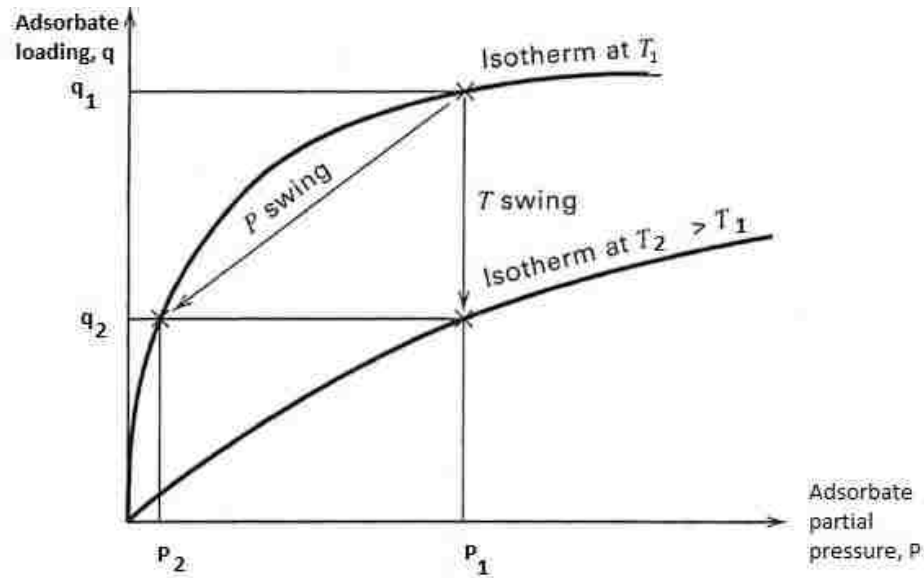


Figure 2.7. Temperature effect on adsorbate loading [108].

For any given partial pressure of the adsorbate in the gas phase, an increase in temperature leads to a decrease in the quantity adsorbed. If the partial pressure remains constant at P_1 , increasing the temperature from T_1 to T_2 will decrease the equilibrium loading from q_1 to q_2 . A relatively modest increase in temperature can effect a relatively large decrease in loading. It is therefore generally possible to desorb any components provided that the temperature is high enough. However, it is important to ensure that the regeneration temperature does not cause degradation of the adsorbents.

The key advantage of TSA over PSA is its ability to separate impurities having a tendency to form strong bonding with the adsorbent (chemisorption) [109]. A major challenge related to the use of TSA is the relative long duration of the processing steps necessary to change the bed temperature as compared to a PSA system. It should be noted that bed pressure transients can be quickly realized in a packed bed by changing the valve settings, while temperature changes require heating the whole mass of adsorbent and metallic wall

requiring hours or even days [110] to complete one cycle, adversely effecting the cycle productivity.

2.2.4. Electric Swing Adsorption

The concept of ESA was initially proposed by researchers at the Oak Ridge National Laboratory [111-113]. The process still consists of an adsorption process and a subsequent desorption process, like a conventional TSA or PSA process. Its unique feature is that in the desorption stage the regeneration is performed by increasing the temperature of the adsorbent using the Joule effect of passing electricity through a saturated electrically-conductive adsorbent (Joule's first law of heating). In fact, regeneration of the adsorbent is carried out by reducing the equilibrium capacity of the materials. In these terms, it seems that the principles of operation of the ESA process are similar with the operation of the TSA, [114]. The in situ heating route can effectively deliver heat to adsorbents without heating the additional media, thus ESA offers several advantages including less heat demand, fast heating rate, better desorption kinetics and dynamics and independent control of gas and heat flow rates as compared with PSA and TSA [115]. On the other hand, the adsorbent employed in ESA experiences large differences in temperature, so significant differences in loading at low and high temperatures are expected what is normally translated to high values of heats of adsorption and maximum performance can be achieved if the concentration of the gas to be adsorbed is small. That is why this process is not suitable for removal of large contents of gas [116].

When an electric current flows through a solid with finite conductivity, electric energy is converted to heat through resistive losses in the material. The heat is generated on the

microscale when the conduction electrons transfer energy to the conductor's atoms through collisions. The heat energy released in a conductor on passing an electric current is called the "Joule heat" and effect is called the 'Joule effect'. Joule's first law of heating states that: "The heat produced per unit time, on passing electric current through a conductor at a given temperature, is directly proportional to the square of the electric current" [117]. The Joule effect within a column can be obtained in two different ways. The simplest one uses an adsorbent able to conduct electricity (direct ESA). An alternative is to use a nonconducting adsorbent and introduce some device able to conduct electricity into the column (indirect ESA).

The ESA process is mentioned in several reports as one possible technique to capture CO₂ from flue gases, but so far this process was commercially employed to remove just volatile organic compounds [113,118-122]. Only two technical works report some experimental data on CO₂ capture, both using commercial adsorbents, where one is an activated carbon material [123] and the other one is zeolite 13X [124].

2.3. Disadvantages of current carbon capture technologies

Post combustion capture is based on separation from flue gas, which has low carbon dioxide concentrations. Concentration of CO₂ for coal power plants is about 12 % to 15 %, for coal fired power plants with integrated gasification combined cycle about 9 % and for a natural gas fired power station as low as 4 % to 8 % [22]. These low concentrations are inconvenient for separation and directly handicap some separation methods.

To date, chemical absorption with amines is the only technique that has been used commercially to capture CO₂ from flue gas. Currently there are three electric power

generating stations in the U.S. that capture CO₂ from flue gas and six other major flue gas CO₂ capture facilities worldwide. All nine use MEA as the chemical sorbent [125]. The main disadvantage of MEA is relatively high amount of energy required for regeneration. Possibility of improvement can be brought by sterically-hindered amines which have good absorption and desorption characteristics. The sterically-hindered amines have larger molecules than MEA and improves CO₂ load during absorption. The hindered amine process needs less energy, because solvents consume less heat for regeneration than MEA solvents. Unfortunately, the drawback is in lower reaction speeds than for MEA. Amine based absorption has also problems with an oxidizing environment, which can cause solvent degradation and equipment corrosion. Moreover, amine solvents react with NO₂ or SO_x into stable salts which are irreversible.

The ammonia scrubbing technology possesses many advantages over the conventional MEA process for CO₂ capture, including lower cost, higher capacity and efficiency for CO₂ absorption, lower decomposition temperature of ammonium bicarbonate, and less corrosion to absorber material. However, in addition to the highly volatile nature of ammonia, the lack of a process to regenerate ammonia from its carbonate salts hinders the ammonia scrubbing technique from being applied in practice.

Carbon dioxide capture using solid adsorbents is considered one of the most promising technologies for CCS [21] despite their disadvantages such as low capacity of sorbents and influence of contaminants (SO₂, H₂O) on the separation process. In desorption step there is a need of either pressure or temperature change that makes PSA and TSA inherently energy intensive. Therefore, more energy efficient gas separation technologies are desirable.

This thesis describes a new carbon dioxide adsorption technique, Supercapacitive Swing Adsorption (SSA), which is based on reversible adsorption and desorption of CO₂ by capacitive charge and discharge of electrically conducting porous carbon material and is not based on pressure or temperature changes. This method could potentially reduce the energy load by the applied electric field which drives the adsorption of CO₂ by simply switching the electric bias on and off. Energy invested for adsorption of CO₂ can be recovered during desorption step because SSA relies on reversible capacitive charging and discharging. The process of adsorption and desorption can be constantly repeated because the stationary sorbent can be reused after the CO₂ is released. Chapter 5 describes the SSA process in more details

3. Theory of supercapacitors

3.1. Introduction to supercapacitors and their principles and properties

Supercapacitors (SCs), also known as ultracapacitors or electrochemical capacitors, store energy through the formation of an electrostatic double-layer of electronic and ionic charge accumulated on each side of the electrode/electrolyte interface in response to an applied potential [126,127]. Most batteries undergo chemical changes or phase transitions upon charge/discharge which degrade performance over several hundred to several thousand cycles. In contrast, Electrochemical Double Layer Capacitors (EDLCs) require only the physical re-arrangement of electronic and ionic charge with little to no chemical changes and can typically be cycled over a million times with little performance degradation. They are not limited by reaction kinetics and solid-state mass transport, as is typically the case for batteries, enabling EDLCs to be charged and discharged rapidly with nearly 100% efficiency.

Supercapacitors can be divided into two separate types depending on their charge storage mechanism: Electrochemical Double Layer Capacitors (EDLCs) and Pseudocapacitors (Figure 3.1). In the first case, the charge accumulation is achieved electrostatically by positive and negative charges residing on two interfaces. The second type exhibits both pseudocapacitance and double-layer capacitance, wherein pseudocapacitance arises from the fast faradaic redox reaction mechanism at the interface between electrode and electrolyte, or within the electrode itself according to Faraday's laws [126]. There is also a third class of supercapacitors called hybrid capacitors which are fabricated with one electrode forming a double layer (carbon based as the negative electrode) and another electrode having pseudocapacitance (e.g., metal oxide based as the positive electrode).

Since this work was based only on EDLCs, the pseudocapacitors and hybrid capacitors are not further discussed.

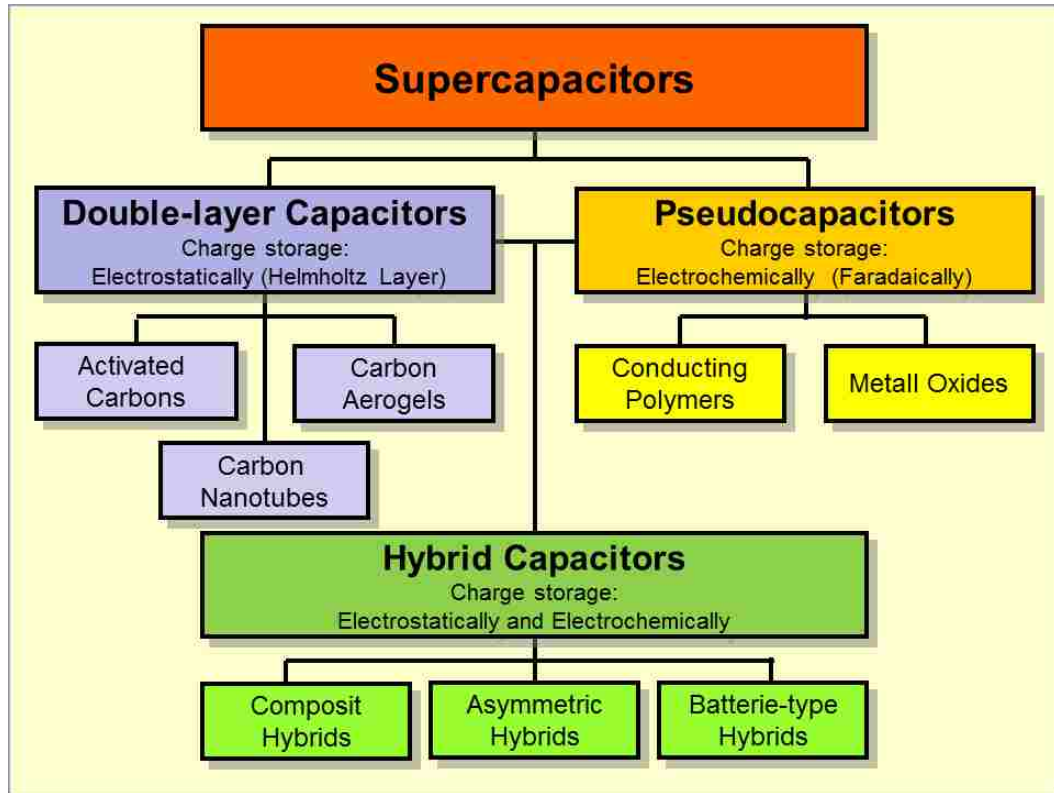


Figure 3.1. Hierarchical classification of supercapacitors [128].

Research activities have been intensified over the decades to identify plausible materials as candidate electrodes for energy storage applications. The priority has been given to high energy, easily available, cheap and environmental friendly materials. In view of the mentioned rationale for choice of materials, activated carbons are the most commonly used electrode material in commercial SCs at present [126]. Carbon in its various forms is currently the most extensively examined and widely utilized electrode materials in EDLCs with development focusing on achieving high surface-area with low matrix resistivity.

Carbons are attractive as electrodes for SCs due to a unique combination of chemical and physical properties, namely [126, 129, 130]:

- High conductivity,
- High surface-area range (~ 1000 to $2000 \text{ m}^2\text{g}^{-1}$),
- Good corrosion resistance,
- High temperature stability,
- Controlled pore structure,
- Processability and compatibility in composite materials,
- Relatively low cost.

The first patent of supercapacitors using porous carbon electrodes in aqueous medium dates back to 1957 by Becker assigned to General Electric [131]. The commercialization of a supercapacitor in aqueous electrolyte actually started in the 1970s by Nippon Electric Company (NEC) [132]. By the 1980s, many companies produced such devices such as Gold capacitor by Matsushita, Dynacap by Elna, PRI ultracapacitor by PRI designed for military applications such as laser weaponry and missile guidance systems, etc. [133, 134]. Since 2000, supercapacitors have effectively permeated industrial applications including automobiles, tramways, buses, cranes, forklifts, wind turbines, electricity load leveling in stationary and transportation systems, etc. [135].

3.1.1. Basic scientific principles and construction of an EDLC

Electrochemical capacitors operate on principles similar to those of conventional electrostatic capacitors. It is therefore instructive to undertake a brief review of electrostatic capacitor operation.

A conventional capacitor stores energy in the form of electrical charge, and a typical device consists of two conducting materials separated by a dielectric (Figure 3.2). When an electric potential is applied across the conductors electrons begin to flow and charge accumulates on each conductor. When the potential is removed the conducting plates remain charged until they are brought into contact again, in which case the energy is discharged. The amount of charge that can be stored in relation to the strength of the applied potential is known as the capacitance, and is a measure of a capacitor's energy storage capability. Equations 3-1 and 3-2 [136] apply to an electrostatic capacitor.

$$C = \frac{Q}{V} = \epsilon \frac{A}{d} \quad \text{Equation 3-1}$$

$$U = \frac{1}{2} CV^2 = \frac{1}{2} QV \quad \text{Equation 3-2}$$

in which C is capacitance in Farads, Q charge in Coulombs, V is electric potential in Volts, ϵ is the dielectric constant of the dielectric, A is conductor surface area, d is dielectric thickness, and U is the potential energy.

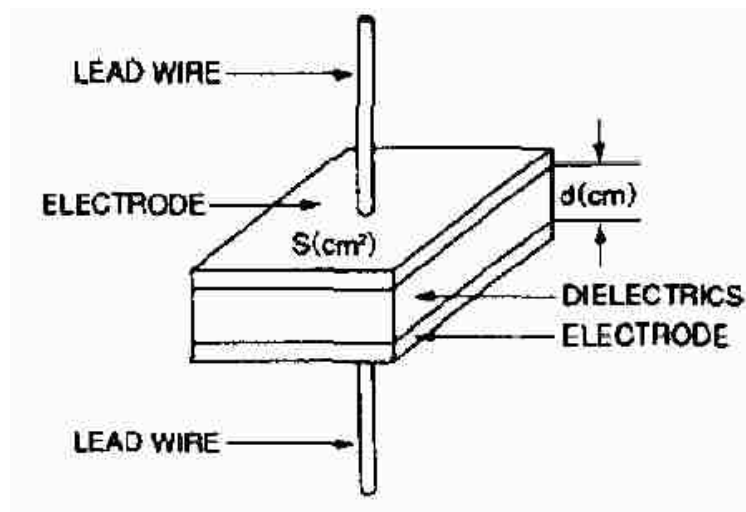


Figure 3.2. Electrostatic capacitor topology [136].

Electrochemical Double Layer Capacitors store electrical charge in a similar manner, but charge does not accumulate on two conductors separated by a dielectric. Instead the charge accumulates at the interface between the surface of a conductor and an electrolytic solution (Figure 3.3). The accumulated charge hence forms an electric double-layer [136].

Figure 3.3 shows the typical configuration of an EDLC, which is symmetric [133]. High specific surface area (SSA), porous carbon electrodes are typically cast onto a metallic current collector. Two such electrodes are sandwiched around an ion permeable membrane that prevents the two electrodes from short circuiting but allows ion migration. If two electrodes are far enough apart to prevent short circuiting the membrane can be omitted. An electrolyte is typically imbibed into the porous carbon electrode. In this case, during operation of the system, the dominant mechanism is the charge/discharge of the electrical double-layer, and the system is called an EDLC. Upon application of a potential difference between the two electrodes, electrons accumulate near the interface of the negatively polarized electrode. The voltage is limited by the stability potential window of the electrolyte. At the same time, holes are generated at the oppositely charged electrode and anions populate the double-layer on the solution side of this interface. To maintain charge neutrality, anions and cations are exchanged across the membrane to balance the charge in each compartment. As schematically illustrated in Figure 3.3, the ions and electric charge on either side of the interface form what is called a double-layer (DL). The separation distance, δ , between these two charged regions is typically on the order of a nanometer, corresponding to the radius of a solvated ion. This region of thickness δ can be thought of as the dielectric layer separating two plates of a conventional parallel plate capacitor. The nanometer-scale charge separation and the use of high specific surface area electrode

materials leads to devices with significantly higher specific capacitance than typical dielectric capacitors. A more detailed description of the structure of this double-layer is given in the next section (3.1.2). The EDL capacitance results from the pure electrostatic attraction between ions and the charged surface of electrodes. The electrode together with the electrolyte and voltage, determines its capacitance and partially its resistance and self-discharge characteristics. The ability to store charge is dependent on the accessibility of the ions to the porous surface-area, so ion size and pore size must be optimal.

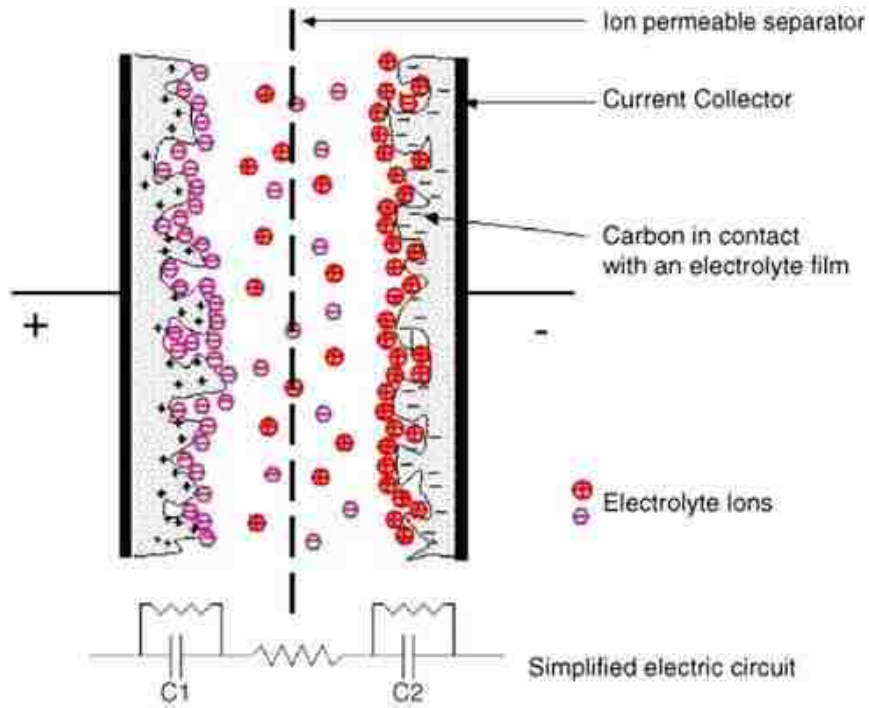


Figure 3.3. Representation of a symmetric EDLC in its charged state [133].

Each electrode/electrolyte interface represents a capacitor and hence the simplified equivalent circuit of the complete device can be represented by two capacitors in series, as shown in Figure 3.3 [133, 137], and the total capacitance (C) expressed by equation 3-3 [138] is essentially controlled by the electrode with the smallest capacitance but the amount

or type of active material in each electrode is often adjusted to obtain matching capacitances:

$$\frac{1}{C} = \frac{1}{C_1} + \frac{1}{C_2} \quad \text{Equation 3-3}$$

Since a double layer forms on each of the two electrodes, a supercapacitor can be thought of as equivalent to two capacitors in series, each with its own capacitance, C_1 and C_2 .

3.1.2. Concept of Electrical Double Layer (EDL)

The distinguishing feature of the supercapacitor device is the electrostatic charging of the electrochemical double layer (EDL). In all capacitors the charge is stored without (ideally) reactions taking place, unless the supercapacitor is of the pseudocapacitive type. The double layer is formed by the separation of charges in the electrolyte and requires the presence of two electrodes accumulating opposite charges (one positive and one negative) to each other.

A double layer is realized when two electrodes immersed in an electrolyte, are polarized. The polarized charges at both the positive and negative electrodes resemble two capacitors connected in series as it was shown in Figure 3.3. The electrical double-layer mechanism, which arises from the electrostatic attraction between the surface charges of activated carbon and ions of opposite charge, plays the major role in carbon/carbon supercapacitors. The understanding of the electrical processes that occur at the boundary between a solid conductor and an electrolyte has developed gradually. Various models have been developed over the years to explain the phenomena observed by chemical scientists.

The first theoretical models for the EDL were developed by Helmholtz in the 19th century. When Helmholtz first coined the phrase “double layer” in 1853, he envisioned two layers of charge at the interface between two dissimilar metals. Later, in 1879, he compared this metal/metal interface with a metal/aqueous solution interface [139, 140]. In this model, the interface consisted of a layer of electrons at the surface of the electrode, and a monolayer of ions in the electrolyte (Fig. 3.4a). As described by Helmholtz in 1853 [139, 140], a charge separation takes place on polarization at the electrode-electrolyte interface with a double layer distance d (Figure 3.4a), leading to a capacitance C (equation 3-4):

$$C = \frac{Q}{V} = \frac{\epsilon_0 \epsilon_r A}{d} \quad \text{Equation 3-4}$$

in which Q is the total charge at the electrode, V is the voltage imposed across the capacitor, A is the specific area of the electrode and electrolyte interface accessible to ions, d is the thickness of the electric double layer, ϵ_0 ($8.854 * 10^{-12} \text{ Fm}^{-1}$) is the permittivity of the free space and ϵ_r is the dielectric constant of the electrolyte. C is the capacitance predicted by the Helmholtz model, and is a constant value dependent only on the dielectric constant and charge layer separation.

Given that the electrode capacitance depends on the reciprocal of the double-layer thickness which is in the order of 10^{-10} m (0.1 nm), and it is directly related to the carbon surface area, typically of several hundreds $\text{m}^2 \text{ g}^{-1}$ of carbon, the capacitance of EDLCs is significantly higher than that of the dielectric and electrolytic ones. The specific capacitance expressed per unit of surface area is typically near $25 \mu\text{F cm}^{-2}$, hence, with large accessible surface area carbon electrodes, high double layer capacitances on the order of $100\text{-}150 \text{ F g}^{-1}$ can be achieved [126]. The charge layer in the electrolyte was first

considered static and the potential profile in the electrochemical double layer decreased linearly with distance from electrode surface.

In the early 1900's, Gouy considered observations that capacitance was not a constant and that it depended on the applied potential and the ionic concentration. To account for this behavior Gouy proposed that thermal motion kept the ions from accumulating on the surface of the electrode, instead forming a diffuse space charge (Fig. 3.4b) [126]. Further work by Chapman in the 1910's on this model developed the idea of distribution of ions in the electrolyte. This model today is referred to as the Gouy-Chapman model. In this model the positive and negative ions are diffused and distributed at a certain distance from the electrode. The Figure 3.4b shows the Gouy-Chapman model and it can be seen that ions were distributed in the solution region. The electric potential in this region decreases exponentially because of the influence of the charge on the electrode reduced by the distance. It can be seen that the change of electric potential becomes higher suddenly near the electrode. This model is also known as the diffusion electrical double-layer. The main weakness with the Gouy-Chapman model was the overestimation of the capacitance value of the electrodes which occurs if the ions are near the electrode surface.

In 1924, Stern overcame this problem by using the analogy of adsorption of ions according to Langmuir at the surface of a solid. Including the hydration shells of ions in the electrolyte solution improved the predictions of his model. By adding the hydration shells to the model, a more accurate geometry (necessary to predict behavior at the interface) was introduced, thus resembling the model seen in Figure 3.4c. As a result, the EDL capacitance (C_{dl}) of the electrode becomes a combination between the Helmholtz/compact double-layer

capacitance (C_H) and the diffusion region capacitance (C_{diff}), and can be expressed as in equation 3-5 [126]:

$$\frac{1}{C_{dl}} = \frac{1}{C_H} + \frac{1}{C_{diff}} \quad \text{Equation 3-5}$$

Stern recognized that the ions in the electrolyte exhibit a certain ionic radius and, therefore, cannot approach the electrode surface closer than their ionic radius allows. This distance of closest approach is called the Outer Helmholtz Plane (OHP).

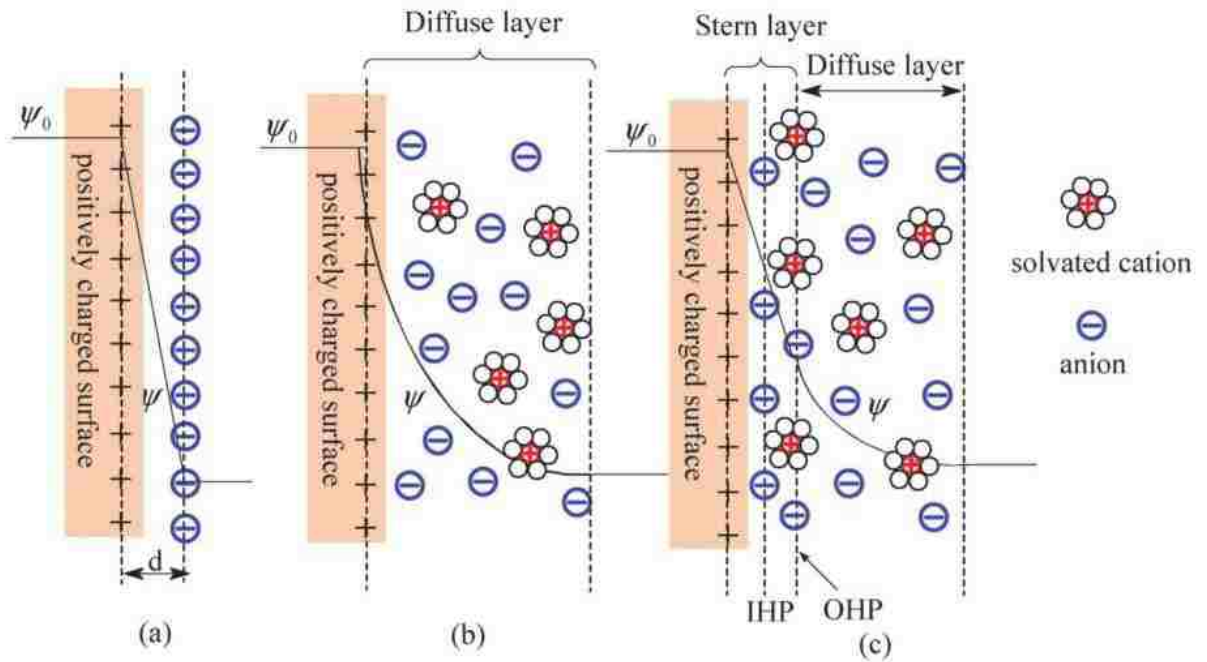


Figure 3.4. Scheme of the electrical double-layer is shown: **a)** Helmholtz model, **b)** Gouy-Chapman model, and **c)** Stern model. IHP and OHP represent the inner Helmholtz plane and outer Helmholtz plane, respectively. d is the double-layer distance described by the Helmholtz model. Ψ_0 and Ψ are the potentials at the electrode surface and the electrode/electrolyte interface, respectively [135].

The Stern layer (Figure 3.4c) consists only of the monolayer of adsorbed solvent on the electrode and hydrated electrolyte ions. This region can be separated into the inner

Helmholtz layer (IHP), which consists of a monolayer of solvent and ions adsorbed on the electrode surface, and the outer Helmholtz layer (OHP), which incorporates the solvated ions of opposite charge. These layer distinctions arise as a result of the different sizes of cations and anions. Anions are usually smaller than the solvated cations and consequently the distance between them and the positive electrode is smaller than the space separating the hydrated cations from the negative electrode. The capacitance at the positive electrode, therefore, is usually twice that of the negatively charged electrode (Figure 3.5 and 3.6). Beyond the Helmholtz regions is a diffuse layer consisting of a distribution of ionic charge [141].

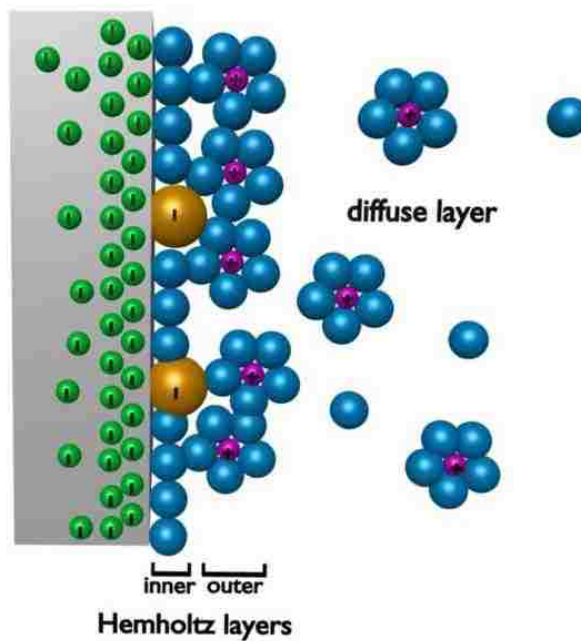


Figure 3.5. *Electrode electrolyte interface at a negatively charged pore [141].*

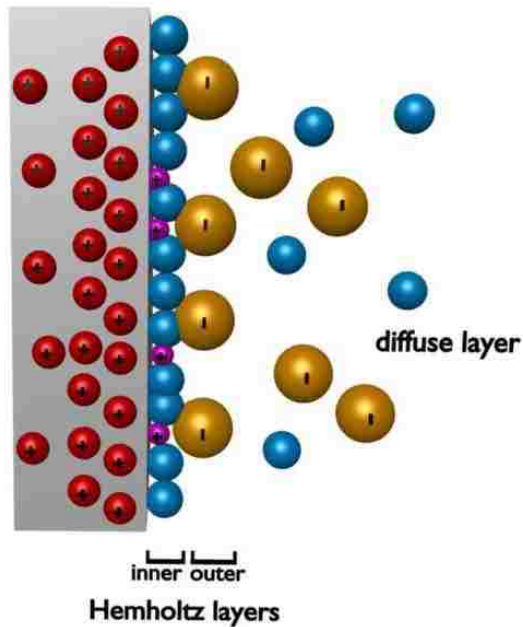
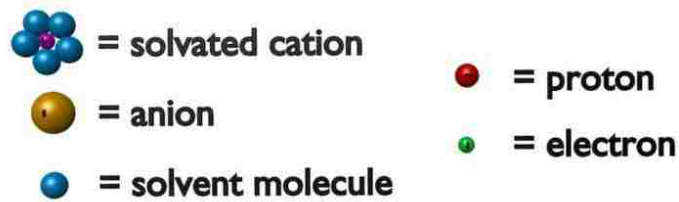


Figure 3.6. Electrode electrolyte interface at a positively charged pore [141].



Theoretically, one electrode and electrolyte interface creates a fully functioning equivalent of a traditional capacitor. Practically speaking, however, there must be two electrodes so that an electric potential may be applied, and there are thus two of these layered regions within a supercapacitor.

The excess charge on the electrode surface is compensated by an accumulation of excess ions of the opposite charge in the solution. This structure behaves essentially as a capacitor as it possesses the double layer. The amount of charge is a function of the electrode potential. Figure 3.7 illustrates the electrode potential before and after charging. The

charges are polarized at the interface forming the Helmholtz layer. Thus an electrical potential can be observed after the charging [126, 129, 130].

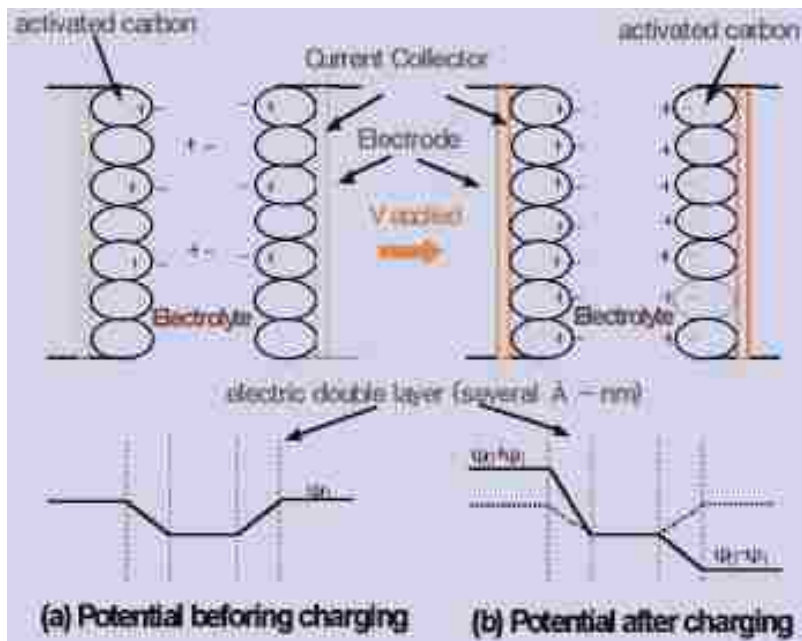


Figure 3.7. Typical distribution of charges at the interface and its electrode potential before and after charging [126].

In 1963 Bockris, Devanathan and Muller proposed a model that included the action of the solvent [142]. They suggested that a layer of water was present within the inner Helmholtz plane at the surface of the electrode. The dipoles of these molecules would have a fixed alignment because of the charge in the electrode. Some of the water molecules would be displaced by specifically adsorbed ions. Other layers of water would follow the first, but the dipoles in these layers would not be as fixed as those in the first layer (Figure 3.8).

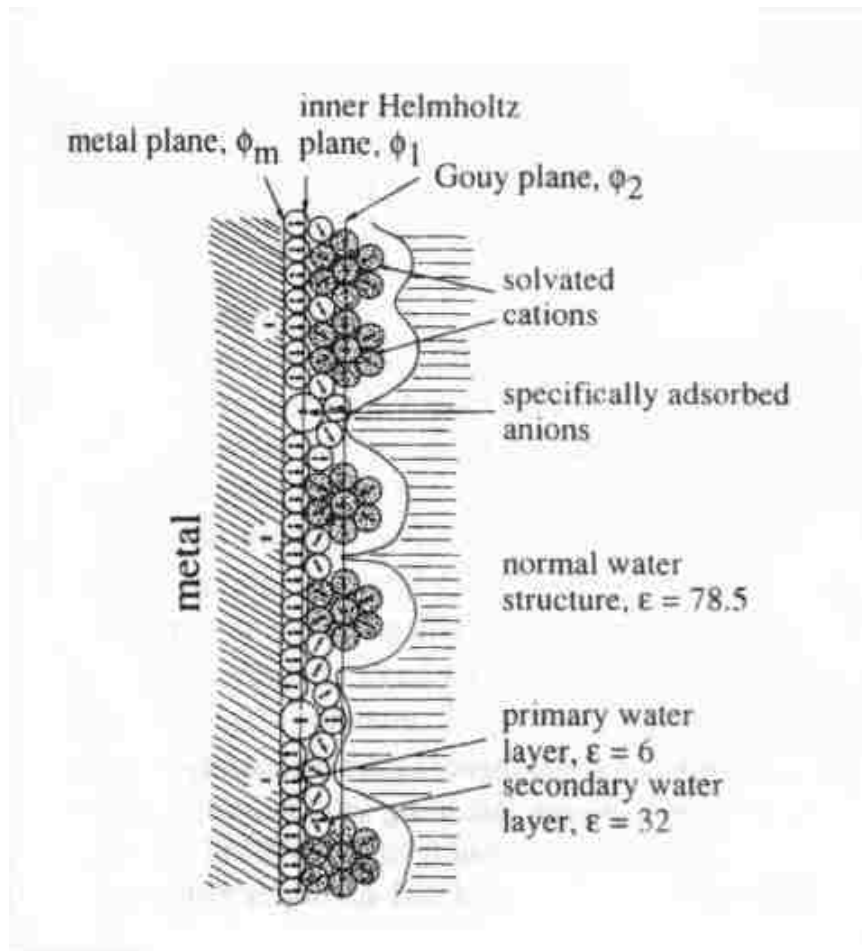


Figure 3.8. A double layer model including layers of solvent [142].

3.1.3. Electrolytes for SCs

The choice of electrolyte in an EDLC is as important as the choice of electrode material. The attainable cell voltage of a supercapacitor will depend on the breakdown voltage of the electrolyte, and hence the possible energy density (which is dependent on voltage) will be limited by the electrolyte. Power density is dependent on the cell's ESR, which is strongly dependent on electrolyte conductivity. There are currently three types of electrolyte in use in EDLCs: aqueous, organic and ionic liquids (ILs).

An aqueous electrolyte has a high ionic conductivity leading to higher power density, but a small electrochemical window (1.2 V) which is restricted by the thermodynamic window

of water. The electrochemical window is the potential window within which the electrolyte is neither reduced nor oxidized at an electrode. Examples of these aqueous electrolytes are commonly H_2SO_4 and KOH . An alternative can be an organic electrolyte which has a bigger electrochemical window (3 V) and higher energy storage capacity, but problems of relatively high resistivity, depletion and toxicity. Examples of these aqueous electrolytes are Propylene Carbonate (PC) and Acetonitrile (ACN) electrolytes [143, 144]. The last ones are ionic liquids composed of organic cations and inorganic anions. Their liquid phase range is large, so is their electrochemical window (6 V) [145, 146]. The problem is their high viscosity which reduces the ions migration rates.

3.2. What is activated carbon (AC)?

Activated carbons are largely utilized not only in commercial EDLCs but also in adsorption of CO_2 because of their low cost. They are typically produced by carbonization of various carbonaceous precursors that are easily acquired, such as coals [147] (e.g. bituminous coal and lignite), fly ashes [148], anthracites [149], and wood or other biomass sources [150] (e.g. bamboo chips, coconut shells, saw dust etc.) [151]. Therefore, activated carbons have a huge advantage over other adsorbents and SC materials in terms of the low cost of raw materials. The activation and treatment process together with the intrinsic nature of different precursors strongly determines the structural characteristics of the resulting activated carbons in terms of pore size distribution, porosity, surface area, as well as pore volume. Figure 3.9 shows a schematic representation of the structure of activated carbons, which gives an idea of how a disordered array of graphene layers, also folded, can be arranged. Activated carbons feature high specific surface area ($>1500 \text{ m}^2 \text{ g}^{-1}$) and are

usually rich in surface functional groups (like hydroxo, keto and carboxylate functionalities) on their pore surfaces.



Figure 3.9. Schematic representation of the microstructure of activated carbons [146].

Figure 3.10 presents a porous network in an AC granule, which includes micropores (lower than 2 nm width), mesopores (between 2 and 50 nm), and macropores (larger than 50 nm) according to the IUPAC classification of pores recommended in 1985 [152]. Most of the adsorption process takes place in the range of micropores, whereas meso- and macropores play very important roles in transporting the adsorbate to the micropores as well as in ionic diffusion [153]. A generalization would be that the micropores are responsible for the largest part of the total surface area with the meso- and macropores contributing less.

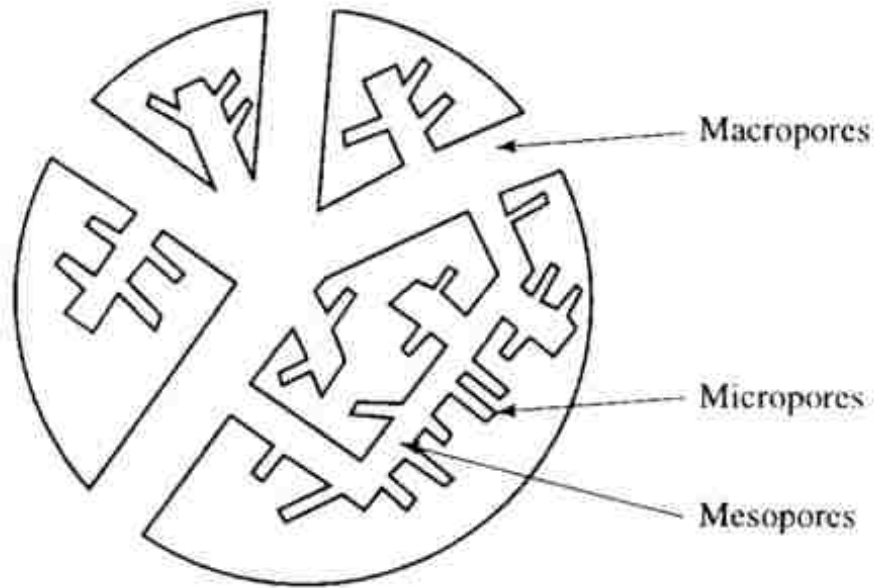


Figure 3.10. Schematic representation of an activated carbon granule [153].

For electrochemical systems these properties of a carbon become significant for the simple reason that electrolyte solutions are used and ions that carry charges have a finite size, depending on which electrolyte solution is used. In aqueous electrolyte solutions the hydration shell of an ion has to be considered as well. For example, a potassium ion, with its accompanying hydration shell has a radius of approximately 5-6 Å (0.5-0.6 nm) [153] and it is thus clear that not all the pores are available for penetration by this ion. Moreover, ACs are relatively hydrophobic materials because of their non-polar C-C and C-H bonds which makes it difficult for water molecules to enter the micropores. On the other hand, the activated carbons have also hydrophilic pores due to polar hydroxo, keto and carboxylate functionalities on their pore surfaces. These hydrophilic pores are filled with the aqueous electrolyte.

The production of activated carbons from raw materials usually consists of two steps: carbonization, and activation [147]. The former step includes heating and thermal

decomposition of the starting materials at a temperature of 500-1200 °C in an inert atmosphere to make carbonaceous materials which have poor surface properties. Therefore, it is essential to follow the carbonization process with an activation step, during which the carbonaceous materials are modified to produce a suitable porosity, and active sites. The activation of the carbonaceous materials can be achieved by either physical or chemical activation.

Thermal or physical activation involves high temperature (700-1100 °C) controlled gasification of carbonaceous precursors in the presence of oxidizing gases such as steam, carbon dioxide, air etc. The oxidizing ambience triggers a controlled burning of volatile materials and carbons to develop high surface area and porosity. The degree of activation is solely controlled by carbonization temperature and duration. Very aggressive activation is avoided as it incurs huge carbon burn-off, low carbon yield, low density and pore widening [154].

On the other hand, chemical activation is conducted at lower temperatures (400-800 °C) involving chemical activating (dehydrating) agents e.g. potassium hydroxide, phosphoric acid, zinc chloride etc. The activating agent penetrates into the precursor and comes out during activation creating huge porosity and surface area. The final morphology of carbon can be easily tuned by controlling the amount of activating agent, carbonization temperature/duration, heating rate etc. [155]. Chemical activation is widely used to produce exceptionally high surface area carbon (>2500 m²/g).

The solid matrix of an electrode acts as a carrier of electrons during the charging and discharging of a SC. Therefore it is highly desirable that there are as few limitations as possible in this matrix. The resistivity, ρ , corresponds to the conductivity, κ , as $\rho = \kappa^{-1}$. In

active carbons this property can vary greatly. Since graphene layers constitute the bulk of active carbons (hexagonal sheets of carbon) the conductivity of the carbon is dependent on the orientation of these sheets. The conductivity can therefore vary by several orders of magnitude [156]. Furthermore, it may be affected by activation treatments such as chemical oxidation, extent of porosity, composition and heat treatment.

4. Characterization methods

Proper characterization of electrode materials was necessary to gain understanding of the specific compositional, structural and electrochemical aspects which are responsible for the SSA results obtained. Thus, several techniques were employed to address this challenge and are described below.

4.1. Physicochemical characterization

Physical characterization techniques assist in evaluating the chemical and morphological properties of the constructed electrodes. There are many physicochemical methods that exist but in this work the gas adsorption-desorption technique, scanning electron microscopy and transmission electron microscopy were used and are further discussed below.

4.1.1. Gas adsorption-desorption technique

Physical adsorption at the gas/solid interface is a commonly used method for the characterization of surface and structural properties of porous materials allowing the determination of their surface area, pore volume, pore size distribution, and adsorption energy distribution. The gas adsorption technique is performed by the addition of a known volume of gas (adsorbate), typically nitrogen, to a solid material in a sample vessel at cryogenic temperatures (77K for N₂). At cryogenic temperatures, weak molecular attractive forces (van der Waals forces) will cause the gas molecules to adsorb onto (attach to the surface of) a solid material. An adsorbate (gas) is added to the sample in a series of controlled doses, the pressure in the sample vessel is measured after each dosing. There is a direct relationship between the pressure and the volume of gas in the sample vessel. By measuring the reduced pressure due to adsorption, the ideal gas law can then be used to

determine the volume of gas adsorbed by the sample. The resulting relationship of volume of gas adsorbed vs. relative pressure (pressure/saturation vapor pressure of the adsorbent (P/P_0) at constant temperature is known as an adsorption isotherm. From the analysis of the isotherm the surface area and pore size distribution of the sample can be derived. The adsorption isotherm can have different shapes which are based on the adsorbent, adsorbate and the adsorbent adsorbate interaction. According to IUPAC [157] adsorption isotherm is classified into six types. The adsorption types are shown in figure 4.1.

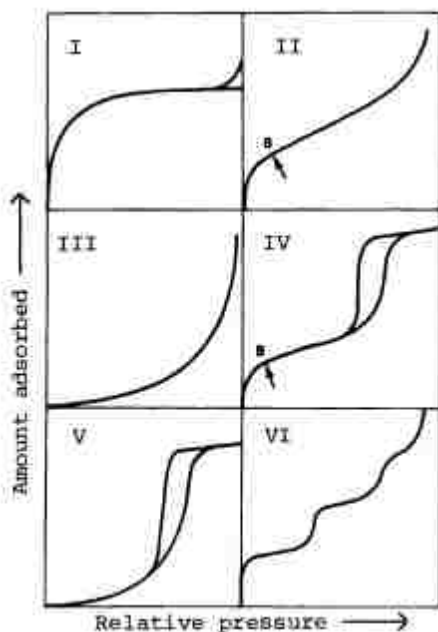


Figure 4.1. The IUPAC classification of isotherms [157].

Type I isotherms are observed with microporous solids with relatively small contributions from the external surfaces of the solid. Hence, the limiting gas uptake is often governed by the accessible micropore volume rather than by the external surface area. Type I isotherm occurs when a monolayer of adsorbate molecules is adsorbed on a non-porous solid. This type is also common for chemisorption.

Type II isotherms are displayed by a nonporous or macroporous adsorbent with high energy of adsorption and have unrestricted monolayer-multilayer adsorption on the surface area of the non-porous adsorbents. The point B shown on the isotherm is often taken to indicate the stage at which monolayer coverage is completed and multilayer adsorption begins dominating during the measurement.

Type III isotherms are affected by the adsorbate-adsorbent interactions and show the formation of a multilayer; they are uncommon and typical for vapor adsorption (i.e. water vapor on hydrophobic materials).

Type IV isotherms reflect monolayer-multilayer adsorption path similar to the type II isotherm, although a type IV isotherm is observed with many mesoporous industrial adsorbents. At saturation vapor pressure the isotherm levels off to a constant value of adsorption. The portion of isotherm which is parallel to the pressure axis is attributed to pore filling by capillary condensation. Capillary condensation occurs due to multilayer adsorption when pore spaces in a porous medium are originally filled with vapor. The gas molecules condense into a liquid phase in the pores. After condensation in the pores, a meniscus is formed at the vapor-liquid interface and at pressures below the saturated vapor pressure, there is equilibrium. In mesopores it is generally associated with a shift in the vapor-liquid coexistence curve [158]. According to Roque-Malherbe [158], condensation occurs at a pressure P , less than the saturation pressure P_0 , of the fluid and this relative pressure (P/P_0) value depends on many factors. Some of these factors include: vapor-liquid interfacial tension, the strength of the molecular interactions among the fluid and the mesopore walls, the mesopore geometry, and the mesopore size. Capillary condensation is typically characterized by a step change in the adsorption isotherm [158]. Materials which

have a uniform pore size distribution usually have a notably sharp step in their adsorption isotherm in which capillary condensation occurred.

Type V isotherm is also not very common, and it is related to the type III isotherm in that the adsorbent-adsorbate interaction is not strong, but can be observed with certain porous adsorbents.

Type VI isotherm represents stepwise multilayer adsorption on a uniform non-porous surface.

In surface adsorption, hysteresis is used to describe the phenomenon of the desorption isotherm being different from the adsorption isotherm, *viz.* the amount of adsorbate is greater for desorption [157]. Conventionally, four types of hysteresis loops are identified (Figure 4.2).

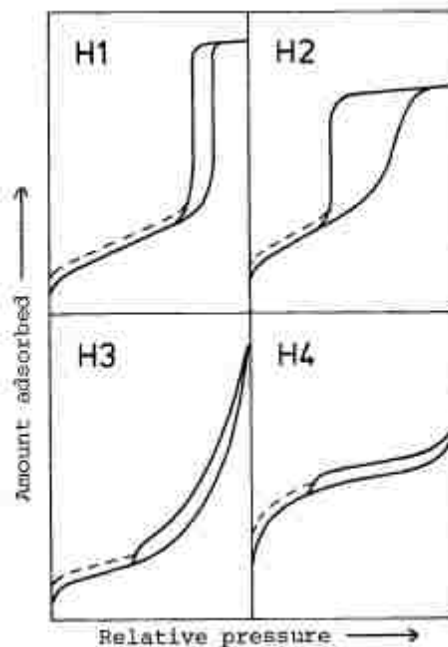


Figure 4.2. Types of hysteresis loops [157].

Hysteresis loops reveal more details of pore structures of the materials: An H1 type hysteresis loop suggests that the material has regular even pores without interconnecting channels; the H2 type of loop indicates that the pores with narrow and wide sections and the materials have possible interconnecting channels; the H3 type is for a type II isotherm with slit-like pores; and H4 is for slit-like pore for type I adsorbent - adsorbate pairs [157]. In the literature, there are many models which describe the adsorption phenomenon using mathematical relationships. The Langmuir monolayer adsorption is the simplest isotherm model. It has been derived theoretically from both kinetic and statistical mechanical concepts [159]. In this model, it is assumed that the adsorbate molecules are adsorbed on a fixed number of well-defined, localized sites, each of which can hold only one adsorbate molecule. All sites are energetically equivalent and there is no interaction among the adsorbate molecules adsorbed on neighboring sites.

Stephen Brunauer, Paul Emmett, and Edward Teller [160] extended the Langmuir model in 1938 by introducing a multilayer adsorption model. The first letter of each publisher's surname was taken to name this theory. The BET model assumes that, in addition to the assumptions made for the Langmuir model, each adsorbate molecule in the first layer serves as an adsorption site for an adsorbate molecule into the second layer, the second layer to the third layer, and so on. The attractive forces between the adsorbate molecules are negligible. The heat of adsorption of the second and subsequent layers is assumed to be equal to the heat of liquefaction of the adsorbate and different from the heat of the adsorption of the first layer. The BET equation used can be given as [160]:

$$\frac{1}{W\left(\left(\frac{P_0}{P}\right)-1\right)} = \frac{1}{W_m C} + \frac{C-1}{W_m C} \left(\frac{P}{P_0}\right) \quad \text{Equation 4-1}$$

in which W is the weight of the gas adsorbed at a relative pressure P/P_0 and W_m is the weight of the adsorbate required for the monolayer surface coverage; C is the BET constant and is related to the energy of adsorption in the first adsorbed layer and it indicates the magnitude of the adsorbent/adsorbate interactions, it varies from solid to solid ($C = \exp\left(\frac{E_1 - E_L}{RT}\right)$ in which E_1 is the heat of adsorption for the first layer, and E_L is heat of adsorption for the second/ higher layers (also known as heat of liquefaction)).

BET theory is based on the following hypotheses [161, 162]:

1. Gas molecules physically adsorb on a solid in layers infinitely – an isolated adsorbed molecule can adsorb a second molecule on top, yielding a full energy of liquefaction, and that in turn a second molecule can adsorb a third and so on;
2. Adsorption takes places either on surface sites or on the top of molecules already adsorbed but not in-between positions;
3. The first layer only interact with the surface, all other layers have interparticle interactions with the same energy as would apply in the liquid state, and involving only nearest neighbors in the vertical stack of adsorbed atoms in each site;
4. For each layer it is possible to apply Langmuir theory since the BET theory is essentially an extension of Langmuir model to multilayer adsorption.

Surface area measurements are usually done using inert adsorbates such as N_2 , or Ar and expressed in units of area per mass of a sample (m^2/g). Based on the amount of the adsorbate required to form a monolayer surface coverage at a given pressure, one can calculate the total surface area of the material. The cross sectional area (A_{cs}) value for the hexagonal close-packed nitrogen monolayer at 77 K is 16.2 \AA^2 [160]. Thus, the total surface area of the sample can be expressed as [160]:

$$S_t = \frac{W_m N A_{cs}}{M} \quad \text{Equation 4-2}$$

in which N is the Avogadro's number (6.022×10^{23} molecules mol⁻¹) and M is the molecular weight of the adsorbate. The specific surface area can be determined by dividing S_t by the sample weight. Nitrogen is used most often to measure BET surface area, but if the surface area is very low, argon or krypton may be used as both give a more sensitive measurement, because of their lower saturation vapor pressures at liquid nitrogen temperature. The amount of gas adsorbed depends not only on the exposed surface area but also on the temperature, gas pressure and strength of interaction between the gas and solid. In BET surface area analysis, nitrogen is usually used because of its availability in high purity. The surface is cooled using liquid N₂ to 77K to obtain detectable amounts of adsorption. Relative pressures less than atmospheric pressure is achieved by creating conditions of partial vacuum. Known amounts of nitrogen gas are then released stepwise into the sample cell. Highly precise and accurate pressure transducers monitor the pressure changes due to the adsorption process. The data collected are displayed in the form of an isotherm, which plots the amount of gas adsorbed as a function of the relative pressure. In addition to the surface area measurements, the pore volume and pore size distributions are also calculated. For pore volume measurements, the total pore volume can be calculated from the amount of vapor which is adsorbed at a relative pressure close to unity (with an assumption that all the pores are filled by the adsorbate). The volume of nitrogen adsorbed (V_{ads}) can be converted to the volume of liquid nitrogen (V_{liq}) contained in the pores using the following equation [160]:

$$V_{liq} = \frac{P_a V_{ads} V_m}{RT} \quad \text{Equation 4-3}$$

in which P_a and T are ambient pressure and temperature respectively and V_m is the molar volume of the liquid adsorbate ($34.7 \text{ cm}^3 \text{ mol}^{-1}$ for nitrogen).

The distribution of pore volumes with respect to the pore size is known as pore size distribution. The most common method for obtaining the pore size distribution is the Barrett-Joyner-Halenda (BJH) method [163]. The basic assumptions which the BJH takes into consideration are; (a) cylindrical pore shape, (b) condensation takes place at lower pressure in smaller pores and larger pores are filled as the relative pressure increases.

Mesopore size calculations assuming the cylindrical geometry can be obtained by using the Kelvin equation [160]:

$$r_k = \frac{-2\gamma V_m}{RT \ln \frac{P}{P_0}} \quad \text{Equation 4-4}$$

in which γ is the surface tension of nitrogen at its boiling point ($8.85 \text{ ergs cm}^{-2}$ at 77 K), V_m is the molar volume of nitrogen, r_k is the Kelvin radius of the pore.

Desorption is a process opposite to the adsorption and occurs in a system being in the state of sorption equilibrium between the bulk phase (fluid phase) and the adsorbing solid surface. When the concentration (or pressure) of the adsorbate in the bulk phase is lowered, some of the adsorbate is released from the surface of the adsorbent to the bulk phase. Temperature change can also cause desorption. As the temperature rises, desorption occurs, because the increase in temperature provides the energy required to overcome forces between the adsorbent and the adsorbate.

Before the specific surface area of the sample can be determined, it is necessary to remove gases and vapors that may have become physically adsorbed onto the surface after

manufacture and during treatment, handling and storage. If outgassing is not achieved, the specific surface area may be reduced or may be variable because an intermediate area of the surface is covered with molecules of the previously adsorbed gases or vapors. Samples are degassed in a vacuum at high temperatures. The highest temperature possible that will not damage the sample's structure is usually chosen in order to shorten the degassing time.

4.1.2. Scanning Electron Microscopy (SEM)

Electron microscopes were developed in the 1930s to overcome the limitations of optical microscopy and provide increased magnification and resolution, far superior to optical systems. The first commercialized Scanning Electron Microscope (SEM) was built by Cambridge Instruments [164].

Scanning Electron Microscopy is a very powerful imaging tool commonly used to visualize nano- and microstructures [165-167]. The difference between optical microscopy and SEM is the way how an image is “produced”. In the first case the sample is probed with photons while in SEM a focused electron beam is transmitted from an electron gun (Figure 4.3). The principle of SEM is based on the interaction of an incident electron beam and the solid specimen [168]. The resolution of SEM images is so greatly improved when compared with optical ones due to *ca.* 10^5 times shorter wavelength of electrons than photons. The signal contains information about surface topography, external morphology, chemical composition, crystallographic information, and electrical conductivity [168]. The instrument allows for the observation of materials on a very small scale ranging from nanometers to micrometers. An ability to produce three-dimensional (3D) images is one of the most outstanding capabilities of the SEM apart from the high resolution, higher

magnification and ease of sample observation. A large depth of field of the SEM allows for the focusing of larger areas of the specimen at one time resulting in 3D images.

Electrons generated in the electron gun are accelerated in an electric field. Then the beam is focused by condenser lenses, passes through deflection coils and when it is properly oriented it finally scans the sample [165]. Scanning Electron Microscopy uses electrons emitted from tungsten or Lanthanum hexaboride (LaB_6) thermionic emitters for the visualization of surface of the sample. The filament is heated resistively by a current to achieve a temperature between 2000-2700 K what results in an emission of thermionic electrons from the tip over an area of $100 \mu\text{m} \times 150 \mu\text{m}$. The electron gun generates electrons and accelerates them to energies in the range 0.1 – 30 keV towards the sample [169]. A series of lenses focus the electron beam on to the sample where it interacts with the sample to a depth of approximately $1 \mu\text{m}$. There are many possible ways for loss of energy by electrons interacting with the sample. It can be emitted as low-energy secondary electrons (SE), high-energy backscattered electrons (BSE), characteristic X-rays, transmitted electrons or heat. X-rays have a characteristic energy unique to the element from which they originate and so provide compositional information about a sample. Usually a detector that collects SE electrons is utilized. Obtained SEM images are characterized with a very high quality and resolution [167]. However, in some cases, it is more intentional to use a detector that collects BSE which allows to record images with high compositional contrast of different components present in the sample [167]. Both SE and BSE signals are collected when a positive voltage is applied to the collector screen in front of the detector. When a negative voltage is applied on the collector screen only BSE signal is captured because the low energy SEs are repelled.

An SEM consists of three distinct parts: an electron column; a detection system; and a viewing system. Figure 4.3 shows a schematic of a simple scanning electron microscope. Two electron beams are controlled simultaneously by the same scan generator: one is the incident electron beam; the other is for the cathode ray tube (CRT) screen. The incident beam is scanned across the sample, line by line, and the signal from the resulting SE is collected, detected, amplified and used to control the intensity of the second electron beam. Thus a map of intensity of secondary electron emission from the scanned area of the sample is shown on the CRT screen as variations in brightness, reflecting the surface morphologies of the specimen. Given this mechanism, the magnification of the SEM image can be adjusted simply by changing the dimensions of the area scanned on the sample surface [164].

One of the crucial issues to be considered is the preparation of a sample. Conductive substrates do not need a special treatment; they only have to be electrically grounded. This is also applicable for substrates in which only a top layer is conductive (*e.g.* ITO electrode). However, when the sample is insulating, an ultrathin conductive film has to be deposited, usually by sputtering to make the surface conductive, increase signal and surface resolution, and prevent accumulation of static electric charge on the specimen. Metallic (*e.g.* gold or platinum) thin films are commonly used. Nonetheless, there is an exception from these methodologies when non-conductive samples are analyzed in low-voltage mode of SEM or environmental SEM. Last but not least, the sample has to fit the holder that is placed in the chamber [169].

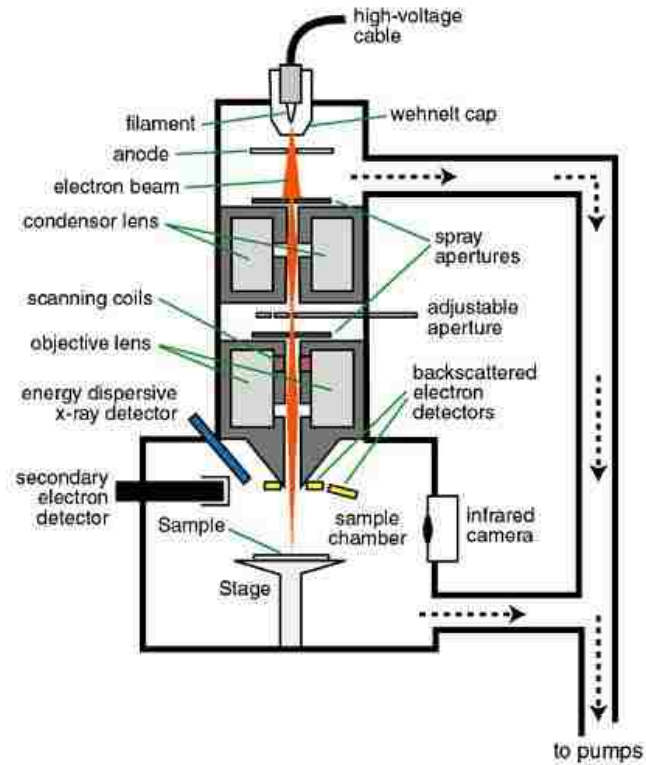


Figure 4.3. Schematic illustration of SEM setup [170].

4.1.3. Transmission electron microscopy (TEM)

In a transmission electron microscope (TEM), similarly to the SEM, electrons are used to screen the sample and produce an image [171-173]. However, there are several significant differences between them. First, in TEM, the electron beam is partially transmitted through the sample and then it is collected on the fluorescent screen (Figure 4.4). Another issue is how strongly the beam is accelerated by an anode. For TEM it is usually 100 keV (40 – 400 keV), while for SEM it ranges between 0.2 and 40 keV [171]. Specimen preparation is also different. Since the beam has to penetrate the sample, the specimen has to be thin enough, on the order of hundreds of nanometers. Otherwise the electron beam might be completely scattered.

The first practical TEM was built by Albert Prebus and James Hillier at the University of Toronto in 1938 using concepts developed earlier by Max Knoll and Ernest Ruska [174]. Since then, the TEM has had considerable development and is now a versatile tool of characterization in material science and biology.

A general TEM usually consists of six basic components, as follows [174, 175]:

- 1) Source providing illumination: An electron source, commonly used in all TEMs, comprises a filament, which emits electrons either by thermal heating (a so-called thermionic filament) or through application of a high electric field to a metal filament tip generating field emission electrons (so-called field-emission filament). The field-emission filament is a lot more expensive and requires much higher vacuum than the thermionic filament, but offers a very stable source with a greater resolution and longer life-time.
- 2) Electrodes: These include a cathode, which accelerates the electrons generated from the filament to a high energy, ranging from a few hundreds to over a million electronvolts. Although a higher voltage can produce a higher resolution, in fact, most TEM instruments are operated at energies between 100 kV and 400 kV. This is to reduce sample damage and the cost of the instrument while still achieving a very short electron wavelength.
- 3) An electron optics system: This consists of a series of electromagnetic lenses, such as condenser lens, objective lens, projective lens as well as intermediate lens. These lenses help to focus the electrons to produce a small probe beam and form images of samples. The objective lens is the heart of the microscope. The spherical and

chromatic aberrations inherent in the objective lens are the major limitations to the resolution of the TEM instrument.

- 4) A sample chamber: This is where the sample is positioned, and is directly above the objective lens. It is important that the chamber is spacious enough to allow the samples to be viewed with a wide range of tilting necessary for the crystal orientation examination as well as for chemical analysis.
- 5) Camera(s): Images of the samples can be acquired using a video/scanned camera which is located beneath a phosphor screen where the images are seen. The photographs are taken by lifting up the screen and exposing the film in the camera. However, this recording method has been gradually replaced by using a charge-coupled device (CCD) camera, which collects a digital image which can be saved onto a computer.
- 6) Vacuum system: in order to minimize scattering of the electrons by air molecules and to increase the mean free path of the electron the TEM runs at a very high vacuum (typically 10^{-4} Pa), which is maintained by a vacuum system. In most cases, such a system comprises a combination of two types of pumps, i.e. mechanical and diffusion pumps.

An electron gun is responsible for producing the electrons that are irradiated onto the specimen. Electrons are usually generated in an electron microscope by thermionic emission from a filament, usually tungsten, in the same manner as a light bulb, or by field emission. The electrons are then accelerated by an electric potential (measured in volts) and focused by electrostatic and electromagnetic lenses onto the sample. Two condenser lenses are responsible for focusing the beam into a pinpoint beam. The

transmitted beam contains information about electron density, phase and periodicity. All of the information is to be used to form an image [176]. A condenser aperture then restricts the beam by knocking out high angle electrons. As the beam comes into contact with the specimen, part of it is transmitted and focused by the objective lens forming an image. The image is then passed through the intermediate and projector lenses which enlarge it before it hits the phosphor screen where it can be seen. The TEM image contrast is due to elastic scattering of electrons. There are various contrast modes to improve the image quality. These modes include: bright and dark field; diffraction contrast; and phase contrast [177]. Bright and dark field modes are based on the occlusion and absorption of electrons in the sample. For amorphous materials, darker areas on the image correspond to fewer electrons being transmitted due to the thicker or denser nature of the material at that point. Lighter areas of the image are a result of more electrons being transmitted through the material in areas that are thinner or less dense [174]. The contrast is greater at low accelerating voltage and smaller aperture diameters. To study crystalline structures, the diffraction contrast mode is used. Using selective Bragg scattering, sharp spots can be visualized. In phase contrast mode, scattered electrons are allowed to recombine with unscattered electrons to form the image [174].

To examine materials by TEM requires a sample that normally should be less than 3 mm in diameter with the area of interest sufficiently thin to allow electrons to penetrate it. It is very important to prepare a good TEM sample, which is a prerequisite for any analysis using various TEM techniques (including imaging, EDX and others). Not only is it difficult to thin the bulk sample down to the desired thickness (mostly less than 100 nm), but also

preparation (such as mechanical/electrochemical polishing and ion sputtering) can create a lot of artifacts in and on the sample, which may give rise to false information.

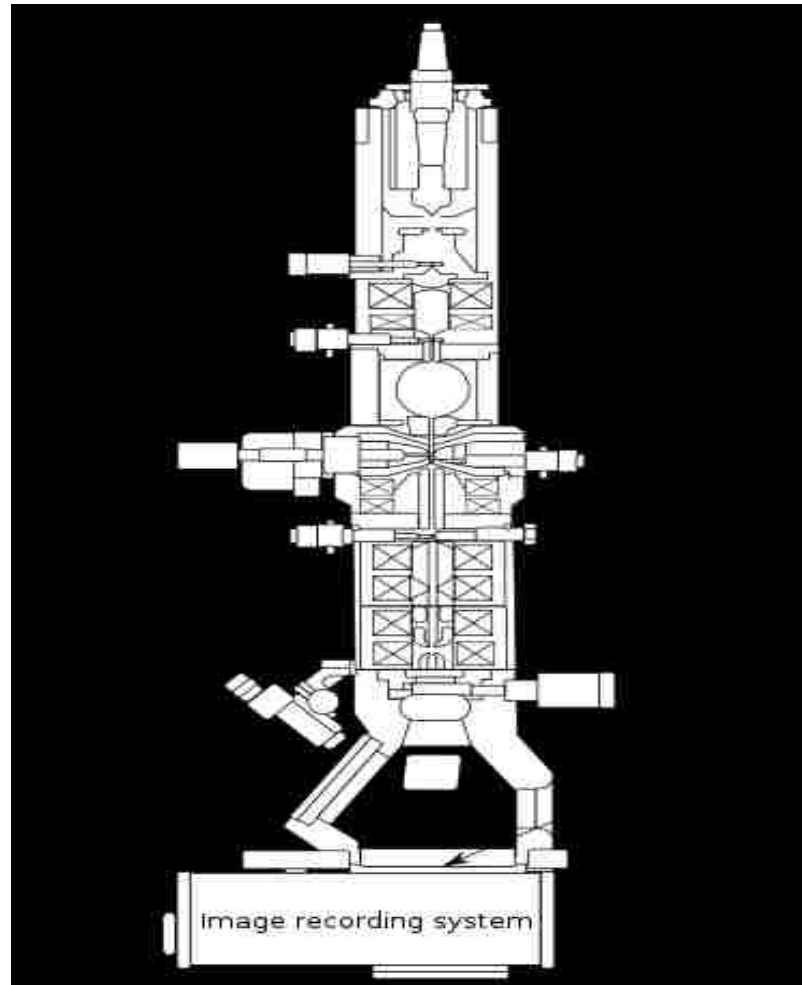


Figure 4.4. Schematic illustration of TEM setup [178].

4.2. Electrochemical characterization

Electrochemistry is the interplay between chemistry and electricity in which reactions involving electrical currents and potential are considered [179]. Since the SSA technology is based on supercapacitors, the electrochemical techniques were utilized in order to ascertain the capacitance, energy and resistances presented in each supercapacitor used for SSA experiments. There are many electrochemical techniques that exist but in this work,

cyclic voltammetry and galvanostatic charge-discharge were used because of their ability to quickly and easily reveal important characteristics of the capacitor and are further discussed in detail. Electrochemical characterization was done with a high-current, high-performance USB potentiostat (GAMRY Reference 3000) in a two electrode cell configuration; all plots were generated using Gamry's Analyst software. A potentiostat is a device that controls the potential between a pair of electrodes whilst measuring the resulting current flow. The Gamry potentiostat can be operated also as a galvanostat. In this case the current flow is controlled while the potential is monitored. The two electrode set up, which uses a working and counter (auxiliary) electrode, was chosen as the simplest cell setup to measure the whole cell. The electrochemical measurements were done directly in the SSA cell in order to measure the capacitive behavior of each pair of electrodes prepared for the SSA experiments.

The standard cell configuration consists of three electrodes immersed in the electrolyte: the working electrode (WE), counter electrode (CE), and reference electrode (RE). This configuration is known as a half-cell setup in which the potential at the WE is monitored and controlled precisely with respect to the RE while the current flowing between the WE and CE is measured [180]. Three-electrode setups have a distinct experimental advantage over two electrode setups: they measure only one half of the cell. That is, the potential changes of the working electrode are measured independent of changes that may occur at the counter electrode. This isolation allows for a specific reaction to be studied with confidence and accuracy. For this reason, 3-electrode mode is the most common setup used in electrochemical experimentation [181] but in this work a two-electrode configuration was used in order to measure the voltage of the whole cell. This setup is typically used with

energy storage or conversion devices such as supercapacitors, batteries, fuel cells, photovoltaic panels, etc. in which the potential across the complete cell is measured. This includes contributions from the CE/electrolyte interface and the electrolyte itself. The two-electrode configuration can therefore be used whenever precise control of the interfacial potential across the WE electrochemical interface is not critical and the behavior of the whole cell is under investigation.

4.2.1. Cyclic Voltammetry (CV)

Cyclic Voltammetry (CV) is a potentiodynamic experimental method and probably the simplest and most versatile electroanalytical technique used by electrochemists for the study of electroactive species. This technique is performed by cycling a linear potential-sweep between two defined voltages determined by the electrolyte decomposition limits. Often, a CV test will repetitively sweep the voltage between two limiting potentials. A pair of voltage sweeps in opposite directions is called a cycle. The potential applied to the electrode varies linearly with time yielding a time-dependent dynamic responsive current (I) which is recorded by the computer software and given by the following equation [181]:

$$I = \frac{dQ}{dt} = C \frac{dV}{dt} = C S \quad \text{Equation 4-5}$$

in which C is a capacitance in Farads ($F = A \text{ s/V}$) and dV/dt is the scan rate (s) of the linear voltage ramp (V/s).

Several predetermined constant potential-sweep rates are used in the following experiments to evaluate the capacitive charging current passing through the material. In this work the rate was between 0.1 mV/s to 1mV/s. Fast scan rates often show lower

capacitances than slower scan rates. Slow scan rates allow slow processes to occur but take a lot of testing time. In the case where slow surface reactions are present, fast scans are over before reactions occur – all current is due to capacitance. Faradaic current has time to flow when scan rates are slower, increasing total current and capacitance. The increase in capacitance by decreasing scan rate can be explained by kinetically slow Faradaic reactions on the electrode surface and by transmission line behavior caused by electrode porosity. An electrode surface with a high electrolyte resistance will not have time to respond to voltage changes during a fast scan. In effect, the fraction of electrode surface accessible to the electrolyte depends on the scan rate [182].

Ideal double-layer capacitance through CV analysis is depicted by a constant and equivalent charging and discharging current (called the double layer charging current) resulting from a constant sweep rate and is represented by a rectangle within a voltammetry plot of the current with respect to applied potential illustrated in Figure 4.5. The current response of a SC is ideally very fast since the charge storage is electrostatic. Supercapacitors exhibiting double-layer capacitance approach ideality with a constant current measured through a majority of the charging process, deviating slightly from this relation due to diffusion resistances in the initial charging or discharging process of the double-layer for the respective voltage limits. Other materials may not exhibit constant capacitance as a result of material resistances or may display potential specific Faradaic reactions depicted by peaks in the response current due to reversible pseudocapacitive processes typically shown in metal oxides and conducting polymers. Characteristic profiles of these capacitive mechanisms from CV technique are also shown in Figure 4.5. Determining the capacitance C from CV experimental results often requires the integration

of the current response (by integration of a segment of the CV curve the stored charge (Q) can be calculated) in a cyclic voltammogram and can then be calculated by the following equation [182, 183]:

$$C = \frac{\int I \times dV}{\Delta V \times s} = \frac{Q}{\Delta V} \quad \text{Equation 4-6}$$

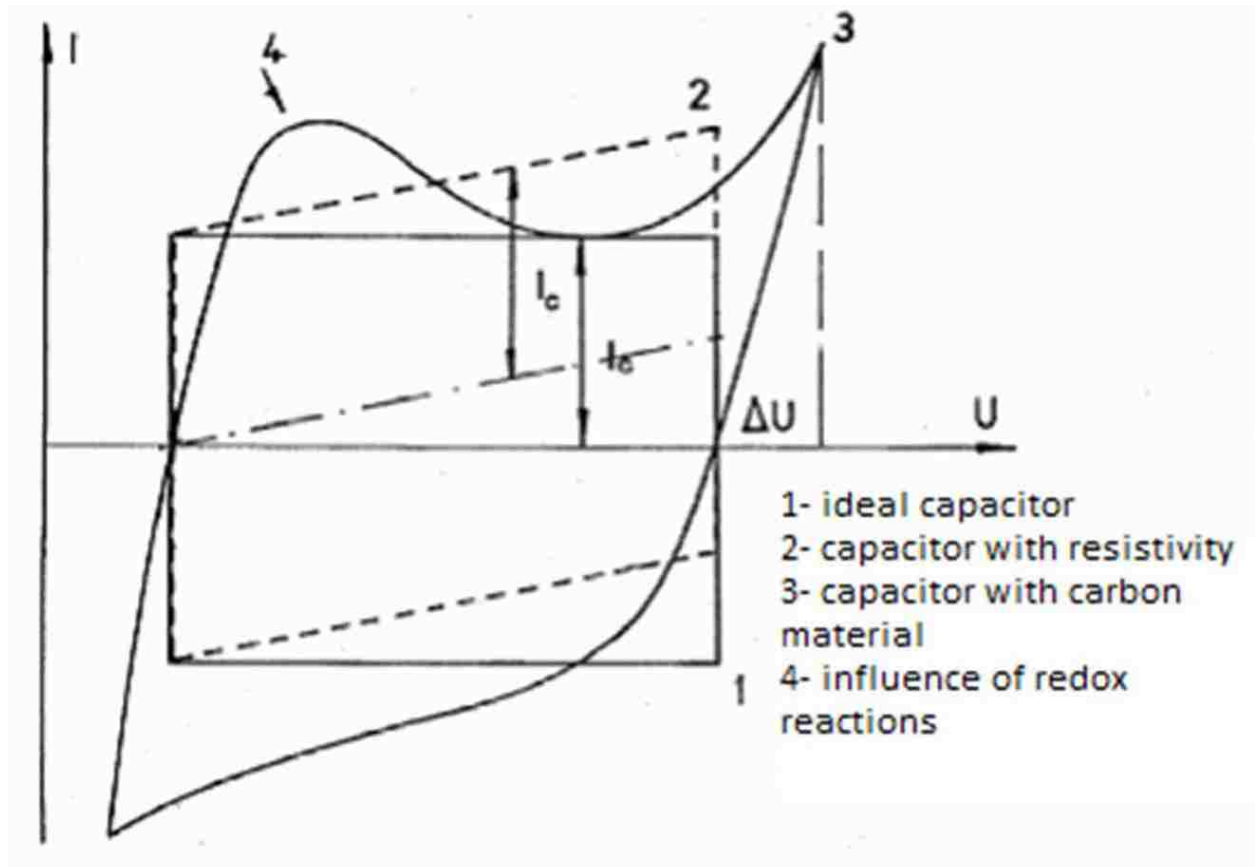


Figure 4.5. Comparison of cyclic voltammograms of various capacitors [184].

Voltammetry can be also graphed as capacitance vs. voltage instead of current vs. voltage.

Charging and discharging at higher power levels correspond to faster sweep rates. Multiple plots which are obtained at different sweep rates are usually displayed on the same graph to demonstrate the influence of power levels on the charging characteristics [185]. In ideal

capacitors capacitance does not depend on the scan rate. However, EDLCs are not ideal and higher scan rate creates lower capacitances.

4.2.2. Galvanostatic Charge-Discharge (GCD)

Galvanostatic Charge-Discharge (GCD) is the standard technique used to test the performance and cycle life of EDLCs. Galvanostatic testing applies a constant current to the electrochemical capacitor using a galvanostat and the resulting voltage change with time is measured resulting in charging of the capacitor up to a pre-set voltage. The capacitor is then discharged and the voltage drop with time is measured. A repetitive loop of charging and discharging is called a cycle. Different currents can be chosen resulting in different current densities that can be used to calculate specific capacitance. The charge (capacity) of each cycle is measured and the capacitance C , in farads (F), is calculated (Equation 4-7). Both are plotted as a function of cycle number. This curve is called the capacity curve [185].

$$C = \frac{Q}{V} \rightarrow \frac{dV}{dt} = \frac{I}{C} \quad \text{Equation 4-7}$$

in which V is the cell potential in volts (V), I is the cell constant current in amperes (A), and Q is the charge in coulombs (C) or ampere seconds (As).

A typical constant current charge and discharge chart of an ideal supercapacitor is characterized by linear charging and discharging curves (a mirror image of the charging and discharging curves) as shown in Figure 4.6. However, a non-ideal supercapacitor or the one which is characterized by pseudocapacitance has non-linear charge and discharge curves.

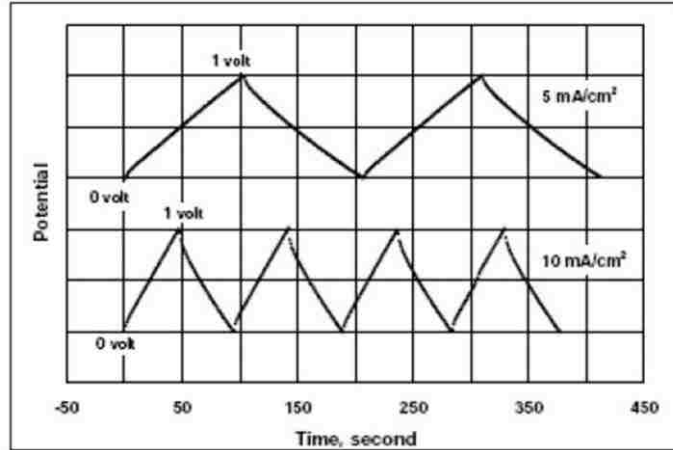


Figure 4.6. Typical charge and discharge curves for a supercapacitor [186].

This technique allows for a determination of the equivalent internal series resistance by quantifying the drop upon discharge ($ESR = \frac{\Delta V_{IR}}{I} \left[\frac{V}{A} = \Omega \right]$). The ESR has several contributions to it including the electrical resistance of the carbon electrodes, the interfacial resistance between the current collectors (contacts) and active electrode mass, and ionic resistance of the electrolyte [185, 187]. The GCD test provides information on the (specific) capacitance of the device (F/g), energy density (Wh/kg), power density (W/kg), ESR (Ohm) and the effect of current density on these characteristics. Theoretically, a perfect ideal capacitor would be lossless and have an ESR of zero, but unfortunately capacitors always have some ESR. A higher ESR leads to a large V_{IR} at each half cycle which dramatically reduces power and capacity [185].

Different constant currents can be applied but as the charge-discharge happens at constant current values the power increases, but the capacitance and energy density are reduced due to the inability of the ions to respond quickly enough to form the double layer and/or allow for the necessary faradaic reactions to take place.

From the GCD experiments also energy (E) used for charge and recovered by discharge can be calculated by integration of the area under the GCD charge and discharge curves multiplied by the constant current accordingly with equation 4-8 [185].

$$E_{charge} = V \times I \times t \quad [V \times A \times s = J] \quad \text{Equation 4-8a}$$

$$E_{discharge} = V \times I \times t \quad [V \times A \times s = J] \quad \text{Equation 4-8b}$$

in which V is potential difference (voltage), I is a constant current value and t is time in seconds necessary to complete charge or discharge step.

5. Introduction to Supercapacitive Swing Adsorption (SSA)

5.1. The origins of SSA

The original idea of adsorption and desorption of carbon dioxide was high electric field and high voltage application to two electrolyte-free inexpensive high surface area carbon (HSAC) materials. These HSAC materials are electrically conductive sorbents with large capacity for CO₂ capture. The technique, called electric field swing adsorption (EFSA), would use applied high electric potentials (up to 5kV) to control the surface interaction between CO₂ gas molecules and an electrically conducting carbon sorbent material. The structure of CO₂ suggests that it is an electron-poor π -system, which would have an affinity for an electron rich π -system. It was expected that the high electric potential would change the electronic structure of the carbon sorbent material which would increase or decrease CO₂ adsorption properties of this carbon depending on the used bias. Negative charges would increase the Lewis basicity of the sorbent surface. Moreover, the adsorptive forces could have partial chemisorptive character because the interactions can be understood as dative bonds between the Lewis basic π -electron system of the carbon and the Lewis acidic center of CO₂. According to this model, a negative bias should favor adsorption, while positive bias should favor desorption. Selectivity of CO₂ over N₂, a major component of flue gas, should be high due to lack of an electron accepting center in nitrogen.

In an attempt to test the effectiveness of an electric field on the carbon dioxide adsorption capacity, a custom cell was designed according to Figure 5.1, in which two carbon electrodes formed a parallel plate capacitor. The cell was leak-tight down to $< 1 \times 10^{-6}$ Torr. It was made from inert materials (stainless steel, alumina) to minimize residual absorption

on cell surfaces. A mount for the adsorbent was electrically isolated and capable of sustaining electric potentials of ± 5 kV relative to ground without breakdown.

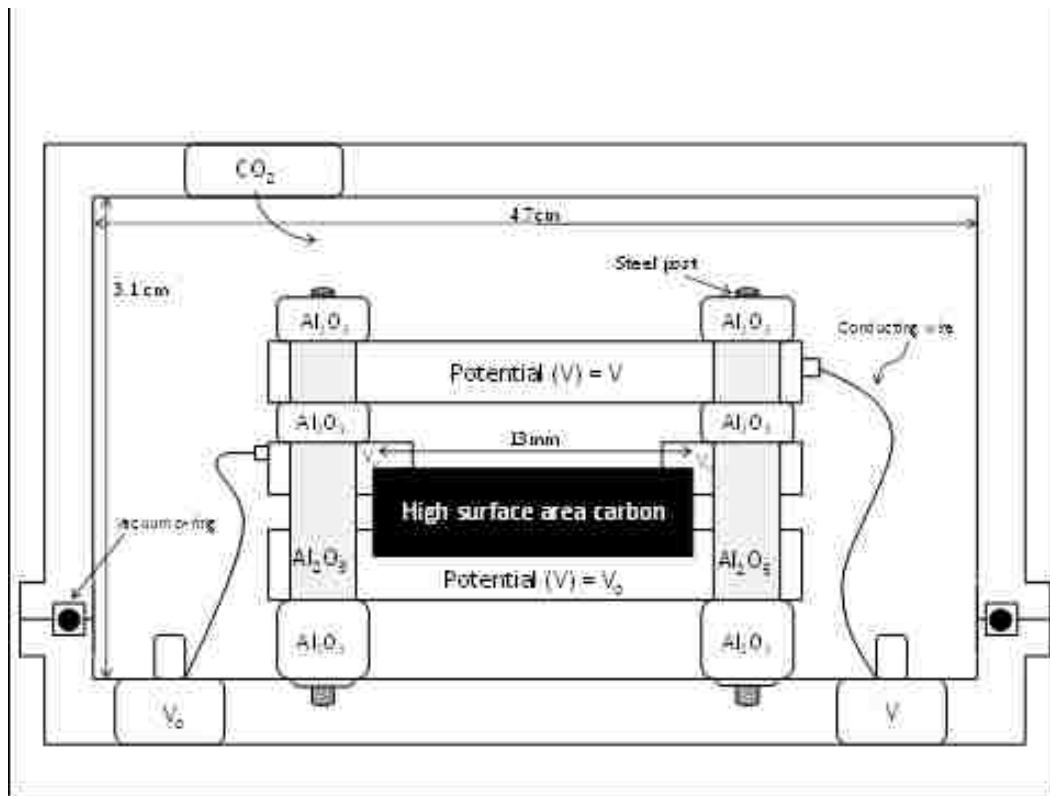


Figure 5.1. Preliminary design for EFSA adsorption cell (image designed by Dr. David T. Moore and Nina K. Jarrah).

Unfortunately this idea did not work and no adsorption or desorption was observed while applying high voltages up to 5kV probably because it was not possible to change the surface charge-density of the sorbent to a sufficient extent to produce a significant change of the CO₂ adsorption properties. The experimental setup was analogous to a parallel plate capacitor setup in which voltage is supplied from two electrode plates with a dielectric medium in between. In the parallel plate capacitor model, the charge in the capacitor is distributed mostly on the outer surface of the electrode, rather than the inside and suggests that in the proposed set up only the outer surface area of the carbon electrodes was

effectively charged, which was a tiny fraction of the total high surface area. The calculation of the number of charges distributed over the outer surface area of the carbon electrode (the electrodes were in the form of pellets with diameter of 13 mm what gives an outer surface area of 530.93 mm² ($4 \times \pi \times r^2$) in which r is a radius of the pellet) can show if it is possible that these charges can affect the CO₂ sorption behavior of the carbon electrodes since the CO₂ sorption capacity of a typical carbon sorbent is on the order of 2 mmol/g at 298 K and 1 atm. By using equation 5-1 the capacitance C of flat, parallel plates of area A and separation d can be calculated:

$$C = \frac{k \times \epsilon_0 \times A}{d} \quad \text{Equation 5-1}$$

in which k is the dielectric constant of a material between two electrodes (1.6 for carbon dioxide) and ϵ_0 a permittivity of empty space (8.85×10^{-12} F/m).

$$C = \frac{1.6 \times (8.85 \times 10^{-12}) \times (5.31 \times 10^{-4})}{0.001} = 7.52 \times 10^{-12} F \left[\frac{F}{m} \times m^2 = F \right]$$

Further, by using equation 5-2 the amount of charge that can be placed on a capacitor can be calculated:

$$Q = C \times V \quad \text{Equation 5-2}$$

in which Q is number of charges in Coulombs (C), C is capacitance in Farads (F), and V is potential difference (voltage) between two electrodes in volts (V).

$$Q = 7.52 \times 10^{-12} F \times 1 V = 7.52 \times 10^{-12} C \left[F \times V = \frac{C}{V} \times V = C \right]$$

Since in 1 Coulomb there are 6.24151×10^{18} electrons, in 7.52×10^{-12} Coulombs there are 4.69×10^7 electrons. 1 mol is 6.02×10^{23} electrons so 4.69×10^7 electrons are in 7.79×10^{-14} mmol. Thus, the ratio between the number of electrons in the capacitor material and the number of carbon dioxide molecules that can be adsorbed is 7.79×10^{-14} mmol electrons/g \div 2 mmol CO₂/g. From this calculation it can be concluded that it is highly unlikely that the charges can change the surface charge-density of the carbon electrode to a sufficient extent to affect the sorption behavior of a significant number of CO₂ molecules.

To circumvent these problems and to effectively load charges into the inner surface of the HSA carbon, the concept of the electric double layer capacitor (EDLC) was used. An EDLC (also called a supercapacitor) has much higher capacitances (on the order of several hundred Farads per gram electrode material) in comparison to a classical parallel plate capacitor. The derived gas adsorption technique was named as supercapacitive swing adsorption (SSA).

5.2. The main hypotheses of SSA

As it was described in Chapter 3 of this thesis an EDLC (also called supercapacitor) contains two nanoporous carbon electrodes with a separator soaked in electrolyte. When an EDLC is charged, an electrical double layer of charges forms at the interface between the electrode pore surface and an electrolyte, increasing the amount of charge that can be delivered to the sorbent surface. This much higher capacitance is due to the high surface area of the carbon material which has direct contact between the charge on its pore surfaces and the counter ion from an electrolyte. It was expected that the presence of this electric double layer can change the interaction of the CO₂ with the electrode, because a much

larger number of electrons were stored in the capacitor compared to the previous parallel plate capacitor. Moreover, it was possible to estimate the number of these surface charges and hence the number of counter ions covering that surface by assuming a typical surface area for the capacitor material (e.g. $1000 \text{ m}^2 \text{ g}^{-1}$), a typical operating voltage (1V), and a typical capacitance (100 F g^{-1}). The calculation of the number of counter ions distributed over a surface area of $1000 \text{ m}^2 \text{ g}^{-1}$ would show if it may be possible that these ions can affect the CO_2 sorption behavior of the carbon electrodes since the CO_2 sorption capacity of a typical carbon sorbent is on the order of 2 mmol/g at 298 K and 1 atm . By using equation 5-2 the amount of charge that can be placed on a capacitor can be calculated:

$$Q = 100 F \times 1 V = 100 C \left[F \times V = \frac{C}{V} \times V = C \right]$$

Since in 1 Coulomb there are 6.24151×10^{18} electrons, in 100 Coulombs there are 6.24151×10^{20} electrons. 1 mol is 6.02×10^{23} electrons so 6.24151×10^{20} electrons are in 1.03 mmol. These electrons are balanced by the counter-cations M^+ , therefore there are 1.03 mmol M^+ on the pore surface per gram of the capacitor material. Thus, the ratio between the number of electrons in the capacitor material and the number of carbon dioxide molecules that can be adsorbed is $1.03 \text{ mmol M}^+/\text{g} \div 2 \text{ mmol CO}_2/\text{g}$. From this calculation it can be concluded that the ions may affect the sorption behavior of a significant number of CO_2 molecules because their numbers are in the same order of magnitude.

The two desirable properties of both EDLC's (very high capacitance) and microporous activated carbon (high adsorption affinity for CO_2), are used in the implementation of SSA for carbon dioxide capture.

Aqueous electrolyte was chosen because of its low cost and its excellent solubilizing properties for ions. Carbon materials are quite hydrophobic and only hydrophilic carbon pores should be infiltrated by the aqueous electrolyte, leaving the hydrophobic ones open for gas adsorption. Moreover capillary forces are only attractive when adhesion (water is attracted to other substances) is stronger than cohesion (water is attracted to water) and these forces are weaker the larger the pore size. It was assumed that the aqueous electrolyte would infiltrate the mesopores and interparticulate spaces of pressed carbon pellets, however the micropore surfaces, as the smallest in size, would be sufficiently hydrophobic thus the aqueous solution would be kept out by capillary forces, leaving the micropores free for CO₂ adsorption. This means that the electrolyte and the sorbent must interpenetrate in a way that leaves contiguous pathways available for transport of gas molecules (through the open sorbent pores), electrons (through the sorbent pore walls), and ions (through pores filled with the electrolyte). Furthermore, it was hypothesized that an optimum combination of gas sorption and ion conductivity can be achieved by a three-phase system in which carbon electrodes would be partially immersed into aqueous electrolyte solution, leaving the upper part of the electrode accessible to the adsorbate gas while the lower part can be infiltrated by the electrolyte.

When charging the EDLC, small ions (e.g. Cl⁻, Na⁺) would be mobilized out of the bulk electrolyte and drawn into micropores, that would change the electronic structure of the carbon pore surface of the micropores. It is assumed that this would bring a significant change on the CO₂ adsorption properties which was adsorbed on the micropore walls leading either to an enhanced or decreased adsorption of the CO₂ (Figure 5.2). Size and/or direction of the effect would depend on electrode character (anode vs. cathode) since the

structures of both double layers are different. Moreover, when the EDLC would be discharged, the driving force would be in the opposite direction, and the ions would return to the electrolyte, restoring the original electronic state of the pore walls and thus the original adsorptivity of the sorbent material.

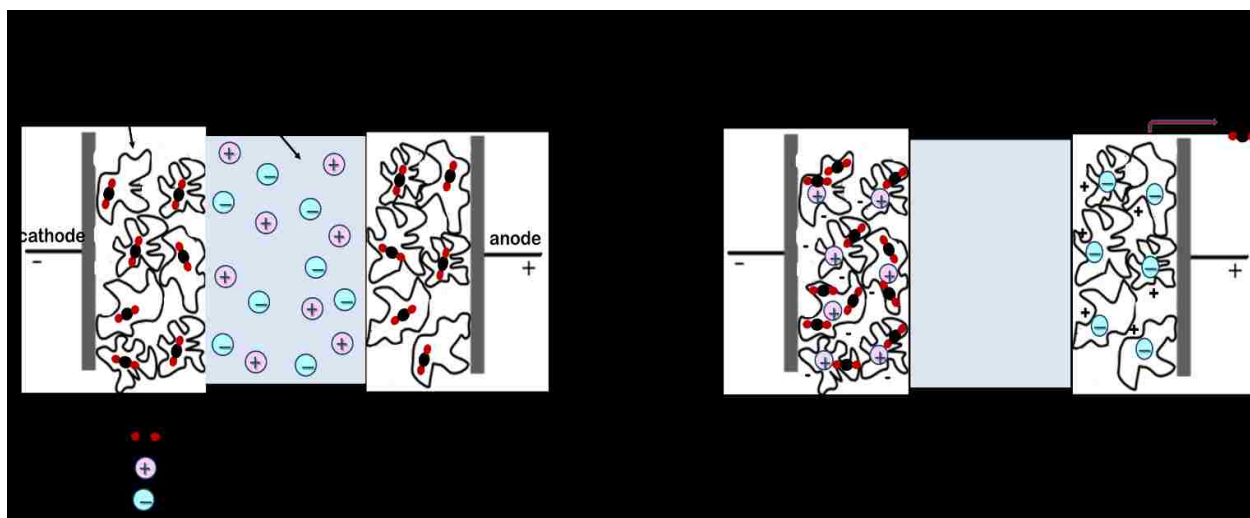


Figure 5.2. Scheme of the hypothesized SSA mechanism.

In SSA electrodes with high surface area (HSA), high electrical conductivity and high affinity for CO₂ are needed. High surface area activated carbons are the predominant electrode material not only for SC applications but also as solid sorbents for carbon dioxide adsorption. For SSA application the commercially available activated HSAC (BPL carbon from Calgon Company) was used as the electrode material. The BPL carbon is a low cost mesoporous-microporous carbon activated from bituminous coal, and usually used as a reference material for CO₂ adsorption. It has a surface area of 640 m² g⁻¹ (calculated from the BET method) and a CO₂ equilibrium loading of 1.2 mol/kg at 298 K and 1 atm. The electrodes were prepared as pellets or as monoliths and detailed procedure of their preparation is given in Chapter 6 (section 6.3). An important factor for SSA is that the AC


materials have inherent corrosion resistance and can be used millions of cycles with little performance degradation. This property is well documented for applications is supercapacitors. [188].

5.3. Advantages of SSA

There are several advantages which could potentially make SSA a good candidate for carbon dioxide capture in coal-fired power plants:

- Since the SSA method depends on repeated capacitive charge and discharge of SC, energy invested for adsorption would principally be recovered upon desorption.
- SC requires only the physical re-arrangement of electronic and ionic charge with no chemical changes and can typically be cycled over a million times with little performance degradation, thus, the process of adsorption and desorption could be constantly repeated.
- In an SSA cycle no temperature and pressure changes are required because adsorption and desorption would be only controlled by capacitive charge and discharge.
- The operating temperature of SSA would only be limited by boiling point of the used electrolyte. If aqueous electrolytes are chosen the maximum operating temperature would be 99 °C (at 1 atm). The temperature of flue gas leaving a desulfurization unit is around 70 °C, consequently SSA with aqueous electrolytes could be compatible with flue gas temperature conditions.
- The parasitic load associated with SSA would likely decrease with increasing operating temperature since the charge-discharge energy efficiency of

supercapacitors increases with increasing temperature because of increasing ionic conductivity with increase in temperature.

 SSA would use only inexpensive and environmentally friendly materials (NaCl and activated carbon).

6. Materials, reagents and experimental setup

6.1. Materials and chemicals

- Activated Carbon (Coal Based) – BPL Carbon 4x10 was obtained from Calgon Carbon Corporation. It was obtained in a granular form which was then powdered with a mortar and pestle;
- Polyvinylidene fluoride (PVDF), $-(C_2H_2F_2)_n-$, with average $M_w \sim 534,000$ by GPC, in the form of powder was purchased from Sigma Aldrich;
- N-Methyl-2-pyrrolidone (NMP), C_5H_9NO , with 99.5+% grade was purchased from Alfa Aesar;
- Carbon fabric, 20cm x 20cm, AvCarb © was purchased from Fuel Cell Earth;
- Conductive Carbon Paint was purchased from SPI Supplies®;
- Sodium Chloride (NaCl) with 99.0% grade was purchased from EMD Chemicals
- 15% CO_2 /85% N_2 gas mixture - NI-CD15K (15.6% of CO_2 certification, $\pm 2\%$ accuracy) was purchased from Airgas, pure CO_2 (ultra-pure) was purchased from Airgas, pure N_2 - NI4.8T 5.0 (ultra high purity) was purchased from Praxair, pure He - HE4.7LS-T (ultra high purity) was purchased from Praxair

6.2. Experimental setup for the SSA experiments

To explore the effect of SSA on carbon dioxide/sorbent interactions in aqueous electrolyte systems, the pressure response of the gas phase above the sorbent was monitored while charging/discharging a supercapacitor. In this method two electrodes and the electrolyte were sealed in a glass pressure cell of 135 mL volume custom-made by Exeter Scientific Glass Company (Figure 6.1.). The cell was designed to have metallic leads to connect two electrodes with an external power supply and a gas inlet and outlet. The electrodes were placed into the cell using vacuum stable Teflon bushings (ACE Glass Company). The SSA cell was partially filled with a known volume (30 mL) of aqueous electrolyte solution

(1 M NaCl) to create separate gas and liquid phases in contact with the electrodes. The pressure cell was then placed inside a Julabo F25 water bath with controlled temperature (299.00 +/- 0.01 K) and flushed with pure CO₂ or a gas mixture with simulated flue gas composition (15% CO₂, 85% N₂) for four hours at atmospheric pressure by bubbling through the solution and expelling contaminants through an oil bubbler. After 4 hours, sealing all valves isolates a constant amount of gas inside the cell which is left to equilibrate for 12 hours. Equilibration ensures that the solution is saturated with CO₂ gas, and that CO₂ adsorption onto the high surface area carbon electrode is complete. Most experiments were carried out at room temperature (299 K) but also higher temperatures were used in some experiments (313 K and 328 K). The potential difference across the electrodes was typically cycled between +1 V and 0 V (relative to ground) with 120 min duty cycles (60 min at +1 V and 60 min at 0 V) using a DC power supply (Extech 382260) or a potentiostat (Gamry 3000). The SSA cell was connected to a high precision barometer (Paroscientific, Inc., Digiquartz ® Pressure Instrumentation, Model 6000-16B) which allowed measuring the pressure inside of the SSA cell with an ±0.08 hPa (±0.06 torr) accuracy. For the performance of an SSA experiment one electrode was partially submerged in an electrolyte (hereafter named the working electrode) and the other one was fully submerged in the electrolyte (the counter electrode) so it could not directly interact with the CO₂ in the gas phase (Figure 6.2.). The partially and fully submerged electrodes served as a cathode (-) and an anode (+), respectively. The cell was configured with sorbent pellets in such a configuration (asymmetric configuration) in order to assess whether competitive anode/cathode effects take place. Effects at both the anode and the cathode could be separated by submerging one of the electrodes completely in electrolyte, and the other one

only half way. This way the pressure changes could be attributed to anode or cathode effects depending on the bias of the electrode half way submerged in the electrolyte and half way exposed to the gas. The pressure cell contained also a temperature probe (Rugged Heavy Duty Transition Joint Thermocouple TJ36 Series from Omega ®) which allowed measuring the temperature of the gas during the experiments with an accuracy of 0.01K. The whole setup was further placed in a custom made Styrofoam box to further ensure that there are no significant temperature changes during the experiments. For the purpose of experiments at higher temperatures (40 °C and 55 °C), a light bulb connected to a Powermite heat controller (POWERMITE™ solid-state type-600W capacity heat control) was placed inside the Styrofoam box. The composition of the CO₂/N₂ mixture during charge and discharge of the sorbent electrodes was measured by a Hewlett Packard 5890 series II gas chromatograph with a thermal conductivity detector and a Carboxen™ 1006 plot fused silica capillary column (30m x 0.32 mm) (Supelco).



Figure 6.1. Custom made glass pressure cell used for SSA experiments.

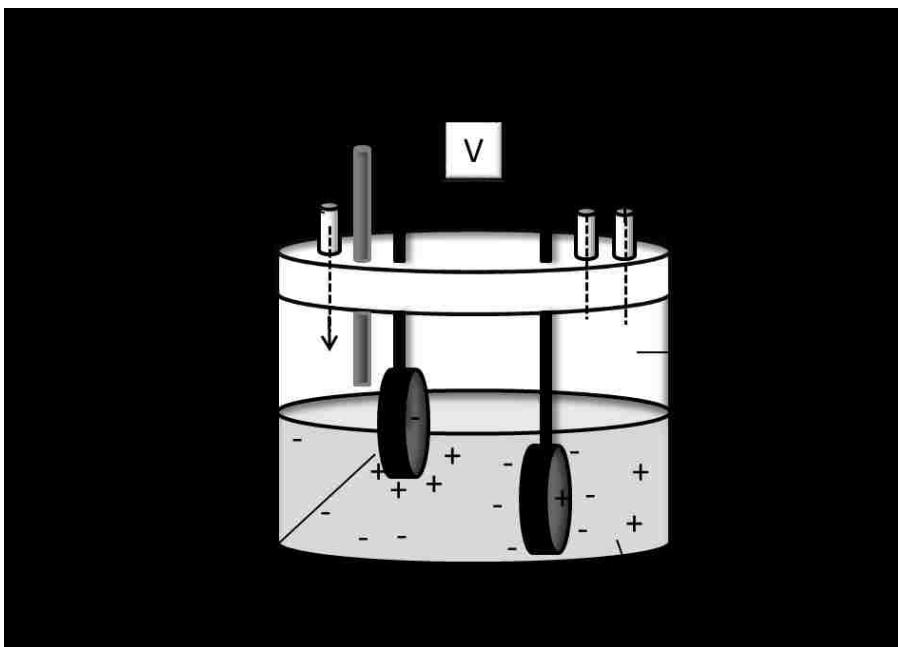


Figure 6.2. Schematic illustration of an SSA cell in which cathode is partially submerged in the electrolyte, while the anode is fully submerged.

6.3. Preparation of electrodes for the SSA experiments

To produce BPL carbon pellets (2 mm thickness and 13 mm diameter), 0.2 g BPL carbon was ground with a mortar and pestle and then mixed with 0.026 g of Polyvinylidene fluoride (PVDF, Sigma Aldrich) binder in 1.3 mL of N-Methyl-2-pyrrolidone (NMP, Alfa Aesar, 99.5%) solvent. The PVDF binder was used due to its non-reactivity with the electrolyte and chemical inertness. Next, the solvent was removed at 120^oC within 12 hours and the powder was pressed in 13mm ID Pellet Die (Carver ®) at 8000 psi using an ICL hydraulic press (ICL ®). The pellets were glued with conducting glue (SPI ®) to a carbon cloth (AvCarb carbon fabric, Fuel Cell Earth) which served as the current collector.

In order to see if the SSA effect can be scaled up monoliths with higher than the nominal pellet mass were prepared. The monoliths (3.7 g or 7.5 g) were prepared by casting a

mixture of 3.7 g BPL carbon with 0.37 g of PVDF binder in 18.5 ml of NMP solvent and 3.7 g NaCl crystals in a 1.3 cm in diameter and 7 cm long glass tube (Exeter Scientific Glass Company). The role of the NaCl was to create macropores and improve kinetics of gas adsorption inside of the monoliths. The monoliths were then dried at 120^oC for 12 hours in order to remove NMP. Then NaCl was leached out with 0.8 L of water within 10 hours and monoliths were dried in a vacuum oven at 100 ^oC overnight. Completion of NaCl removal was checked by measuring the weight difference before and after the leaching process.

6.4. Equipment used for the characterization of the prepared electrodes

The prepared electrodes were characterized with the techniques described in Chapter 4 before the SSA measurements. The results of this characterization can be found in Appendix A of this dissertation.

All the gas/vapor sorption properties of the electrode materials were studied with an Autosorb-1 instrument from Quantachrome Company (Figure 6.3) using N₂ adsorbate at 77 K for measuring surface area of the electrode materials. A CO₂ adsorption isotherm was measured in order to check the CO₂ uptake (how much CO₂ can be adsorbed per gram of material) on BPL carbon. The CO₂ isotherms were measured at 4 different temperatures: 273 K, 298 K, 323 K and 343 K.



Figure 6.3. A photo of the Autosorb-1 instrument at Lehigh University available in Prof. Kai Landskron lab.

Scanning electron microscope was used to check surface physical morphology and structure of the BPL carbon electrode materials prepared for SSA experiments. The SEM systems employed in this work was a Hitachi 4300SE/N. Figure 6.4 shows a photo of this model available at Lehigh University.



Figure 6.4. A photo of the Hitachi 4300SE/N microscope at Lehigh University in department of Materials Science and Engineering [189].

Transmission electron microscope was used to examine the microstructure of the BPL carbon electrode materials prepared for SSA experiments. The TEM systems employed in this work was a JEOL JEM-2000FX with a lanthanum hexa-boride filament. Figure 6.5 shows a photo of this model available at Lehigh University.



Figure 6.5. A photo of the JEOL JEM-2000FX microscope at Lehigh University department of Materials Science and Engineering [189].

The electrochemical characterization of prepared electrodes was done by CV and GCD. All CV and GCD experiments were recorded with a Gamry Potentiostat (GAMRY Reference 3000), shown in Figure 6.6, in a full cell configuration and all plots were generated using Gamry's Analyst software. The reference 3000 is a high-performance Potentiostat/Galvanostat/ZRA with a maximum current of ± 3 A and a maximum voltage

of ± 32 volts. In addition, energy measurements were done with a Voltech PM1000+ power analyzer which can provide measurements of electrical power and energy with 0.1% accuracy. This instrument can measure power consumption from milliwatts to megawatts, providing accurate power and data on products ranging from the tiniest cell phone charger to the electric hybrid bus and has a built-in energy analyzer (watt-hour integrator) for measuring energy consumption over time.



Figure 6.6. A photo of the Gamry Potentiostat/Galvanostat/ZRA model 3000 available at Lehigh University in Prof. Kai Landskron lab.

7. Results of the SSA experiments

In an SSA experiment a known volume of gas (pure CO₂ or a gas mixture which simulated flue gas (15% CO₂, 85% N₂)) was added to the cell and the pressure was recorded during cycles of applied bias. Pressure changes observed were interpreted as changes in moles of gas adsorbed or desorbed on the BPL HSAC electrodes according to the ideal gas law (equation 7-1):

$$\Delta P = \Delta n \left(\frac{RT}{V} \right) \quad \text{Equation 7-1}$$

in which ΔP is a change of the pressure (in Torr) due to adsorption or desorption of CO₂, Δn is a change in the number of moles of CO₂, R is a gas constant = 62.36 $\left(\frac{L \times \text{Torr}}{K \times \text{mol}} \right)$, T is the temperature in which the experiment was done (usually it was room temperature, 25 °C = 298.15 K) and V is the volume of gas.

An increase in the pressure (at constant volume and temperature) was interpreted as gas desorption, a pressure decrease was interpreted as gas adsorption.

All the experiments were done in the set up described in the previous Chapter and shown in Figures 6.1. and 6.2.

7.1. SSA effect during CV and GCD experiments

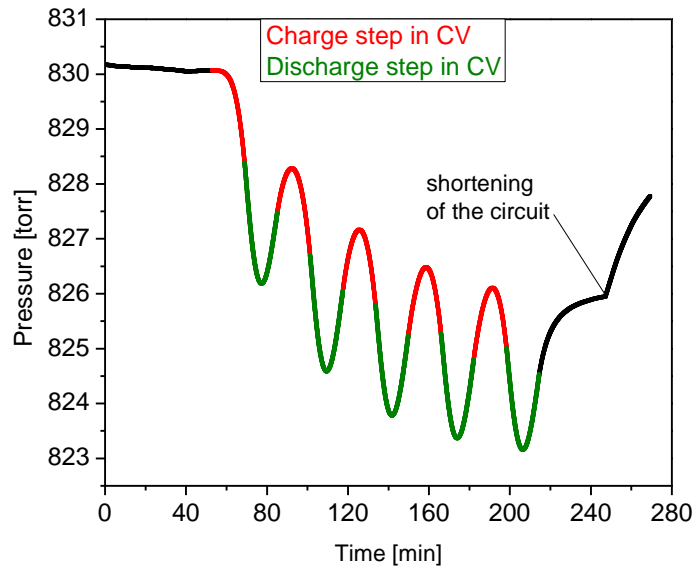
The SSA method is based on repeated capacitive cycling of SC, hence during the SSA experiments the capacitive behavior of the system was verified by CV and GCD which were recorded with a Gamry Potentiostat (GAMRY Reference 3000) in a two electrode cell set up. The electrochemical behavior and the pressure changes were recorded simultaneously. As described in Chapter 4 these electrochemical methods provided the

specific capacitance of electrodes and confirmed that Faradaic reactions did not contribute significantly to the charging current over the range of potentials used during gas sorption experiments.

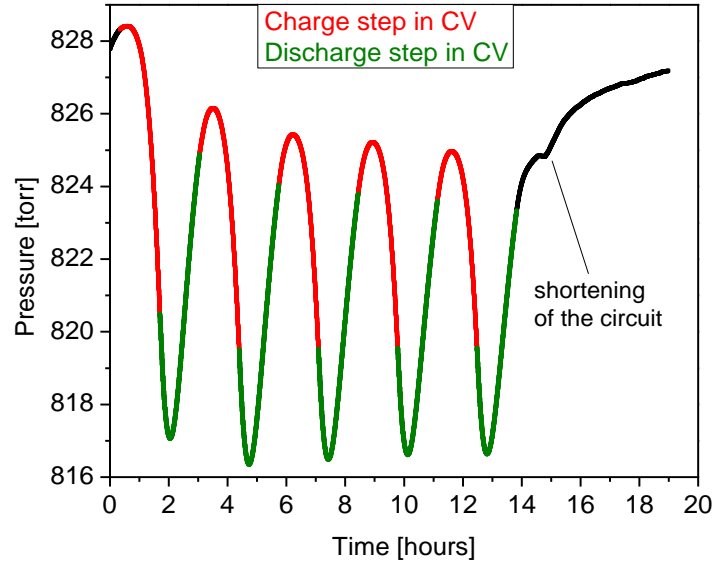
Carbon dioxide capture requires more energy efficient gas separation technologies than the ones which are available at this time. Thus it was important to check how much energy is used during the charge step and how much can be recovered during the discharge step of designed SC since the SSA method relies only on repeated capacitive cycling. The GCD experiments allowed us to calculate the energy used for charge and recovered during discharge by the integration of the area under the GCD charge and discharge curves multiplied by the constant current used accordingly to equation 4-8a,b.

Both the CV and GCD experiments confirmed the capacitive behavior of the system. The half-submerged electrode was working as a cathode and the fully submerged in 1M NaCl electrolyte electrode as an anode to separate effects at both the anode and the cathode as was described in the experimental setup (Chapter 6). Both electrodes had 3.7 g mass and a 1V potential difference was used. In these experiments a mixture composed of 15% CO₂ and 85% N₂ was used as a gas phase. This mixture corresponds to a coal-fired power plant flue gas after water, NO_x and SO_x removal.

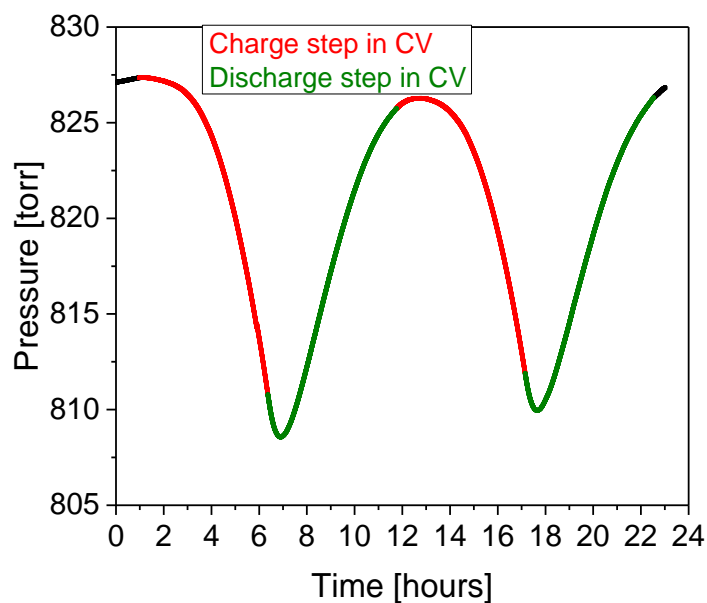
During the CV and GCD characterization pressure changes were measured concurrently in order to see if charging and discharging of a supercapacitor causes adsorption. The pressure changes monitored during these experiments showed pressure decrease during charging and increase by about the same value during discharging (Figure 7.1 and 7.3) and the magnitude of the effect depended on a scan rate (during CV) or constant current value (during GCD) as well as the capacitance of the prepared SC.



a)



b)



c)

Figure 7.1. Pressure changes observed during CV experiments at different scan rates **a)** 1 mV/s, **b)** 0.2 mV/s, **c)** 0.05 mV/s for 3.7 g BPL carbon monoliths in asymmetric configurations with electrode half way submerged working as cathode, 15% CO₂/85% N₂ gas mixture (red – charge step, green – discharge step).

For CV experiments pressure changes of approximately 3 Torr, 9 Torr, and 17 Torr were observed for scan rates at 1 mV/s, 0.2 mV/s, and 0.05 mV/s respectively (C = 12 F, 36 F and 59 F respectively) (Figure 6.1). During the CV experiments the pressure minimum was not at the maximum voltage and this delay was decreasing with decreasing scan rate and was nearly absent when the scan rate was 0.05 mV/s. This phenomenon is due to the different kinetics associated with charging for the different scan rates. For very low scan rates, the capacitance values are higher because the ions have a much longer time to penetrate and reside in all the available electrode pores and form electric double layers, which are needed to generate higher capacitance. At 1 mV/s the capacitance was 13 F, for

0.2 mV/s the capacitance was already 36 F and at 0.05 mV/s it reached 59 F. It can be seen from CV curves (Figure 7.2) for these three scan rates that the current increases with the scan rate. Furthermore, as the scan rate decreases, the voltammogram's 'window' tends to tilt toward the vertical axis, thereby becoming a quasi-rectangle. At higher scan rates transport of ions from the electrolyte to the electrode is limited. Thus, a smaller capacitance is produced. The monoliths used for this experiment were 1 cm thick thus it is better to use a lower scan rate to overcome diffusion limitations of the ions into inner deep gaps and pores of HSAC electrode.

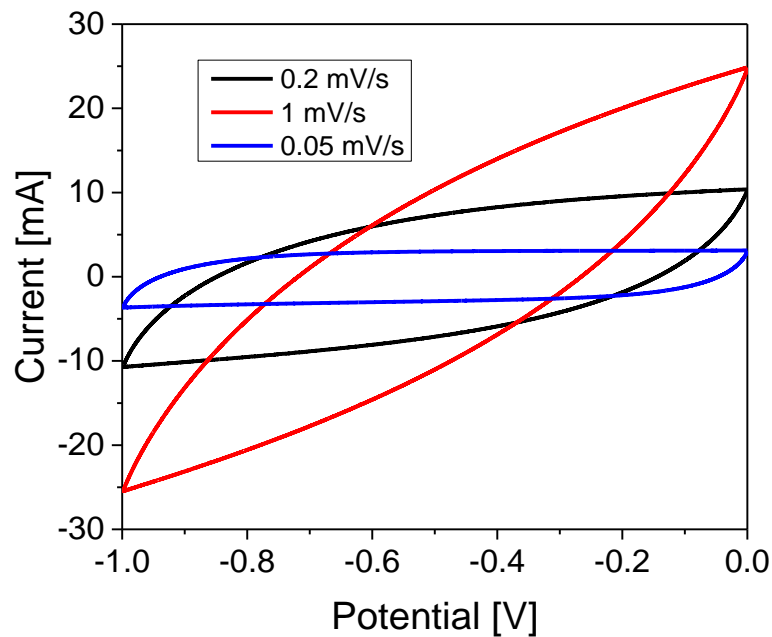
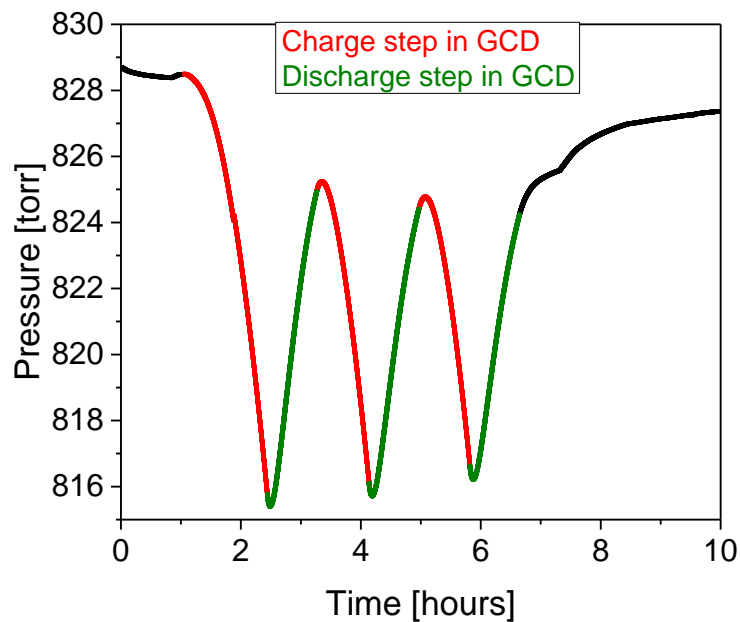


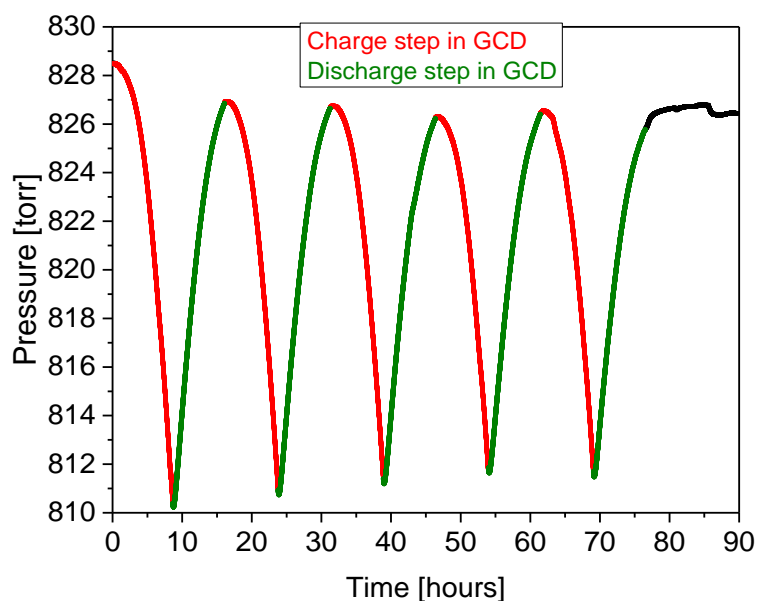
Figure 7.2. CV curves for the 3.7 g BPL carbon monoliths in asymmetric configurations with electrode half way submerged working as cathode at three different scan rates from 0V to 1V potential range.

From the CV experiments it can be observed that the higher the capacitance of the system, the more the pressure changes what is expected because the hypothesis was that adsorption is a function of the capacitance.

For the GCD experiments two constant current values were chosen, 10 mA and 2 mA and the observed pressure changes were 9 Torr and 16 Torr respectively ($C = 39 \text{ F}$ and 59 F respectively) (Figure 7.3). In this case there was no delay for pressure changes as there was during the CV experiments. In CV the potential is ramped at a constant scan rate and the resulting current is being measured. In GCD a constant current is held until a set voltage is reached, making time a dependent variable. At the chosen scan rates and constant currents for the CV and GCD respectively, the GCD experiments take much longer than the CV experiments, hence, the carbon dioxide has a much longer time available for adsorption and desorption.



a)



b)

Figure 7.3. Pressure changes observed during GCD experiments at different constant current **a)** 10 mA, **b)** 2 mA for 3.7 g BPL carbon monoliths in asymmetric configurations with electrode half way submerged working as cathode, 15% CO₂/85% N₂ gas mixture (red – charge step, green – discharge step).

To see if SSA has high energy efficiency, the charge-discharge energy efficiency was calculated according to equations 4.8a and 4.8b and was equal to 42% at 10 mA constant current and 74% at 2 mA constant current (see calculations in an appendix B). The energy efficiency of a supercapacitor is a matter of the charge-discharge rate and the ESR of the capacitor [189]. The smaller the ESR of a capacitor the faster it can be charged at constant efficiency. The slower the charge rate the higher the efficiency at constant ESR. The ESR has been measured from the current resistance (IR) drop and was equal to 17.7 Ohms. As it was discussed in Chapter 4, theoretically, a perfect capacitor would be lossless and have an ESR of zero. Real capacitors suffer from power loss during charge and discharge. This

loss is caused by resistances in the electrical contacts, the electrodes, and the electrolyte. In the designed capacitor this value is higher than in commercially available capacitors, like Nesscap capacitors in which ESR is usually smaller than 0.5Ω . Current commercial SCs can be charged and discharged with around 95% efficiency which suggests that SSA can be still optimized in the future.

Next, it was important to see whether the specific interactions of CO_2 with the cathode and anode are different, since the respective double layers are different. Here, the half-exposed gas electrode acted as the anode, and the fully submerged electrode acted as the cathode. The GCD experiment at 10 mA constant current was performed similarly as in the other configuration. In this case a reversible effect was observed, however, the pressure was increased when the electrodes were charged (Figure 7.4) which indicates that the polarity of the half-submerged electrode can be chosen to either adsorb or desorb CO_2 . When the gas-exposed electrode (half way submerged) is acting as a cathode in 1M NaCl (negative bias), the pressure decreases which indicates that the SSA effect at the cathode leads to increased adsorption of CO_2 , while when the exposed electrode is working as an anode (positive bias) the pressure increases indicating desorption of CO_2 occurred from this electrode. The BPL HSAC electrode has high natural affinity for CO_2 itself. The CO_2 isotherm for a small sample of the prepared electrode with 13% of PVDF binder showed a specific capacity of 31 cc of CO_2/g of sorbent material (see Figure A2 in Appendix A). The specific CO_2 capacity was determined by measuring the isotherm for the pressed BPL carbon electrode with 13% binder on the Autosorb-1 instrument at room temperature. The results of the anodic experiments showed that it is possible to desorb CO_2 which was “naturally” adsorbed on the BLP carbon electrode.

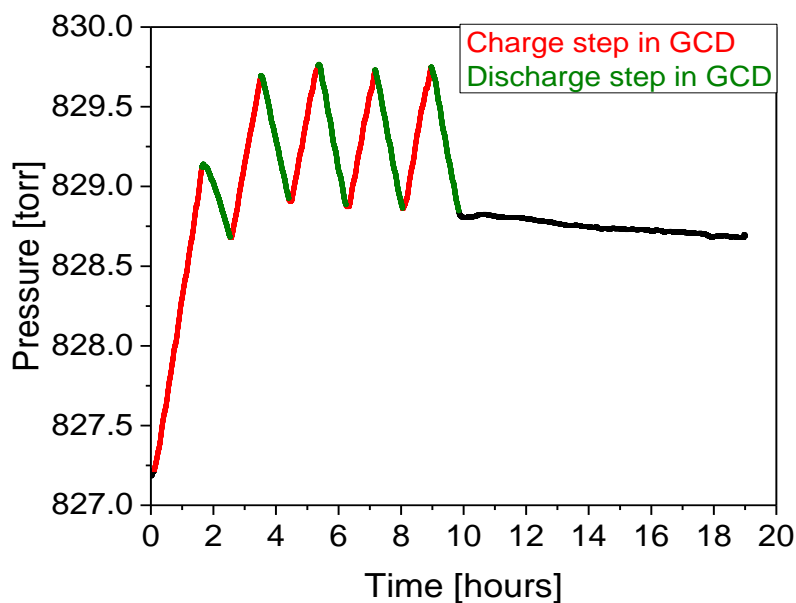


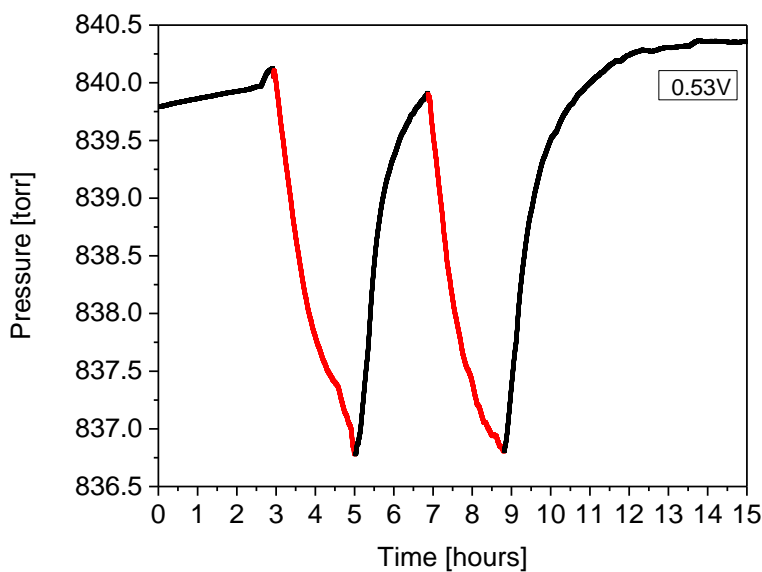
Figure 7.4. Pressure changes observed during GCD experiments at 10 mA ($C = 42\text{ F}$) constant current for 3.7 g BPL carbon monoliths in asymmetric configurations with electrode half way submerged working as an anode, 15% CO_2 /85% N_2 gas mixture (red – charge step, green – discharge step).

As can be seen from the Figure 7.4. the pressure increased almost 2 Torr during the first charging half-cycle while the pressure increased close to 1 Torr upon the second charging. This phenomenon can be explained by the fact that the adsorbed CO_2 was not fully desorbed while switching the polarity of the working electrode. When the electrode started to work as an anode, the charge step speeded up desorption. The opposite effect for the electrode working as the anode suggests that the specific interactions of CO_2 with the cathode and anode must be different, believably due to the different structure of the respective double-layers. The magnitude of the anode effect was much smaller (9 times) in comparison to the effect observed for the cathodic experiment. The significance of this

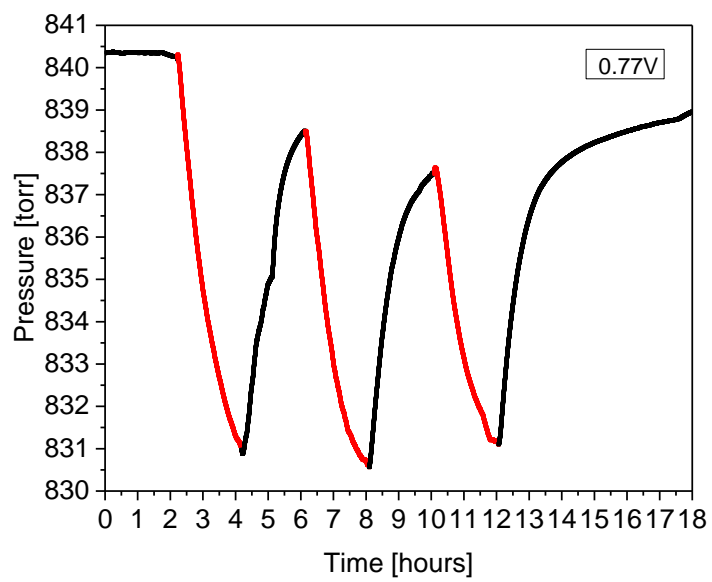
asymmetry in the magnitudes may be reflective of the different molecular-level processes occurring at the anode and cathode, respectively.

7.2. SSA effect at different potentials

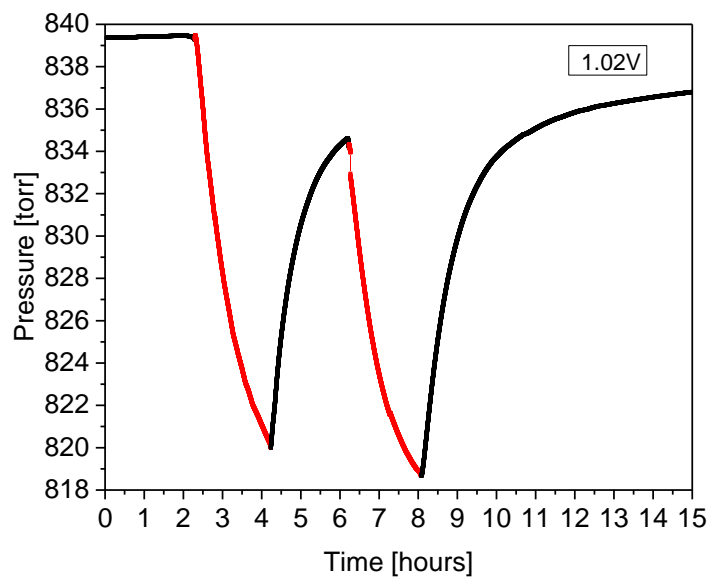
Previous experiments were done at 1 V potential difference using a potentiostat and electrochemical techniques to charge and discharge the supercapacitor. Here, the constant voltage power supply was used in order to see if again the same effects of pressure change can be observed. Four different voltage values, 0.53 V, 0.77 V, 1.02 V, and 1.21 V, were applied with the DC power supply and held for 1 hour after which the potential was turned off and the circuit was shorted. The half-submerged electrode served as the cathode. Again, a 15% CO₂/85% N₂ mixture served as a gas phase. It was observed that the size of the pressure changes depends on the voltage. They increased dramatically from 3 Torr at 0.53 V to 30 Torr at 1.21 V for the first half-cycle (Figure 7.5).



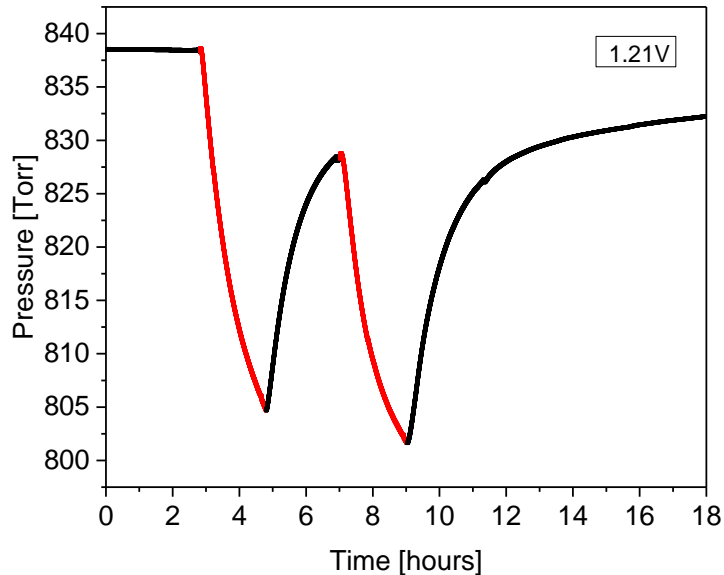
a)



b)



c)



d)

Figure 7.5. Pressure changes at different voltages **a)** 0.53 V, **b)** 0.77 V, **c)** 1.02V and **d)** 1.22 V for 3.7 g BPL carbon monoliths in asymmetric configurations with electrode half way submerged working as cathode. 15% CO₂/85% N₂ gas mixture. Red curve: Electrodes are charged. Black curve: Electrodes are discharged (short-circuited).

It was noticed in all the above experiments that the largest pressure drop was observed for the first charging cycle for the first 1 h adsorption half-cycle, however upon discharging the pressure did not increase by the same value. All second cycles exhibited a declining trend in the pressure change, however, after the final cycle there was a long, slow recovery of the pressure to its initial value. This suggested that the declining SSA effect from cycle-to-cycle might be due to incomplete discharge of the supercapacitor resulted from slow desorption kinetics. That is why, in order to fully discharge the SC and completely desorb CO₂ adsorbed on the electrode, more time is needed.

During these experiments the energy flow was monitored using a power analyzer (Voltech PM1000+) which was placed between the constant voltage power supply and the electrodes. The values of pressure change and energy used for the first charging are shown in Table 7.1.

Table 7.1. Adsorption of CO₂ depending on voltage value.

Voltage [V]	Pressure change [Torr]	Energy used for charging [mWh]	$\Delta P/V^2$ [Torr/V ²]	$\Delta P/E$ [Torr/mWh]	E/V^2 [mWh/V ²]
0.53 V	3.2 torr	3.6 mWh	11.4	0.87	12.9
0.77 V	8.9 torr	7.2 mWh	12.2	1.22	12.2
1.02 V	19.4 torr	13.4 mWh	18.6	1.44	12.9
1.21 V	30.4 torr	17.7 mWh	20.7	1.71	12.1

Energy (E) which is stored in a SC can be calculated by equation 7-2:

$$E = \frac{1}{2} C \times V^2 \quad \text{Equation 7-2}$$

in which C is a capacitance of SC and V is the applied voltage.

The calculated values of $\Delta P/V^2$ and $\Delta P/E$ are increasing with increased voltage value while E/V^2 is almost constant for all the voltages. The capacitive charging behavior of the system can be seen from the fact that E/V^2 is nearly constant. Moreover, since $\Delta P/V^2$ and $\Delta P/E$ are increasing with increased voltage value, SSA can operate more energy-efficiently at higher voltages. Unfortunately, the limiting factor here is the voltage range imposed by the electrolysis of water, which thermodynamically occurs at 1.23 V at 25 °C and decreases with temperature. Thermodynamically oxygen evolution occurs at 1.23 V vs. standard hydrogen electrode (SHE), and hydrogen evolution, per definition, at 0 V vs. SHE.

Recently, it has been demonstrated that neutral aqueous electrolytes such as alkali sulfates could achieve higher voltages with symmetric carbon/carbon capacitors than generally obtained in acidic or basic medium. Béguin et al. demonstrated that a stability potential window of 2.0 V can be achieved with activated carbon in 0.5 mol L⁻¹ Na₂SO₄ [191]. The electrochemical analysis of seaweed-derived carbons in 0.5 mol L⁻¹ Na₂SO₄, demonstrated that the nature of the electrode material and the electrolyte pH influence both the capacitance values and the stability potential window; due to the presence of nitrogenated functionalities in these carbons, the potential window reached 2.4 V in 0.5 mol L⁻¹ Na₂SO₄ [192]. Qu et al. [193] reported that the migration rate of hydrated ions in the bulk electrolyte and within the inner pores of activated carbon increase in the order of Li⁺ < Na⁺ < K⁺, and that the rate performance improves in the order Li₂SO₄ < Na₂SO₄ < K₂SO₄. The highest operating voltage of 2.2 V with an exceptional cycling stability has been demonstrated in Li₂SO₄; Fic et al. have suggested that the stronger hydration of Li⁺ compared to Na⁺ and K⁺ ions is responsible for larger voltage in Li₂SO₄ solution [194]. Also, the use of equation 7-3 to calculate the mass ratio of two electrodes in a hybrid supercapacitor (a hybrid capacitor is the combination of two electrodes, one that stores charge electrostatically, and the other storing charge faradaically) allows the operating voltage range to be extended up to 2 V in neutral media [195]

$$\frac{m^+}{m^-} = \frac{C^- \Delta E^-}{C^+ \Delta E^+} \quad \text{Equation 7-3}$$

in which m⁺ and m⁻ are the masses of positive and negative electrode, respectively and C⁺ and C⁻ the specific capacitance for the positive and negative electrodes, respectively; ΔE⁻ and ΔE⁺ are the potential difference from the open circuit voltage (OCV) to the negative

and positive potential stability limits, respectively. This equation is widely used in literature for assembling hybrid supercapacitors with electrodes having different values of specific capacitance ($C^- \neq C^+$) and/or operating at different voltage ($\Delta E^- \neq \Delta E^+$) [196]. However, this equation may also be applied to non-hybrid systems to increase the operating voltage of the supercapacitors. Chen et al. reported the effect of mass-balancing on the performance of SCs using the same activated carbon in both electrodes in neutral electrolyte [197]. These findings have opened a new door for the aqueous electrolytes and show that SSA might operate at higher voltages boosting the CO₂ adsorption capacity.

7.3. Reproducibility of the SSA effect

In order to probe the repeatability of the SSA experiments three subsequent repetitions of the same experiment were conducted. The gas-exposed electrode was working as the cathode in contact with the 85% N₂/15% CO₂ gas mixture, and the bias was cycled with the Exttech DC power supply from +1 V to 0V with a 2-hour duty cycle.

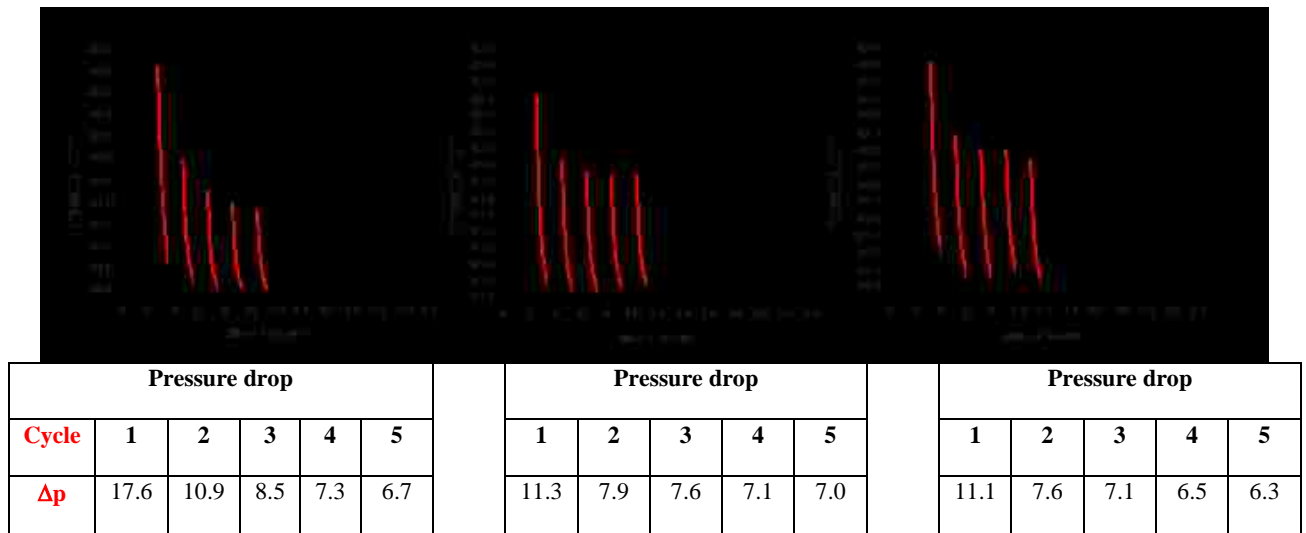


Figure 7.6. Pressure changes during subsequent repetitions of the same experiment for 3.7 g BPL carbon monoliths in asymmetric configurations with electrode half way submerged working as cathode. 15% CO₂/85% N₂ gas mixture. Red curve: Electrodes are charged. Black curve: Electrodes are discharged (short-circuited).

The results, shown in Figure 7.6, reveal that the SSA effect is reproducible from cycle-to-cycle, and from day-to-day. As previously, in all experiments the largest pressure drop was observed for the first charging cycle (17.6 Torr) (the first 1 h adsorption half-cycle). However upon discharging the pressure only increased by 9.5 torr. All further cycles exhibited a gradually declining trend in the pressure change between 10.9 and 6.7 Torr (first experiment in Figure 7.6). This effect was attributed to the incomplete desorption since the pressure did not go back to the original value within one hour desorption half-cycle.

In addition, after the final fifth cycle, there was a long, slow recovery of the pressure to its initial value suggesting that the declining SSA effect from cycle-to-cycle is likely due to incomplete discharge of the supercapacitor and slower kinetics of the discharge step. All further repetitions of this experiment over several days exhibited qualitatively similar trends. On the average of all the cycles the pressure change was *ca.* 7 Torr.

7.4. SSA effect vs. reverse-charging of the working electrode

In Section 7.1 it was already shown that the reverse-charging of the half-submerged working electrode can either actively adsorb CO₂ (cathode) or desorb CO₂ (anode). In those experiments a potentiostat was used to charge and discharge the supercapacitor with the galvanostatic charge-discharge method. Here, a similar experiment was done but a constant voltage power supply was used in order to see if again the same effects of pressure change can be observed while the working electrode has different polarity. Figure 7.7 shows the pressure changes when the working electrode was used as the anode in contact with the 85%N₂/15%CO₂ gas mixture, and a 1 V potential was applied. The duration of a charge-half-cycle and discharge-half-cycle was 1h, respectively.

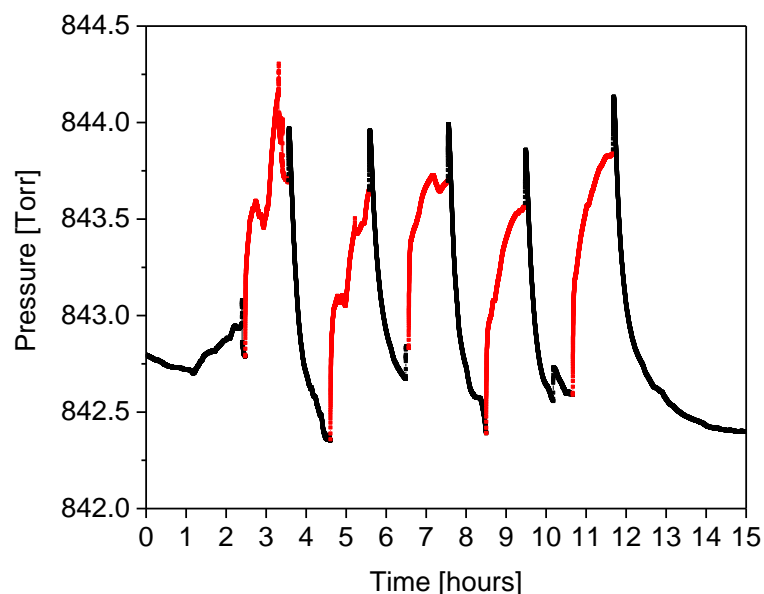


Figure 7.7. Pressure changes observed for 3.7 g BPL carbon monoliths in asymmetric configurations with electrode half way submerged working as an anode while charging with the constant voltage power supply, 15% CO₂/85% N₂ gas mixture (red – charge step, black – discharge step).

As can be seen from the Figure 7.7 the pressure also increased about 1 Torr when a bias was applied and decreased by about the same value when the bias was removed. The desorption of CO₂ from the biased anode is smaller than the adsorption of CO₂ on the biased cathode. The desorption can be explained by the fact that the BPL HSAC electrodes have their own “native” affinity for CO₂ binding.

The results discussed above showed that SSA can be used to actively adsorb or desorb CO₂ simply by directly switching the polarity of the bias applied to the half-submerged electrode from cathodic (adsorption) to anodic (desorption) configuration. Results from this type of experiment are shown in Figure 7.8.

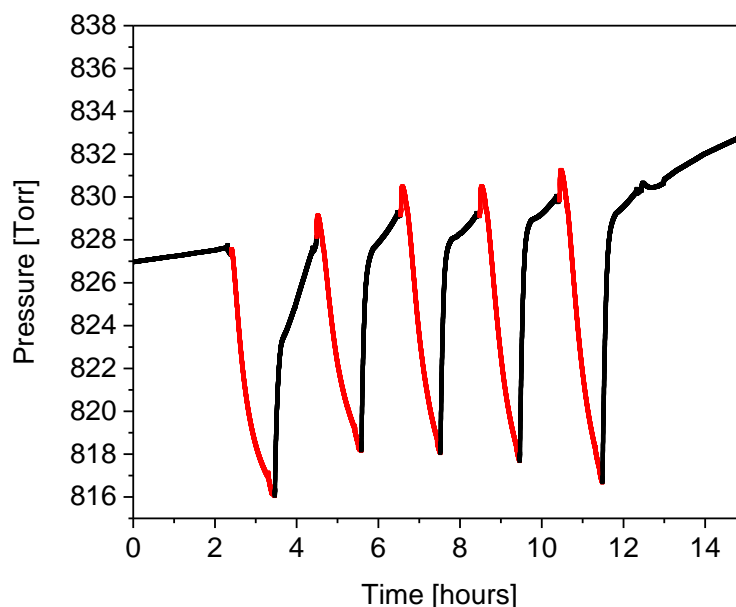


Figure 7.8. Pressure changes observed during cathodic-anodic half cycles for 3.7 g BPL carbon monoliths in asymmetric configurations with electrode half way submerged working alternately as a cathode and as an anode while using the constant voltage power supply, 15% CO₂/85% N₂ gas mixture (red – cathodic step, black – anodic step).

In this case during the first half-cycle (adsorption) the half-submerged electrode was working as a cathode and a +1 V potential was applied to the fully submerged electrode. Then the leads were reversed for the desorption step in which the working electrode served as the anode. It can be seen from Figure 7.8 that reversible pressure changes of around 11 Torr were possible for all five adsorption-desorption cycles. What is also important, reversing the polarity of the applied bias during desorption cycles leads to full cycle-to-cycle reversibility with equal full-range adsorption and desorption magnitudes.

7.5. The influence of electrode infiltration on the SSA effect

It was observed that the efficacy of the 3.7 g BPL electrodes increased with continued usage. The pressure response during subsequent, repeated cathodic cycles increased from the average of 7 Torr to 16 Torr (compare Figure 7.6 with Figure 7.9).

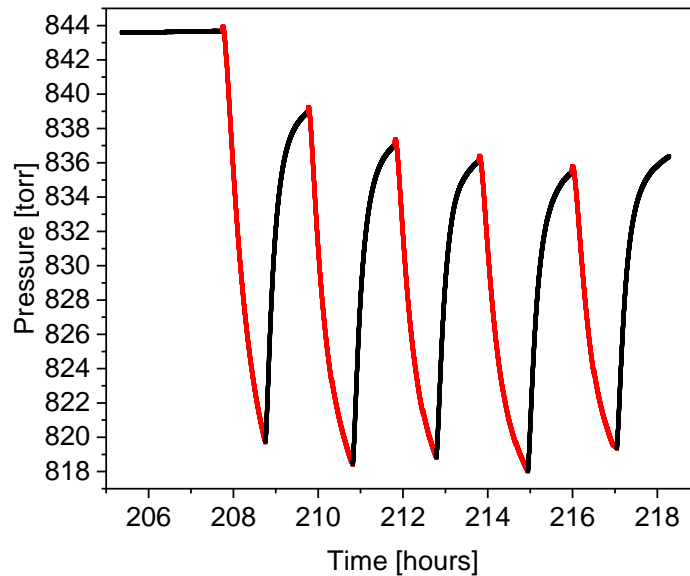
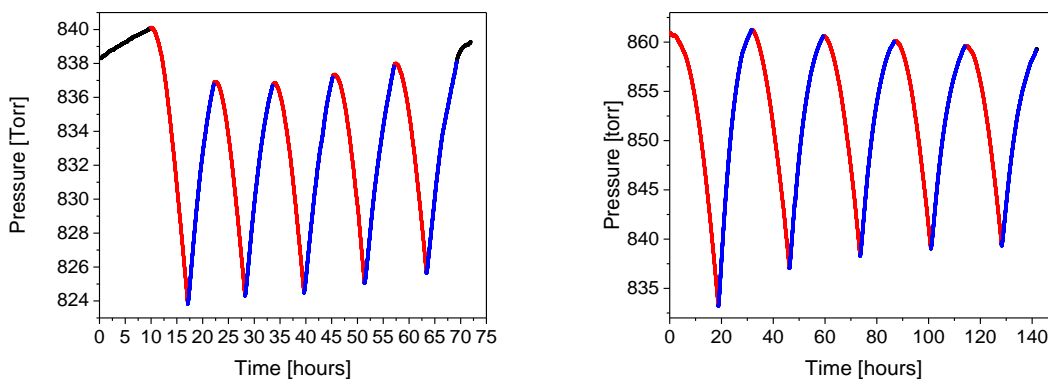


Figure 7.9. Pressure changes observed for 3.7 g BPL carbon monoliths after being used for a longer time in asymmetric configurations with electrode half way submerged working as a cathode while charging with the constant voltage power supply, 15% CO₂/85% N₂ gas mixture (red – charge step, black –discharge step).

From Figure 7.9 it can be seen that the same setup of electrodes was in use for almost 9 days before the experiment was started (206h). In the context of the results from Fig. 7.6 the above results (Fig. 7.9) showed that the SSA effect is not only reproducible from cycle to cycle but also can get bigger after long, subsequent charging and discharging. This increase may be attributed to an increase in the degree of infiltration of electrodes upon repeated charging and discharging and hence increase in capacitance of the carbon electrodes. The same effect was also observed in experiments with the larger (7.5 g)

electrodes (7.5 g) when running cathodic GCD experiments at 2 mA constant current. The first experiment was done two days after the electrodes were submerged in the electrolyte, and the next one was done 21 days after the first experiment (Figure 7.10). It must be also said that between these days other experiments were done (such as charge-discharge with the power supply) and the system was in use all the time.



1	charge step	16.23 torr decrease	53.07	1	charge step	27.64 torr decrease	140.3
2	charge step	12.65 torr decrease	46.19	2	charge step	24.04 torr decrease	111.3
3	charge step	12.39 torr decrease	46.50	3	charge step	22.17 torr decrease	108.7
4	charge step	12.27 torr decrease	47.23	4	charge step	20.82 torr decrease	108.0
5	charge step	12.33 torr decrease	48.02	5	charge step	20.26 torr decrease	107.9

a)

b)

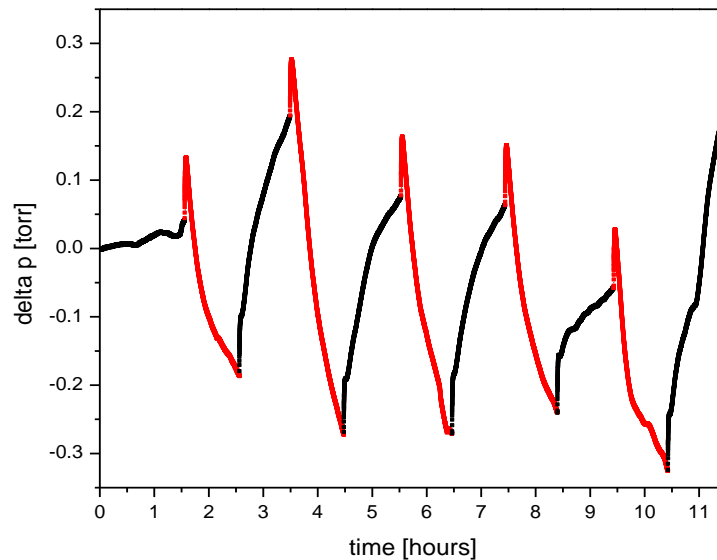
Figure 7.10. Comparison of pressure changes during GCD experiment at 2 mA constant current within 0 V to 1 V potential range done at different times: **a)** 2nd day of experimental setup, **b)** 23rd day of experimental setup for 7.5 g BPL carbon monoliths in asymmetric configurations with electrode half way submerged working as cathode, 15% CO₂/85% N₂ gas mixture (red – charge step, blue –discharge step).

From the above figure it is clear that the pressure change increased almost twice (from an average of 12 Torr to an average of 22 Torr) with time. Electrode capacitance was also

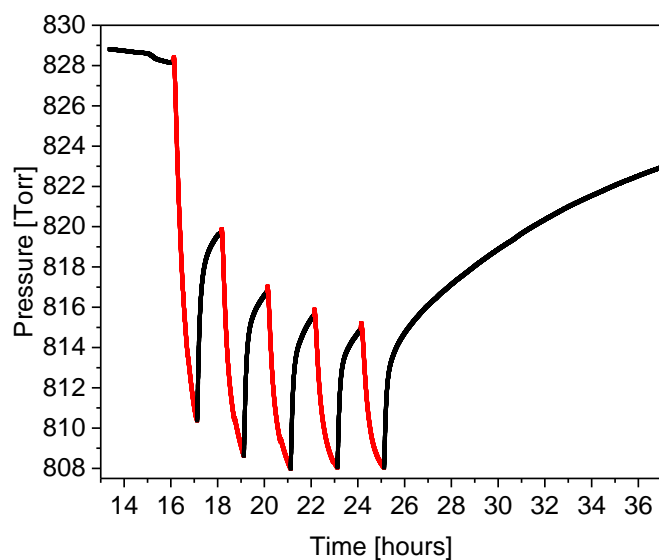
found to depend on time that electrodes were soaked in the electrolyte (from $\overline{44}$ F to $\overline{102}$ F).

7.6. Scalability of the SSA effect

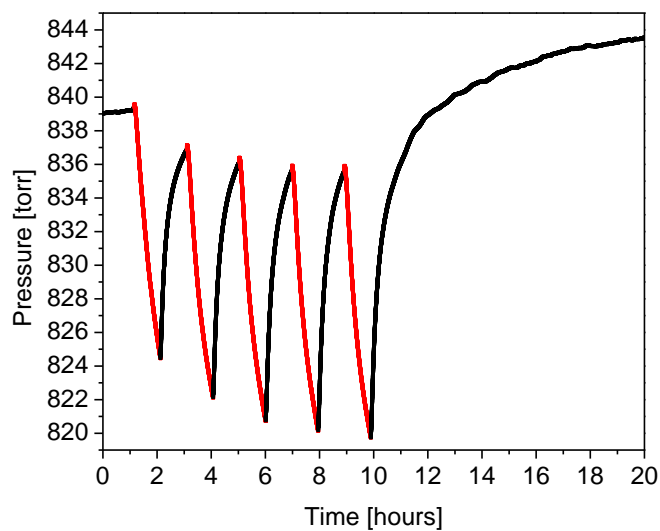
In order to see if it is possible to scale up the SSA effect, experiments with three different masses (0.2 g, 3.7 g and 7.5 g) of BPL carbon electrodes were done at the same conditions (electrode half-way submerged served as the cathode, 15% CO₂/85% N₂ gas mixture). The constant voltage power supply was used to charge electrodes at 1 V with a 2 hour duty cycle. It was observed that the SSA effect scales up proportionally with the mass of the sorbent electrodes (Figure 7.11).



a)



b)



c)

Figure 7.11. Pressure changes for three different masses of electrodes: **a)** 0.2 g ($\overline{\Delta P} = 0.4$ Torr), **b)** 3.7 g and ($\overline{\Delta P} = 7$ Torr) **c)** 7.5 g. ($\overline{\Delta P} = 14$ Torr) in asymmetric configurations with electrode half way submerged working as a cathode. 15% CO_2 /85% N_2 gas mixture. Red curve: Electrodes are charged at 1V. Black curve: Electrodes are discharged (short-circuited). For a) baseline was subtracted for clarity.

For the largest electrodes the first 1 hour adsorption half-cycle showed again the largest pressure drop but upon discharging the pressure did not increase to its original value. All further cycles exhibited a gradually declining trend in the pressure change and after the last cycle the pressure recovered to its initial value but at a very slow rate. The average pressure drop during the charge steps was 7 Torr for the 3.7 g electrodes and 14 Torr for the 7.5 g electrodes.

From Figure 7.7 it can be observed that increasing the mass of the electrode by a factor of 18 (from 0.2 g to 3.7 g) increased the SSA effect 18 times (from 0.4 Torr to 7 Torr). Similarly, increasing the mass of the electrode by the factor 2 (from 3.7 g to 7.5 g), increased the SSA effect by 2 (from 7 Torr to 14 Torr). Since gas separations are often done at large scale, the possibility of the scaling of the SSA effect with the mass of electrodes is an important fact.

7.7. The gas selectivity of the SSA effect

In order to see if SSA can actively separate CO₂ from a CO₂/N₂ mixture, the gas phase composition was investigated upon adsorption and desorption by gas chromatography (GC). At the end of each charge and discharge half cycle 10 µL aliquots of gas were sampled with a microliter syringe and the composition of the gas was analyzed by the GC. For the smallest size electrode pairs (0.2 g) for which the 0.4 Torr pressure change was observed (Figure 7.11a) there was no change in composition observed with GC what can be explain by the fact that the expected composition change was only 0.06% (calculations in appendix B) which is below the detection limits of the GC technique. In order to monitor the composition of CO₂ during charge and discharge the pressure change needed to be at

least 17% larger to see at least 1% change ($\frac{0.40 \text{ Torr}}{0.06\%} = 6.67 \text{ Torr}$). For this reason larger monolithic pieces of BPL carbon were prepared (3.7 g and 7.5 g) for which 7 Torr and 14 Torr pressure changes were observed (Figure 7.11b,c) while charging with the power supply. The GC measurements showed that it is possible to separate CO₂ from N₂ in the mixture. For the 3.7 g monoliths it was observed that approximately 7 Torr pressure change corresponds to 1% change in CO₂ content while for 7.5 g electrodes 14 Torr pressure change would give an average of 2% change (Table 7.2). It is also important to add here that after the final cycle the pressure and, hence, composition of CO₂ went back to the same value as before the experiment.

Table 7.2. Change in gas composition during SSA experiment with 3.7 g and 7.5 g electrodes.

Mass of electrode		3.7 g		7.5 g	
Cycle number		Pressure change [torr]	Change in composition of CO ₂ [%]	Pressure change [torr]	Change in composition of CO ₂ [%]
1	charge step	-11.3	-2.1%	-14.91	-2.7%
	discharge step	+8.0	+1.1%	+12.42	+1.7%
2	charge step	-7.9	-1.1%	-14.86	-1.9%
	discharge step	+7.8	+1.0%	+13.93	+1.9%
3	charge step	-7.6	-1.1%	-15.27	-2.1%
	discharge step	+7.2	+1.1%	+14.88	+1.8%
4	charge step	-7.1	-1.4%	-15.48	-2.2%
	discharge step	+7.0	+1.0%	+15.40	+2.3%
5	charge step	-7.0	-1.4%	-15.84	-2.5%
	discharge step	+6.9	+1.3%	+16.05	+2.8%

To measure the gas separation even more precisely, electrodes with the highest mass (7.5 g) were used and a GCD experiment was performed at 2 mA constant current within 0 V to 1.2 V potential range with the same gas mixture. Reversible pressure changes ranging from 47 Torr (first cycle) to 39 Torr (last cycle) were measured (Figure 7.12).

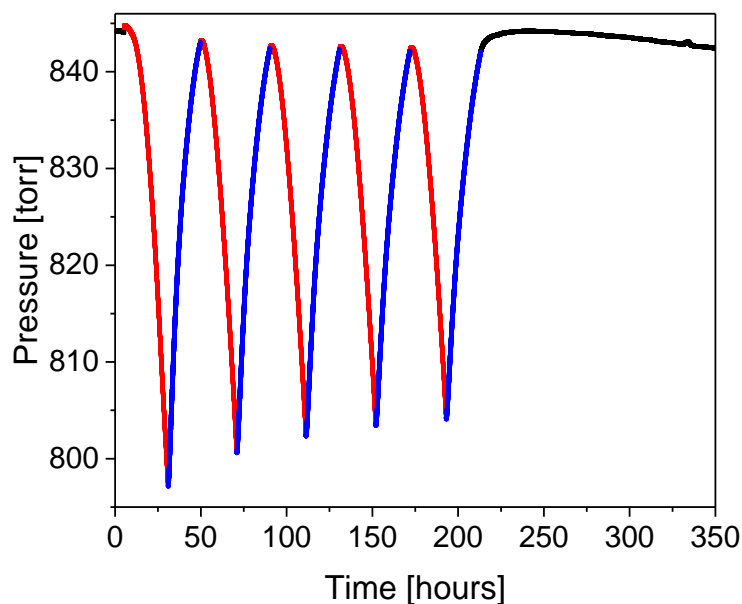


Figure 7.12. Pressure changes during GCD (cathodic) at 2mA constant current within 0V to 1.20V potential range for 7.5 g BPL carbon electrodes in asymmetric configurations with electrode half way submerged working as a cathode. 15% CO₂/85% N₂ gas mixture. (red – charge step, blue –discharge step).

Table 7.3 shows the results of the GC measurements. At the end of the adsorption (charging) cycles the percentage of CO₂ in the gas mixture was reduced by values between 6.5% and 5.9%. During desorption (discharging) cycles, the CO₂ content increased by approximately the same extent (6.1 to 5.4%). It was expected from previous GC measurements that a 42 Torr pressure change should give 6% change in CO₂ since 7 Torr and 14 Torr gave 1% and 2 % respectively (see calculations in Appendix B) and exactly

this value was observed. The SSA effect of such a system was determined to be 6%, which can be defined as 6% enhancement of the sorption capacity in the charged state *versus* the uncharged state. These results further confirmed actual gas separation of CO₂ and N₂ from the mixture and showed that the effect is selective for CO₂ over N₂. There is good agreement between reversibly adsorbed CO₂ calculated from the measured composition and the measured pressure changes what further confirms that SSA is highly selective for CO₂ over N₂.

Table 7.3. Change in gas composition during SSA experiment with 7.5 g electrodes. Cycle 3 and 5 ended during the night and GC experiments were not performed for lab safety reasons.

Cycle number		Pressure change [torr]	Change in composition of CO ₂ [%]
1	charge step	-47.7	-6.5%
	discharge step	+46.1	+6.1%
2	charge step	-42.6	-6.0%
	discharge step	+42.0	+5.9%
3	charge step	-40.3	Not measured
	discharge step	+40.3	Not measured
4	charge step	-39.1	-5.5%
	discharge step	+38.9	+5.4%
5	charge step	-38.4	Not measured
	discharge step	+38.0	Not measured

Experiments with pure N₂ were carried on in exactly the same way as with the gas mixture or pure CO₂. Monoliths with a mass of 7.5 g were used to ensure the maximum sensitivity of the experiment. Figure 7.13 shows the pressure response upon charging and discharging the BPL carbon monoliths. In this experiment the half-submerged electrode was used as the cathode. Before the experiment, electrodes were cleaned and outgassed in a vacuum oven at 100 °C for 12 hours to make sure that no air was adsorbed. Further, electrodes were closed in the SSA cell and flushed for 4 hours with helium gas which does not adsorb on

the carbon surfaces. To make sure that the electrolyte does not contain any air, a fresh 1 M NaCl aqueous solution was prepared under vacuum conditions according to the following steps: first 100 mL of distilled water was redistilled under helium. Second, 5.8 g of NaCl was placed in a round bottom 2-neck flask. Next, the NaCl was outgassed at 100°C under vacuum to remove any air or moisture. Then, 100 mL of redistilled water was moved with a syringe into the flask containing NaCl crystals to make 1 M aqueous NaCl electrolyte. This electrolyte was further moved with a syringe to the SSA cell.

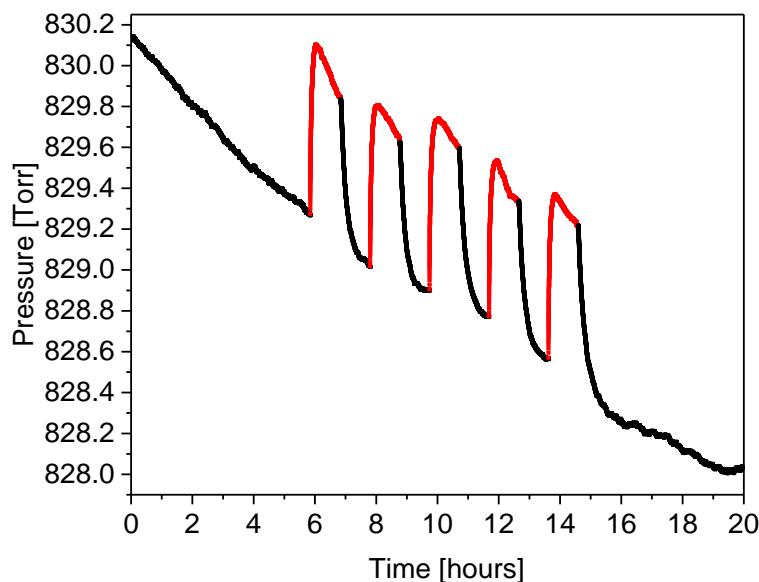


Figure 7.13. Pressure changes during 1 hour cathodic half cycles in pure N_2 . Red curve: Electrodes are charged at 1V. Black curve: Electrodes are discharged (short-circuited).

From Figure 7.13 it can be observed that the pressure is going slightly up while charging the electrodes what suggests that N_2 is actually slightly repelled from the BPL carbon electrode what further confirmed selectivity of CO_2 over N_2 .

Next, an experiment with helium was performed as a control experiment with the purpose to differentiate between gas adsorption effects and other effects that may influence the gas pressure during the charging and discharging (Figure 7.14). Helium can be assumed to not adsorb significantly on the carbon surfaces and therefore sorption effects can be distinguished from other effects. Before this experiment the electrodes were also cleaned and outgassed for 12 hours and then the system was purged with He for 4 hours. The electrolyte was prepared under vacuum conditions. It was observed that there were practically no pressure changes upon the applied bias for the helium control experiment which further confirmed that the observed SSA effect is specific to CO₂, indicating a high selectivity for CO₂ over N₂ and also He.

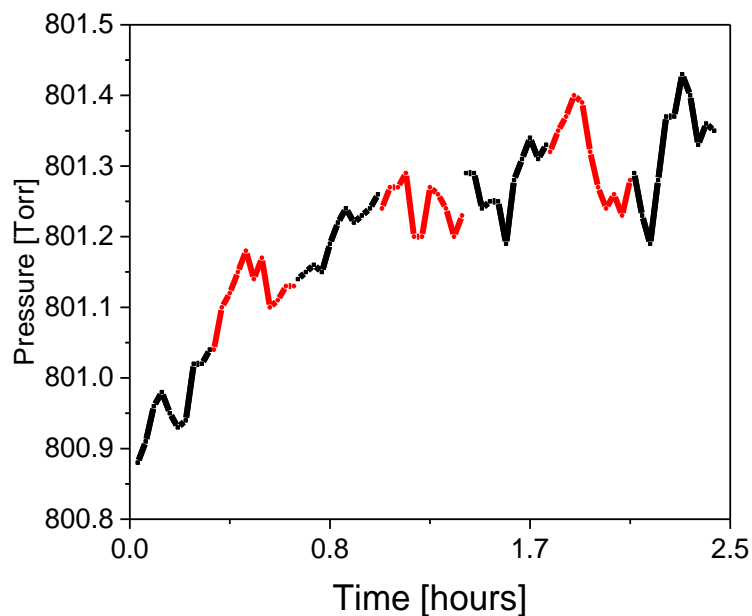
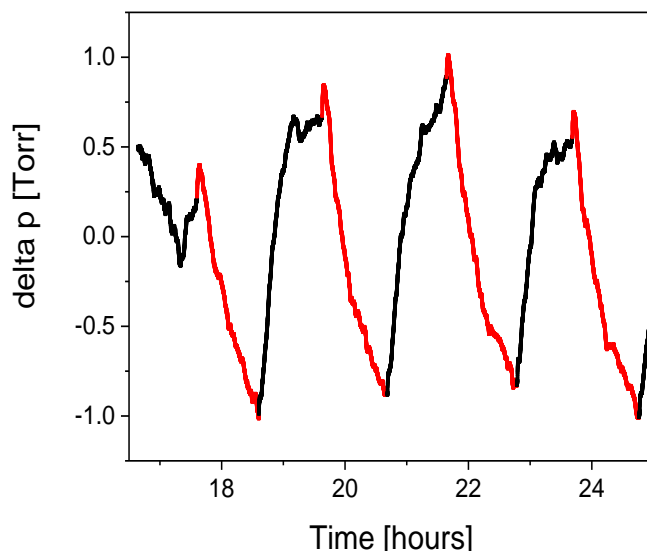


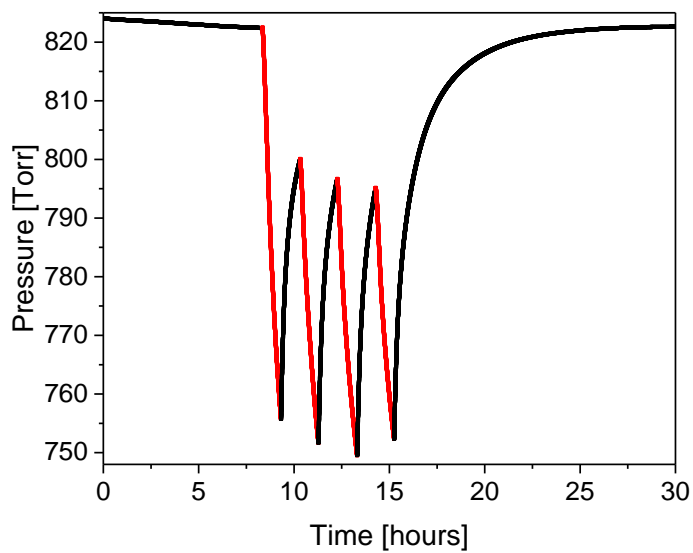
Figure 7.14. Pressure changes during 1 hour cathodic half cycles in pure He. Red curve: Electrodes are charged at 1V. Black curve: Electrodes are discharged (short-circuited).

7.8. Dependence of the SSA effect on CO₂ partial pressure

According to Dalton's Law of Partial Pressures (1) each gas in a mixture of gases exerts a pressure, known as its partial pressure that is equal to the pressure the gas would exert if it were the only gas present; (2) the total pressure of the mixture is the sum of the partial pressures of all the gases present. Flue gases and engine exhaust gases have low CO₂ partial pressures with CO₂ concentrations of typically 15 vol%. As a consequence, it was important to investigate the dependence of the SSA effect on the CO₂ partial pressure. Experiments with pure CO₂ and with a gas mixture of 15% CO₂/85% N₂ were done with the cathode half-way exposed to the gas for 0.2 g BPL HSAC electrodes (compare Figure 7.13a with 7.11a). For both the pure CO₂ and the gas mixture, it was possible to see a clear pressure drop of 1.5 Torr and 0.4 Torr respectively when the bias was applied. What is more, even though the partial pressure of CO₂ in a gas mixture was 6.7 times smaller, the corresponding pressure response decreased by a factor of only 3.7. The same comparison was also made for larger monoliths (compare Figure 7.11c with 7.13b). These experiments were carried out as previously described: 7.5 g BPL carbon electrodes were used, the gas-exposed electrode was biased as the cathode and the bias was cycled from +1V to 0V with two hour duty cycles with the constant current power supply. Again experiments with pure CO₂ resulted in an approximate four-fold increase (48 Torr) in the effect compared to a 15%/85% CO₂/N₂ mixture (14 Torr) but the CO₂ partial pressure increased by a factor of 6.7. From these results it can be concluded that there is a less than proportional dependence of the effect on CO₂ partial pressure.



a)



b)

Figure 7.15. Pressure changes during 1 hour cathodic half cycles in pure CO_2 for a) 0.2 g BPL HSAC pellets and b) 7.5 g BPL HSAC monoliths in asymmetric configurations with electrode half way submerged working as a cathode. Red curve: Electrodes are charged at 1V. Black curve: Electrodes are discharged (short-circuited). For a) baseline was subtracted for clarity.

7.9. SSA effect in thermodynamic equilibrium

From all of the above figures illustrating the pressure changes it can be observed that after one hour for each half cycle the pressure is not equilibrated. Therefore the size of the SSA effect for the 15% CO₂/85% N₂ gas mixture was measured in thermodynamic equilibrium (at 1.0 V and 1.2 V for the 7.5 g monoliths) to find out how much time is needed to fully adsorb and desorb CO₂ upon charging and discharging of the carbon supercapacitor. Here the time for a single adsorption half-cycle was extended until no further pressure decrease was observed. The pressure changes were confirmed in two independent experiments. As can be seen from Figure 7.16 the SSA effect saturates at a pressure drop of 54 Torr at 1V and at 74 Torr at 1.2V.

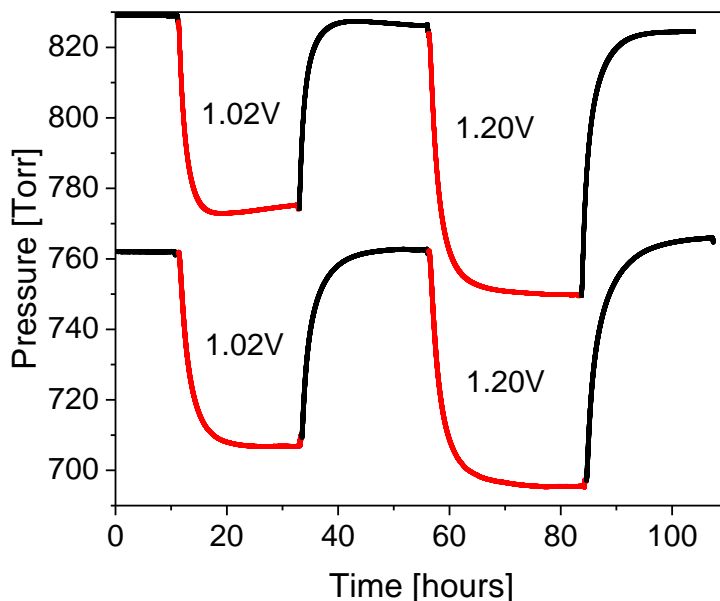


Figure 7.16. Pressure changes in thermodynamic equilibrium for SSA at 1.0 V and 1.2 V for 7.5 g BPL carbon monoliths in asymmetric configuration with 15% CO₂ and 85% N₂ gas mixture. Red curve: Bias ON. Black curve: Bias OFF (short-circuited).

The gas composition was measured at the end of each half cycle. The gas composition change for the experiment at 1.0 V was 7.1% and for the 1.2 V experiment the change was 10.1% what means that at 1.2V about two thirds of the CO₂ has been removed from the gas mixture (0.1 atm out of 0.15 atm CO₂). As can be seen from Figure 7.16 discharge of the electrodes led to full recovery of the pressure which was also confirmed by the GC measurements. The equilibrium pressure changes showed that SSA can be fully reversible and CO₂ can be successfully adsorbed and desorbed. The same experiment was also done with pure CO₂ and the results are shown in Figure 7.17. For pure CO₂ the effect was 97 Torr at 1 V and 109 Torr at 1.2 V that further confirmed the less than proportional relationship between the pressure changes and the CO₂ partial pressure. What is more, the less than proportional relationship is even more pronounced in equilibrium since at thermodynamic equilibrium the pressure changes only double when the CO₂ partial pressure increases from ca. 0.15 atm to ca. 1.

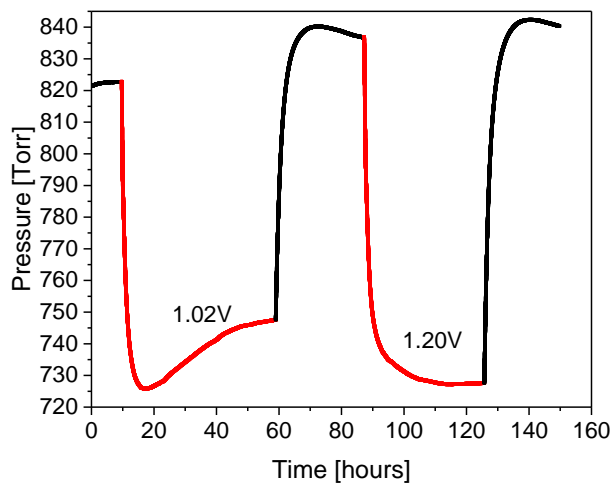


Figure 7.17. Pressure changes in thermodynamic equilibrium for SSA at 1.0 V and 1.2 V for 7.5 g BPL carbon monoliths in asymmetric configuration with pure CO₂. Red curve: Bias ON. Black curve: Bias OFF (short-circuited).

Since the volume of the gas sorption cell and the mass of the electrodes are known the magnitude of the effect in mol of gas per kilogram of carbon in equilibrium can be calculated. From the pressure change in Figure 6.15 it can be calculated that at 1.2V 0.05 mol CO₂/kg of sorbent material can be reversibly adsorbed at 299 K and a CO₂ partial pressure of 0.15 atm (see calculations in an appendix). If this value would be compared with a native sorption capacity of BPL carbon which is 0.24 mol CO₂/kg of sorbent at the same conditions this is relatively little but it is important to say that the native loading for BPL carbon is for a completely dry CO₂ while in all SSA experiments the CO₂/N₂ gas mixture is saturated with water vapor from aqueous electrolyte.

7.10. SSA effect at different temperatures.

In post-combustion processes, the flue gas temperature is typically within the range of 50 to 120°C [198]. Thus, SSA experiments were done at three different temperatures, 26 °C, 40 °C and 55 °C in order to check if the SSA effect depends on temperature. Higher temperatures could not be applied due to maximum operating temperature of the pressure sensor (60 °C). These experiments were done with the 15%CO₂/85%N₂ gas mixture in thermodynamic equilibrium. It was observed that the effect of adsorption/desorption of CO₂ is only weakly dependent on the temperature (Figure 7.18). However, it was observed that the higher the temperature, the more time is needed for the system to reach thermodynamic equilibrium. This observation was surprising because usually equilibrium is established faster at higher temperatures due to higher ion mobility. Surprising was also that the SSA effect stays the same with increasing temperature. In the activated carbon based supercapacitors an increase in the operating temperature causes an increase in the overall capacitance [199,200]. In SSA an increase in capacitance with temperature was

observed. At 26 °C the capacitance was 102 F while at 40 °C the capacitance was already 172 F (from CCD at 2 mA constant current and 0 V to 1V potential range). It was observed previously that the higher the capacitance of the system, the higher the SSA effect. The higher capacitance requires a longer time until the equilibrium is reached because there is greater degree of electrode infiltration what leads to an increase in the SSA effect. On the other hand, the CO₂ adsorption capacity of solid adsorbents decreases with temperature (see Appendix A). The solubility of CO₂ in water decreases with an increase in temperature. It can be concluded that the two effects compensate, that is why the SSA effect did not increase with increased temperature.

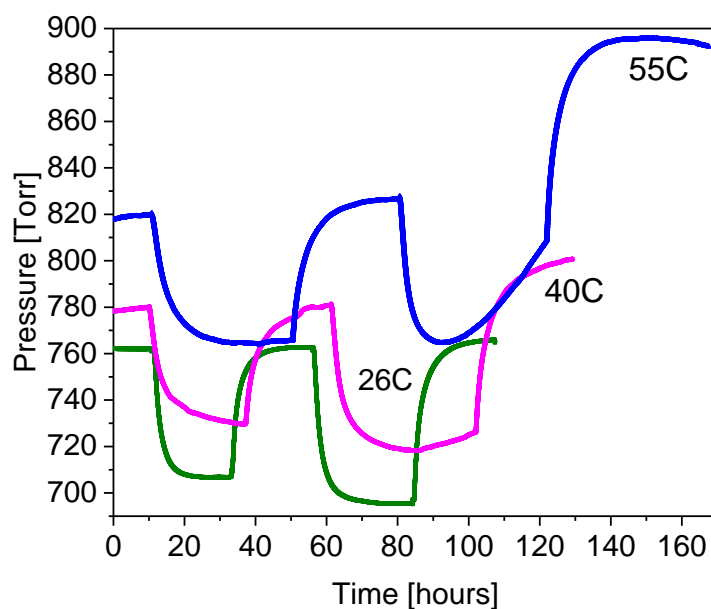


Figure 7.18. Pressure changes at different temperatures at 1.0 V (first cycle) and 1.2 V (second cycle) at 26 °C (green), 40 °C (purple), and 55 °C (blue) for 7.5 g BPL carbon monoliths in asymmetric configuration with 15% CO₂ and 85% N₂ gas mixture.

At 1.02 V pressure changes of 55, 50, and 55 Torr were observed at temperatures of 26, 40, and 55 °C respectively. At 1.2 V the effect was increased to 67 Torr at 26 °C. At 40 and 55 C° it was observed that the pressure first decreased and then slowly increased and this phenomenon was especially seen at 55 °C. The reason for this effect could be in overcoming the overvoltage that prevent electrolysis at 1.23 V. Overvoltage is the extra voltage that must be applied to a reaction to occur at the rate at which it would occur in an ideal system. This overvoltage must be applied due to the resistance inside the electrolyte, electrode, and also the reaction system itself. Under ideal conditions, a potential of 1.23 volts is large enough to oxidize water to O₂ gas. Under real conditions, however, it can take a much larger voltage to initiate this reaction. High temperature can cause overvoltage to be reduced. At the end of the experiment at 55 °C it can be observed that the pressure is higher than in the beginning of the experiment that further suggests the electrolysis of solvent and evolution of gas.

7.11. Possible mechanisms for SSA

Since experiments without any electrolyte did not show any pressure changes at voltages up to 5 kV it is obvious that the electric double layer is essential for the SSA effect. The question is how this SSA effect occurs. Principally, the interactions between the electrode and the CO₂ gas could happen *via* one of the following molecular mechanisms:

- a) adsorption of CO₂ at the gas-solid interface,
- b) adsorption of CO₂ at the liquid-solid interface.

Physisorption at a gas-solid interface is kinetically very fast and typically complete within seconds to minutes, however the SSA effect requires several hours to fully adsorb or desorb

CO₂ (see Figure 7.16) what suggests that the adsorption does not take place at the gas-solid interface but rather within the electrical double layer at the liquid-solid interface which is consistent with slow adsorption kinetics. During all the SSA experiments asymmetry between the interactions of CO₂ with the partially and fully submerged electrode in the cell was observed. The enhanced adsorption of CO₂ during cathodic cycles and desorption during anodic cycles could be observed which indicates that the specific interactions of CO₂ with the cathode and the anode must be different since structures of the respective double layers are different. Calculations in Chapter 5 showed that it is possible that the number of delocalized π -electrons in the carbon upon charge and discharge may affect the sorption behavior of a significant number of CO₂ molecules.

In the SSA experiments it was also observed that with time the capacitances become larger and hence, the SSA effect becomes also larger (Figure 7.10). It can be concluded that the area of the wetted interface has likely increased. In addition, electrowetting could play a significant role. Electrowetting is the modification of the wetting properties of a surface (which is typically hydrophobic) with an applied electric bias. As it was said before nanoporous carbons are relatively hydrophobic materials because of their non-polar C-C bonds however, when the carbon capacitor is charged the area of the wetted interface of the gas-exposed electrode increases while the gas-solid interface decreases. This phenomenon would also speak against adsorption at the gas-solid interface as the explanation for the SSA effect, since pressure swings have increased, while the area of the gas-solid interface has decreased.

On the other hand the SSA effect could also occur due to changes in the solubility of the CO₂ in the electrolyte. When the capacitor is charged, the ions are being removed from the

bulk electrolyte to form double layers, this would lead to increased CO₂ solubility in the bulk electrolyte since the solubility of CO₂ is decreasing with increasing ionic strength [201]. When the half-submerged electrode was working as the cathode pressure drops could be observed but when the same electrode was working as the anode the pressure was increasing. This suggests that the SSA effect is not due to changes in the solubility of the CO₂ in the electrolyte since it would be expected to see similar pressure drops no matter whether the gas-exposed electrode is working as the cathode or the anode. However, since CO₂ tends to be salted out of NaCl solutions and the amount of the dissolved CO₂ in the aqueous electrolytes is significant, this mechanism contributes to some extent and cannot be ruled out. Since the salting-out effect depends on various factors such as the charge and radius of the ions, the salt concentration, temperature and the static dielectric constant of the solvent [202], it is clear that more experiments are required to clarify the full mechanism of the SSA effect. Therefore, in the future, it is necessary to do experiments with various aqueous electrolytes which have different radii of the ions. It would be interesting for example to compare aqueous NaCl, KCl, and CaCl₂ at different concentrations.

8. Summary and Conclusions

8.1. Summary

In this dissertation a novel and simple technique, supercapacitive swing adsorption, for carbon dioxide adsorption and separation is described. It is shown that in this technique adsorption and desorption of CO₂ can be accomplished by the reversible charge and discharge of high surface area carbon supercapacitor electrodes which are in contact with the gas phase and an aqueous 1M sodium chloride electrolyte. This process requires no temperature and pressure changes, because adsorption and desorption are controlled only by capacitive charge and discharge of supercapacitive HSAC electrodes. It is proven that the electric double layer formed during the charge of the carbon electrodes is necessary for the SSA effect. The results of the experiments show that SSA has the ability to successfully separate CO₂ from N₂. Moreover, there is a high selectivity of CO₂ over N₂ and He gas and little dependence on the CO₂ partial pressure in a 15% CO₂/85% N₂ gas mixture. The presented results show also that CO₂ can be reversibly adsorbed and desorbed depending on the direction of applied bias and this effect is only weakly dependent on the temperature. During cathodic charging of the half-submerged electrode adsorption of CO₂ is possible. When the system was charged, the sorption capacity of CO₂ went up, leading to a pressure drop and when the system was discharged, the sorption capacity dropped, causing the system pressure to rise higher. On the other hand the anodic charging can harness the “native” high adsorptivity of HSA BPL carbon sorbents for CO₂, and desorb adsorbed CO₂. The adsorption property of activated BPL carbon is changed without chemical modification. The SSA effect scales approximately proportionally with the amount of used sorbent material. Hence, the SSA technique may be scalable to the

industrial scale and could help reduce the emissions from fossil fuel power plants. Furthermore, SSA may be potentially extended to other gas system because it is doubtful that the SSA effect is only restricted to CO₂.

8.2. Results of SSA experiments vs. hypotheses of SSA

It was possible to link very high capacitance and high adsorption affinity for CO₂ properties of activated carbon material in the implementation of SSA for carbon dioxide capture. The reversible adsorption/desorption behavior of carbon dioxide can be controlled by charging and discharging of the capacitive system

Moreover, calculations in Chapter 5 showed that a significant fraction of the BPL carbon pore surface area is covered by ions from electrolyte in the charged state which can affect the sorption behavior of a significant number of CO₂ molecules. The results of SSA experiments confirmed the calculations since the sorption capacity of CO₂ went up during cathodic charging, and when the system was discharged, the sorption capacity dropped.

Further, size and/or direction of the effect really depends on the electrode character (anode vs. cathode) because the structures of both double layers are different. Adsorption of CO₂ during cathodic charging and desorption of CO₂ during anodic charging was observed.

Finally, competitive anode/cathode effects was observed due to the asymmetric configuration of the two BPL carbon electrodes, in which one electrode was partially submerged in an electrolyte while the other one was fully submerged in the electrolyte so it could not directly interact with the CO₂ in the gas phase.

8.3. Conclusions

The SSA effect is reversible and selective for CO₂ over N₂. The SSA effect scales with the mass of the sorbent material. An important fact is that SSA achieves the gas adsorption in the presence of water what shows that the technique is insensitive to water vapor in the gas mixture.

There are several aspect which can have a significant impact on the SSA effect. First, SSA can be applicable to a variety of different sorbent materials because the only basic requirement for the sorbent is electrical conductivity, high surface area and high equilibrium loading for CO₂ gas what can be applicable to many carbon materials and also for some other materials including metal-organic frameworks which can be electrically conducting and can have higher equilibrium loadings for CO₂ in comparison to the BPL carbon.

Another impact on the magnitude of the SSA effect could be in the chemical nature and concentration of the electrolyte. The electrolyte determines the capacitance and also the degree of infiltration of the HSAC electrodes. In this work only 1 M NaCl was used therefore it would be interesting to see how the SSA effect will change with concentration of the electrolyte. Also, it will be interesting to compare various aqueous electrolytes which will have different radius of the ions.

From Figure 7.3 the charge-discharge energy efficiency was calculated according to equations 4.8a and 4.8b and was equal to 42% at 10 mA (22.2 J was used for charging and 9.5 J was recovered upon discharging) constant current and 74% at 2 mA (33.1 J was used for charging and 24.4 J was recovered upon discharging) constant current. This calculations

allowed us to calculate the parasitic load of SSA which can be correlated with the charge-discharge energy difference (33.1 J- 24.4 J = 8.7 J) and the measured pressure changes (16 Torr at 2 mA constant current). By using equations 8-1 and 8-2 the energy penalty of 2.1 GJ/ton CO₂ can be calculated and this value is comparable to energy penalties for amine-based systems which are at this moment the most developed systems for carbon capture [203]:

$$n = \frac{PV}{RT} = \frac{16.00 \text{ Torr} \times 0.11 \text{ L mol K}}{62.36 \text{ L Torr} \times 299.75 \text{ K}} = 9.42 \times 10^{-5} \text{ mol} = 0.094 \text{ mmol} \quad \text{Equation 8-1}$$

in which P is the pressure change, V is the volume of the SSA cell filled with gas, R is gas constant (8.314 J K⁻¹ mol⁻¹ = 62.364 L Torr K⁻¹ mol⁻¹) and T is temperature inside of the cell which is equal to temperature of the room in which experiment was carried on (26.6⁰C = 299.75K). Further, the energy penalty (E) can be calculated (1 mol of CO₂ = 44.01 g of CO₂):

$$E = \frac{8.7 \text{ J}}{0.094 \text{ mmol}} = \frac{92.6 \text{ J}}{\text{mmol}} = \frac{92.6 \text{ kJ}}{\text{mol}} = \frac{92.6 \text{ kJ}}{44.0 \text{ g}} = \frac{2.1 \text{ kJ}}{\text{g}} = \frac{2.1 \text{ GJ}}{\text{t}} \quad \text{Equation 8-2}$$

Since an average CO₂ emission for US coal fired power plants = 1 ton per 3.6 GJ of energy generated [1], the parasitic load here is 58.3%:

$$\text{parasitic load} = \frac{2.1 \text{ GJ}}{3.6 \text{ GJ}} \times 100\% = 58.3\% \quad \text{Equation 8-3}$$

It needs to be considered that the SSA system has relatively low charge-discharge energy efficiencies. Commercially available supercapacitors can be charged and discharged within seconds at energy efficiencies larger than 95% what suggests that SSA can be still optimized. The major reason for the relatively low charge-discharge energy efficiency is due to high ESR of our capacitive system. One of the reasons why the ESR is higher for

prepared capacitor is the electrically insulating PVDF binder which was used for preparation of carbon pellets and monoliths. This binder not only increases the internal resistivity of the capacitor but also reduces the charge-discharge energy efficiency. Electrodes used for SSA experiments have large distance and a large thickness which is not ideal from the standpoint of ionic resistivity. These arguments show that there is strong potential that the parasitic load of SSA can be still decreased.

References

1. EIA (Energy Information Administration), 2013. International Energy Outlook 2013. <http://www.eia.gov/forecasts/ieo/index.cfm>, accessed April 9th, 2014.
2. S. A. Rackley, Carbon Capture and Storage, *Elsevier* (2010).
3. IPCC. Climate Change 2001: Impacts, Adaptation and Vulnerability (2001).
4. J. F. B. Mitchell, The greenhouse effect and climate change, *Reviews of Geophysics*, **27** (1), 115–139 (1989)
5. T. S. Ledley, E. T. Sundquist, S. E. Schwartz, D. K. Hall, J. D. Fellows, T. L. Killeen, Climate change and greenhouse gases, *Eos, Transactions American Geophysical Union*, **20** (39), 453–458 (1999).
6. C. Stewart, M.-A. Hessami, A study of methods of carbon dioxide capture and sequestration - the sustainability of a photosynthetic bioreactor approach, *Energy Conversion and Management*, **46** (3), 403-420 (2005)
7. M. Beychok, Fossil fuel combustion flue gases, *Encyclopedia of Earth*, 2012 (<http://www.eoearth.org/view/article/171355/>, accessed on April 18th, 2014).
8. H. Yang, Z. Xu, M. Fan, R. Gupta, R. Slimane, A. Bland, et al., Progress in carbon dioxide separation and capture: A review. *J Environ Sci.*, **20** (1), 14-27 (2008)
9. IPCC, Carbon Dioxide Capture and Storage. *Cambridge University Press*, p. 431 (2005).
10. IEA (International Energy Agency), *Technology Roadmap: Carbon capture and storage*; 2009.
11. R.J. Hook, An Investigation of Some Sterically Hindered Amines as Potential Carbon Dioxide Scrubbing Compounds. *Ind. Eng. Chem. Res.* **36**, 1779 -1790 (1997).
12. J. T. Yeh, H. W. Pennline, K. P. Resnik, Study of CO₂ Absorption and Desorption in a Packed Column. *Energy & Fuels*, **15**, 274-278 (2001).
13. C. Alie, L. Backham, E. Croiset, P. L. Douglas, Simulation of CO₂ capture using MEA scrubbing: a flowsheet decomposition method. *Energy Conversion and Management*, **46** (3), 475-487 (2005).
14. L. M. Romeo, I. Bolea, I. J. Escosa, Integration of power plant and amine scrubbing to reduce CO₂ capture costs. *Applied Thermal Engineering*, **28** (8-9), 1039-1046 (2008).
15. S. P. Reynolds, A. D. Ebner, J. A. Ritter, New pressure swing adsorption cycles for carbon dioxide sequestration. *Adsorption*, **11** (1) Suppl., 531-536 (2005).
16. M. T. Ho, G. W. Allinson, D. E. Wiley, Reducing the cost of CO₂ capture from flue gases using pressure swing adsorption, *Ind. Eng. Chem. Res.*, **47** (14), 4883-4890 (2008).

17. J. Zhang, P. A. Webley, Cycle development and design for CO₂ capture from flue gas by vacuum swing adsorption. *Environmental Science and Technology*, **42** (2), 563 – 569 (2008).
18. A. J. Mason, K. Sumida, Z. R. Herm, R. Krishna and J. R. Long, Evaluating metal–organic frameworks for post-combustion carbon dioxide capture via temperature swing adsorption, *Energy Environ. Sci.*, **4**, 3030-3040 (2011).
19. C. A. Grande, R. P. P. L. Ribeiro and A. E. Rodrigues, CO₂ Capture from NGCC Power Stations using Electric Swing Adsorption (ESA), *Energy Fuels*, **23** (5), pp 2797–2803 (2009).
20. A. Olajire, CO₂ capture and separation technologies for end-of-pipe applications - A review. *Energy*, **35**, 2610-2628 (2010).
21. J. Figuerola, T. Fout, S. Plasynski, H. McIlvried, R. Srivastava, Advances in CO₂ capture technology-The U.S. Department of Energy's Carbon Sequestration Program. *International Journal of Greenhouse Gas Control*, **2** (1), 9-20 (2008).
22. A. B. Rao and E. S. Rubin, A Technical, Economic, and Environmental Assessment of Amine-Based CO₂ Capture Technology for Power Plant Greenhouse Gas Control, *Environ. Sci. Technol.* **36** (6), 4467-4475 (2002).
23. G. T. Rochelle, Amine Scrubbing for CO₂ Capture, *Science*, **325**, 1652–1654 (2009).
24. R.W. Baker, and K. Lokhandwala, Natural Gas Processing with Membranes: An Overview, *Ind. Eng. Chem. Res.*, **47** (7), 2109-2121 (2008).
25. M.T. Ho, G. Allison, and D.E. Wiley, Comparison of CO₂ separation options for geo-sequestration: are membranes competitive?, *Desalination*, **192** (1-3), 288-295 (2006).
26. E. Favre, Carbon Dioxide recovery from post-combustion processes: Can gas permeation membranes compete with absorption?, *Journal of Membrane Science*, **294** (1-2), 50-59 (2007).
27. H. Yang, S. Fan, X. Lang, Y. Wang, J. Nie, Economic comparison of three gas separation technologies for CO₂ capture from power plant flue gas, *Chinese Journal of Chemical Engineering*, **19** (4), 615-620 (2011).
28. Ch.-H. Yu, Ch.-H. Huang, Ch.-S. Tan, A Review of CO₂ Capture by Absorption and Adsorption, *Aerosol and Air Quality Research*, **12**, 745–769 (2012).
29. IPCC, Carbon Dioxide Capture and Storage. *Cambridge University Press*, p. 442 (2005).

30. J. Junga, Y. S. Jeonga, Y. Lima, Ch. S. Leeb, Ch. Hana, Advanced CO₂ Capture process using MEA scrubbing: Configuration of a Split Flow and Phase Separation Heat Exchanger, *Energy Procedia*, **37**, 1778 – 1784 (2013).
31. P.E. Fanta, Amine, In *AccessScience, McGraw-Hill Companies*, Available from: www.accessscience.com/content/Amine/028000 (accessed on April 18th 2014).
32. B. Eliasson, P. Riemer, A. Wokaun, Greenhouse Gas Control Technologies, *Elsevier*, first edition, page 102 (1999)
33. P. V. Danckwerts, The Reaction of Carbon Dioxide with Ethanolamines, *Chem. Engr. Sci.*, **34**, 443 (1979).
34. M. Radosz, X. Hu , K. Krutkramelis , and Y. Shen, Flue-Gas Carbon Capture on Carbonaceous Sorbents: Toward a Low-Cost Multifunctional Carbon Filter for “Green” Energy Producers, *Ind. Eng. Chem. Res.*, **47** (10), 3783–3794 (2008).
35. S. Freguia, G. Rochelle, Modeling of CO₂ capture by aqueous monoethanolamine, *AIChE Journal*, **49** (7), 1676-1686 (2003).
36. D. D'Alessandro, T. McDonald, Toward carbon dioxide capture using nanoporous materials, *Pure Applied Chemistry*, **83** (1), 57-66 (2011).
37. A. Veawab, A. Aroonwilas, A. Chakma, P. Tontiwachwuthikul. Solvent Formulation for CO₂ Sequestration from Flue Gas Streams. Faculty of Engineering, University of Regina, Regina, Saskatchewan, Canada
38. J.A. Kent, Kent and Riegel’s Handbook of Industrial Chemistry and Biotechnology, Volumes 1 & 2 (11th edition), *Springer-Verlag*, NY, USA, p 1876 (2007).
39. CH. Hsu, H. Chu, C. M. Cho, Absorption and reaction kinetics of amines and ammonia solutions with carbon dioxide in flue gas, *J. Air & Waste Manage. Assoc.* **53** 246-252 (2003).
40. Y. Zhang, Z.Z. Li, X. Li, J. X. Dong, and Y. Wang, Experimental study on sequestration of CO₂ in the true flue gas by ammonia spray producing NH₄HCO₃, *The fifth international symposium on coal combustion*, 562-566 (2003).
41. J. T. Yeh, K. P. Resnik, K. Rygle, H. W. Pennline, Semi-batch absorption and regeneration studies for CO₂ capture by aqueous ammonia, *Fuel Processing Technology*, **86**, 1533-1546 (2005).
42. K. P. Resnik, J. T. Yeh and H. W. Pennline, Aqua ammonia process for simultaneous removal of CO₂, SO₂ and NO_x, *Int. Environmental Technology and Management*, **4**, 89-104 (2004).

43. H. Bai, A.C. Yeh, Removal of CO₂ Greenhouse gas by ammonia scrubbing, *Ind. Eng. Chem. Res.*, **36** (6), 2490-2494 (1997).
44. J. T. Yeh, K. P. Resnik, K. Rygle, H. W. Pennline, Absorption and Regeneration Studies for CO₂, *Proceedings of Third Annual Conference on Carbon Capture & Sequestration*, Alexandria, VA. U.S. DOE – NETL and Parson Project Services, Inc., 6 June 2004, Web. 13 Nov. 2010.
45. K. P. Resnik, W. Garber, D. Hreha, J. T. Yeh, H. W. Pennline, A parametric scan for regenerative ammonia-based scrubbing for the capture of CO₂, *Proceedings of 23rd Annual International Pittsburgh Coal Conference* (2006).
46. H.E. Howe, Manufacture of Carbon Dioxide, *Ind. Eng. Chem. Res.*, **20** (10), 1091-1094 (1928).
47. D. H. Killeffer, Absorption of Carbon Dioxide, *Ind. & Eng. Chem.*, **29** (11), 1293 (1937).
48. I. Langmuir, The adsorption of gases on plane surfaces of glass, mica and platinum, *The Journal of the American Chemical Society*, **40** (9), 1361–1403 (1918)
49. M. Polanyi, Section III.—theories of the adsorption of gases: a general survey and some additional remarks. Introductory paper to section III, *Transactions of the Faraday Society*, **28**, 316–333 (1932).
50. A. L. Myers and J. M. Prausnitz, Thermodynamics of mixed-gas adsorption, *AIChE Journal*, **11**, 121–127 (1965).
51. D. M. Ruthven, Principles of Adsorption and Adsorption Processes, *John Wiley & Sons*, New York, NY, USA (1984).
52. R. T. Yang, Adsorbents. Fundamentals and Applications, *John Wiley & Sons*, New Jersey, NJ, USA (2003).
53. P. C. Wankat, Large-Scale Adsorption and Chromatography, *CRC Press*, Boca Raton, Fla, USA (1986).
54. A. E. Rodrigues, M. D. LeVan, and D. Tondeur, Adsorption, Science and Technology, *Kluwer Academic Publishers*, Boston, Mass, USA (1989).
55. M. Suzuki, Adsorption Engineering, Chemical Engineering Monographs, *Elsevier*, Tokyo, Japan (1990).
56. J. Kärger and D. M. Ruthven, Diffusion in Zeolites and Other Microporous Solids, *John Wiley & Sons*, London, UK (1992).
57. C. Tien, Adsorption Calculations and Modeling, *Butterworth-Heinemann*, Boston, Mass, USA (1994).

58. D. Basmadjian, *The Little Adsorption Book: A Practical Guide for Engineers and Scientists*, CRC Press, Boca Raton, Fla, USA (1997).
59. J. L. Humphrey and G. E. Keller, *Separation Process Technology*, McGraw-Hill, New York, NY, USA (1997).
60. D. D. Do, *Adsorption Analysis: Equilibria and Kinetics*, Imperial College Press, London, UK (1998).
61. J. W. Thomas and B. D. Crittenden, *Adsorption Technology and Design*, Elsevier, Boston, Mass, USA (1998).
62. O. Talu, Needs, status, techniques and problems with binary gas adsorption experiments, *Advances in Colloid and Interface Science*, **76-77**, 227–269 (1998).
63. F. Rouquerol, J. Rouquerol, and K. Song, *Adsorption by Powders and Porous Solids*, Academic Press, London, UK (1999).
64. Z. Zhao, X. Cui, J. Ma, R. Li, Adsorption of carbon dioxide on alkali-modified zeolite 13X adsorbents, *International Journal of Greenhouse Gas Control*, **1**, 355-359 (2007).
65. M.G. Plaza, S. García, F. Rubiera, J.J Pis and C. Pevida, Post-Combustion CO₂ Capture with a Commercial Activated Carbon: Comparison of Different Regeneration Strategies. *Chem. Eng. J.*, **163**, 41–47 (2010).
66. Q. Wang, J. Luo, Z. Zhong and A. Borgna, CO₂ Capture by Solid Adsorbents and Their Applications: Current Status and New Trends. *Energy Environ. Sci.* **4**, 42–55 (2011).
67. J.-R. Lia, Y. Mab, M. C. McCarthyb, J. Sculleya, J. Yub, H.-K. Jeongb, P. B. Balbuenab, H.-C. Zhou, Carbon dioxide capture-related gas adsorption and separation in metal-organic frameworks, *Coordination Chemistry Reviews*, **55** (15–16), 1791–1823 (2011).
68. A. Sayari, Y. Belmabkhout, R. Serna-Guerrero, Flue gas treatment via CO₂ adsorption. *Chemical Engineering Journal*, **171** (3), 760-774 (2011).
69. A. Samanta, A. Zhao, G. K. H. Shimizu, P. Sarkar, R. Gupta, Post-Combustion CO₂ Capture Using Solid Sorbents: A Review. *Industrial & Engineering Chemistry Research*, **51** (4), 1438-1463 (2012).
70. M.S. Shafeeyan, W.M.A. Wan Daud, A. Houshmand, A. Arami-Niya, The application of response surface methodology to optimize the amination of activated carbon for the preparation of carbon dioxide adsorbents, *Fuel*, **94**, 465-472 (2012).
71. C. Pevida, M.G. Plaza, B. Arias, J. Feroso, F. Rubiera, and J.J. Pis, Surface modification of activated carbons for CO₂ capture, *Applied Surface Science*, **254** (22), 7165-7172 (2008).

72. Z.H. Lee, K.T. Lee, S. Bhatia, and A.R. Mohamed, Post-combustion carbon dioxide capture: Evolution towards utilization of nanomaterials, *Renewable and Sustainable Energy Reviews*, **16** (5), 2599-2609 (2012)
73. M. G. Plaza, C. Pevida, B. Arias, J. Feroso, F. Rubiera, and J.J. Pis, A comparison of two methods for producing CO₂ capture adsorbents, *Energy Procedia*, **1** (1), 1107-1113 (2009).
74. K. S. Knaebel and F. B. Hill, Pressure swing adsorption: development of an equilibrium theory for gas separations, *Chemical Engineering Science*, **40** (12), 2351–2360 (1985).
75. M. D. LeVan, Pressure swing adsorption: equilibrium theory for purification and enrichment, *Industrial and Engineering Chemistry Research*, **34** (8), 2655–2660 (1995).
76. G. Pigorini and M. D. LeVan, Equilibrium theory for pressure swing adsorption. 2: purification and enrichment in layered beds, *Industrial and Engineering Chemistry Research*, **36** (6), 2296–2305 (1997).
77. G. Pigorini and M. D. LeVan, Equilibrium theory for pressure swing adsorption. 3: separation and purification in two-component adsorption, *Industrial and Engineering Chemistry Research*, **36**, (6), 2306–2319 (1997).
78. G. Pigorini and M. D. LeVan, Equilibrium theory for pressure-swing adsorption. 4: optimizations for trace separation and purification in two-component adsorption, *Industrial and Engineering Chemistry Research*, **37** (6), 2516–2528 (1998).
79. H. W. Habgood, The kinetics of molecular sieve action: sorption of nitrogen-methane mixtures by Linde Molecular Sieve 4A, *Canadian Journal of Chemistry*, **36**, 1384–1397 (1958).
80. K. Chihara, M. Suzuki, and K. Kawazoe, Adsorption rate on molecular sieving carbon by chromatography, *AIChE Journal*, **24** (2), 237–246 (1978).
81. H. Jüntgen, K. Knoblauch, and K. Harder, Carbon molecular sieves: production from coal and application in gas separation, *Fuel*, **60** (9), 817–822 (1981).
82. A. Kapoor and R. T. Yang, Kinetic separation of methane-carbon dioxide mixture by adsorption on molecular sieve carbon, *Chemical Engineering Science*, **44** (8), 1723–1733 (1989).
83. F. Rezaei and P. Webley, Optimum structured adsorbents for gas separation processes, *Chemical Engineering Science*, **64** (24), 5182–5191 (2009).
84. P. Cen and R. T. Yang, Separation of a five-component gas mixture by pressure swing adsorption, *Separation Science and Technology*, **20** (9-10), 725–747 (1985).
85. T. Golden, J. Hufton, R. Quinn, Air Products and Chemicals, Inc. *13th NICHE Conference* October 13 (2008) (<http://www.canadiancleanpowercoalition.com/pdf/> - Accessed on April 15th 2014).

86. S. Sircar, Fractionation of multicomponent gas mixtures by pressure swing adsorption, *U.S. patent* **4**, 790, 858 (1988).
87. T. C. Golden, R. Kumar, and W. C. Kratz, Hydrogen purification, *US patent* **4**, 957, 514 (1990).
88. C. W. Skarstrom, Method and apparatus for fractionating gas mixtures by adsorption, *U.S. Patent* **2**, 944, 627 (1960).
89. M. T. Ho, G. W. Allinson and D. E. Wiley, Reducing the Cost of CO₂ Capture from Flue Gases Using Pressure Swing Adsorption, *Ind. Eng. Chem. Res.*, **47** (14), 4883–4890 (2008).
90. A. Malek and S. Farooq, Hydrogen purification from refinery fuel gas by pressure swing adsorption, *AIChE Journal*, **44** (9), 1985–1992 (1998).
91. J. Stöcker, M. Whysall, and G. Q. Miller, 30 Years of PSA Technology for Hydrogen Purification, *UOP LLC*, Des Plaines, Ill, USA (1998).
92. C. H. Lee, J. Yang, and H. Ahn, Effects of carbon-to-zeolite ratio on layered bed H₂ PSA for coke oven gas, *AIChE Journal*, **45** (3), 535–545 (1999).
93. S. Sircar, W. E. Waldron, M. B. Rao, and M. Anand, Hydrogen production by hybrid SMR-PSA-SSF membrane system, *Separation and Purification Technology*, **17** (1), 11–20 (1999).
94. J. H. Park, J. N. Kim, and S. H. Cho, Performance analysis of four-bed H₂ PSA process using layered beds, *AIChE Journal*, **46** (4), 790–802 (2000).
95. S. Sircar and T. C. Golden, Purification of hydrogen by pressure swing adsorption, *Separation Science and Technology*, **35** (5), 667–687 (2000).
96. C. W. Skarstrom, Method and apparatus for fractionating gas mixtures by adsorption, *U.S. patent* **2**, 944, 627 (1960).
97. N. H. Berlin, Method for providing an oxygen-enriched environment, *U.S. Patent* **3**, 280, 536 (1966).
98. H. Jüntgen, K. Knoblauch, J. Reichenberger, and F. Tarnow, Process for the recovery of nitrogen-rich gases from gases containing at least oxygen as other component, *U.S. patent* **4**, 264, 339 (1981).
99. D. M. Ruthven, N. S. Raghavan, and M. M. Hassan, Adsorption and diffusion of nitrogen and oxygen in a carbon molecular sieve, *Chemical Engineering Science*, **41** (5), 1325–1332 (1986).
100. C. G. Coe, J. F. Kirner, R. Pierantozzi, and T. R. White, Nitrogen adsorption with Ca and or Sr exchanged lithium X-zeolites, *U.S. patent* **5**, 152, 813 (1992).

101. J. G. Jee, J. S. Lee, and C. H. Lee, Air separation by a small-scale two-bed medical O₂ pressure swing adsorption, *Industrial and Engineering Chemistry Research*, **40** (16), 3647–3658 (2001).
102. Y. Lü, S. J. Doong, and M. Bülow, Pressure-swing adsorption using layered adsorbent beds with different adsorption properties: II-experimental investigation, *Adsorption*, **10** (4), 267–275 (2005).
103. J. C. Santos, A. F. Portugal, F. D. Magalhães, and A. Mendes, Optimization of medical PSA units for oxygen production, *Industrial and Engineering Chemistry Research*, **45** (3), 1085–1096 (2006).
104. R. L. Bec, Method for purifying hydrogen-based gas mixtures using calcium X-zeolite, *U.S. patent* 6, 849, 106 (2005).
105. J. S. D'amico, H. E. Reinhold III, and K. S. Knaebel, Helium recovery, *U.S. patent*, 5, 542, 966 (1996).
106. N. K. Das, H. Chaudhuri, R. K. Bhandari, D. Ghose, P. Sen, and B. Sinha, Purification of helium from natural gas by pressure swing adsorption, *Current Science*, **95** (12), 1684–1687 (2008).
107. A. P. G. Taveira and A. M. M. Mendes, Xenon external recycling unit for recovery, purification and reuse of xenon in anesthesia circuits, *U.S. patent* 7, 442, 236 (2008).
108. J. D. Seader, Ernest J. Henley, D. Keith Roper, Separation Process Principles, 3rd Edition, *John Wiley & Sons*, p.610 (2010)
109. M.-B. Kim, J.-H. Moon, C.-H. Lee, H. Ahn, W. Cho, Effect of heat transfer on the transient dynamics of temperature swing adsorption process, *Korean Journal of Chemical Engineering*, **21**, 703-711 (2004).
110. J. Bonjour, J.-B. Chalfen, F. Meunier, Temperature swing adsorption process with indirect cooling and heating, *Industrial & Engineering Chemistry Research*, **41** (23), 5802-5811 (2002).
111. A. Subrenat and P. Le Cloirec, Thermal Behavior of Activated Carbon Cloths Heated by Joule Effect, *Journal of Environmental Engineering-Asce* **129** (12) 1077-1084 (2003).
112. P. D. Sullivan, M. J. Rood, K. J. Hay, and S. Qi, Adsorption and Electrothermal Desorption of Hazardous Organic Vapors, *Journal of Environmental Engineering-Asce* **127** (3) 217-223 (2001).
113. P. D. Sullivan, M. J. Rood, G. Grevillot, J. D. Wander, and K. J. Hay, Activated Carbon Fiber Cloth Electrothermal Swing Adsorption System, *Environmental Science & Technology*, **38** (18) 4865-4877 (2004).
114. C. A. Grande, R. P. P. L. Ribeiro, A. E. Rodrigues, CO₂ Capture from NGCC Power Stations using Electric Swing Adsorption (ESA), *Energy Fuels* **23**, 2797-2803 (2009).

115. H. An, B. Feng and S. Su, CO₂ Captured by Electrothermal Swing Adsorption with Activated Carbon Fibre Materials, *Int. J. Greenhouse Gas Control*, **5**, 16–25 (2011).
116. C. A. Grande, R. P. L. Ribeiro, E. L. G. Oliveira, A. E. Rodrigues, Electric swing adsorption as emerging CO₂ capture technique, *Energy Procedia*, **1**, 1219–1225 (2009).
117. S. Prakash, Physics Vol (1 and 2), third revised edition, p.365 (2006) (accessed through books.google.com/books?isbn=8188597317 on April 30th, 2014).
118. R.N. Place, A.J. Blackburn, S.R. Tennison, A.P. Rawlinson, B.D. Crittenden, Method and Equipment for Removing Volatile Compounds from Air. *US patent 6*, 964, 695 (2005).
119. R.R. Judkins, T.D. Burchell, Electrical swing adsorption gas storage and delivery system, *US Patent 5*, 912, 424 (1999).
120. J.P. Farant, G. Desbiens, Adsorption of contaminants from gaseous stream and in situ regeneration of sorbent, *US patent 7*, 316, 731 (2008).
121. F.D. Yu, L. Luo, G. Grevillot, Electrothermal swing adsorption of toluene on an activated carbon monolith. Experiments and parametric theoretical study. *Chem. Eng. Process.* **46**, 70–81 (2006).
122. L. Luo, D. Ramirez, M. J. Rood, G. Grevillot, K. J. Hay, D. L. Thurston, Adsorption and electrothermal desorption of organic vapors using activated carbon adsorbents with novel morphologies. *Carbon* **44**, 2715 – 2723 (2006).
123. C. A. Grande, A. E. Rodrigues, Electric Swing Adsorption for CO₂ Removal from Flue Gases. *Int. J. Green. Gas Control*, **2**, 194-202 (2008).
124. N. Ettlili, S. Bertelle, D. Roizard, C. Vallieres, G. Grevillot, A New Electrical Swing Adsorption Process for Post-Combustion CO₂ Capture, *Proceedings of the 8th International Conference on Greenhouse Gas Control Technologies*, Elsevier (2006).
125. B. R. Strazisar, R. R. Anderson, and C. M. White, Degradation of Monoethanolamine Used in Carbon Dioxide Capture from Flue Gas of a Coal-fired Electric Power Generating Station, *Proceedings of First National Conference on Carbon Sequestration*, Washington, DC (2001).
126. B.E. Conway, Electrochemical Supercapacitors: Scientific Fundamentals and Technological Applications, *Kluwer Academic*, NY (1999).
127. M. Winter, R.J. Brodd, What Are Batteries, Fuel Cells, and Supercapacitors?, *Chemical Reviews*, **104** (10), 4245-4270 (2004).
128. <http://commons.wikimedia.org/wiki/File:Supercapacitors-Overview.png> (Accessed on June 2nd, 2014).

129. P. Simon and A. Burke, Nanostructured Carbons: Double-Layer Capacitance and More, *The electrochemical society interface*, **17** (1), 38-43 (2008).
130. R. Kotz and M Carlen, Principles and applications of electrochemical capacitors, *Electrochimica Acta*, **45** (15–16), 2483–2498 (2000).
131. H. I. Becker, Low voltage electrolytic capacitor, *United States Patent* 2800616 (1957).
132. M. Endo, T. Takeda, Y. J. Kim, K. Koshiba, K. Ishii, High power electric double layer capacitor (EDLC's): from operating principle to pore size control in advanced activated carbons, *Carbon Sci.*, **1**, 117-128 (2001).
134. P. Sharma, T. S. Bhatti, A review on electrochemical double-layer capacitors, *Energy Convers. Manage.*, **51**, 2901-2912 (2010).
135. F. Béguin, E. Frackowiak. Carbons for Electrochemical Energy Storage and Conversion Systems. CRC Press, Boca Raton, 2010, pp 329-373 & 454-463.
136. A. Nishino, Capacitors: operating principles, current market and technical trends, *Journal of power sources*, **60**, 137-147 (1996).
137. J. T. Zhang, X. S. Zhao, On the configuration of supercapacitors for maximizing electrochemical performance, *ChemSusChem*, **5**, 818-841 (2012).
138. E. Frackowiak, Carbon materials for supercapacitor application, *Phys. Chem. Chem. Phys.*, **9**, 1774-1785 (2007).
139. M.J. Sparnaay, The electric double layer, *Pergamon Press* (Australia) Pty. Ltd., vol. 4, 1st ed., Sydney (1972).
140. P. P. Barker, Power Engineering Society Summer Meeting, 2002 IEEE, p. 316 (2002)
141. V. Obreja, On the performance of supercapacitors with electrodes based on carbon nanotubes and carbon activated material-A review, *Physica E.*, **40**, 2596-2605 (2008).
142. M. Matsumoto, Electrocapillarity and double layer structure, from H. Ohshima, & K. Furusawa, Electrical phenomena at interfaces: fundamentals, measurements, and applications, vol. 76, *Surfactant science series*, 2nd ed. New York: Marcel Dekker, Inc., pp. 87-99 (1998).
143. F.C.Wu, R.L. Tseng, C.C. Hu, C.C.Wang, The capacitive characteristics of activated carbons - comparisons of the activation methods on the pore structure and effects of the pore structure and electrolyte on the capacitive performance, *J. Power Sources*, **159**, 1532-1542 (2006).
144. J.G. Lee, J.Y. Kim, S.H. Kim, Effects of microporosity on the specific capacitance of polyacrylonitrile based activated carbon fiber, *J. Power Sources*, **160** (2), 1495-1500 (2006).

145. H. Teng, Y. J. Chang, C. T. Hsieh, Performance of electric double-layer capacitors using carbons prepared from phenol–formaldehyde resins by KOH etching, *Carbon*, **39** (13), 1981-1987 (2001).
146. R.C. Bansal, J.B. Donnet, H.F. Stoeckli, Active Carbon, Active Carbon, *Marcel Dekker, Inc.*, New York (1988).
147. D. Lozano-Castelló, D. Cazorla-Amorós, A. Linares-Solano, Powdered Activated Carbons and Activated Carbon Fibers for Methane Storage: A Comparative Study, *Energy & Fuels*, **16** (5), 1321-1328 (2002).
148. P. Davini, P., Flue gas treatment by activated carbon obtained from oil-fired fly ash, *Carbon*, **40** (11), 1973-1979 (2002).
149. M.M. Maroto-Valer, Z. Tang, Y. Zhang, CO₂ capture by activated and impregnated anthracites, *Fuel Processing Technology*, **86** (14–15), 1487-1502 (2005).
150. Y. Wang, Y. Zhou, C. Liu, L. Zhou, Comparative studies of CO₂ and CH₄ sorption on activated carbon in presence of water. *Colloids and Surfaces A: Physicochemical and Engineering Aspects*, **322** (1–3), 14-18 (2008).
151. S. Choi, J. Drese, C. Jones, Adsorbent materials for carbon dioxide capture from large anthropogenic point sources, *ChemSusChem*, **2**, 796-854 (2009).
152. K.S.W. Sing, D.H. Everett, R.A.W. Haul, L. Moscou, R.A. Pierotti, J. Rouquerol, and T. Siemieniewska, Reporting physisorption data for gas/solid systems with special reference to the determination of surface area and porosity (recommendations 1984), *Pure and Applied Chemistry*, **57** (4), 603–619 (1985).
153. F. Rodríguez-Reinoso, The role of carbon materials in heterogeneous catalysis, *Carbon*, **36**, 159-175 (1998).
154. A. Ahmadpour, D.D. Do, The preparation of active carbons from coal by chemical and physical activation, *Carbon*, **34** (4), 471-479 (1996).
155. M.J.B. Evans, E. Halliop, J.A.F. McDonald, The production of chemically- activated carbon, *Carbon*, **37** (2), 269-274 (1999).
156. K. Kinoshita, Carbon - Electrochemical and Physicochemical Properties, *John Wiley & Sons Inc.*, New York (1988).
157. K. S. W. Sing, Reporting Physisorption Data for gas/solid Systems with Special Reference to the Determination of Surface Area and Porosity, *Pure & Appl. Chem.*, **54** (11), 2201 - 2218 (1982).
158. R.M.A. Roque-Malherbe, Adsorption and Diffusion in Nanoporous Materials, *CRC Press*, page 94 (2007).

159. I. Langmuir, The adsorption of gases on plane surfaces of glass, mica and platinum, *J.Am.Chem.Soc.*, **40** (9), 1361 – 1403 (1918).
160. S. Brunauer, P. H. Emmett, E. Teller, Adsorption of Gases in Multimolecular Layers, *Journal of the American Chemical Society*, **60** (2), 309-319 (1938).
161. W.A. Steele, G. Zgrablich, W. Rudzinski, Equilibria and Dynamics of Gas Adsorption on Heterogeneous Solid Surfaces, *Elsevier*, page 6 (1996) (online edition accessed on July 6th, 2014 http://books.google.com/books?id=BuPg3Oayi48C&pg=PA6&dq=hypothesis+of+BET+theory+adsorption&hl=en&sa=X&ei=W_i-U4PSMMq3yAS4s4CgCQ&ved=0CCwQ6AEwAw).
162. K. D. Hammond, W. Curtis Conner Jr., *Advances in Catalysis*, *Academic Press*, first edition, page 26 (2013).
163. E.P. Barrett, L.G. Joyner, and P.P. Halenda, The determination of pore volume and area distributions in porous substances. I. Computations from nitrogen isotherms, *Journal of the American Chemical Society*, **73**, 373—380 (1951).
164. J.I. Goldstein, D.E. Newbury, P. Echlin, *Scanning Electron Microscopy and X-ray Microanalysis*, Plenum Press, New York and London, 2nd edition (1992).
165. W. Zhou, Z.L. Wang, *Scanning Microscopy for Nanotechnology*, *Springer*, New York, pp. 1–40 (2006)
166. K.C.A. Smith, C.W. Oatley, The scanning electron microscope and its fields of application, *British Journal of Applied Physics*, **6** (11), 391–399 (1955).
167. L. Reimer, *Scanning Electron Microscopy: Physics of Image Formation and Microanalysis*, *Springer Series in Optical Sciences*, **45**, pp. 207–233 (1998).
168. P.J. Grundy, G.A. Jones, *Electron microscopy in the study of materials*, *Edward Arnold Publishers*, London (1976).
169. G. Lawes, *Scanning electron microscopy and X-ray microanalysis: Analytical chemistry by open learning*, *John Wiley & sons* (1987).
170. <http://www4.nau.edu/microanalysis/microprobe-sem/instrumentation.html> (Accessed on May 25th, 2014)
171. L. Reimer, H. Kohl, *Transmission Electron Microscopy*, Springer, 5th edition, pp. 1–10, 419–425 (2008).
172. C. Kisielowski, et. Al., Detection of Single Atoms and Buried Defects in Three Dimensions by Aberration-Corrected Electron Microscope with 0.5-Å Information Limit, *Microscopy and Microanalysis*, **14** (5), 469–477 (2008).

173. M.A. O’Keefe, L.F. Allard, D.A. Blom, HRTEM Imaging of Atoms at Sub-Angstrom Resolution, *Journal of Electron Microscopy*, **54** (3), 169–180 (2005).
174. D. B. Williams and C. B. Carter, Transmission Electron Microscopy, *Springer*, 2nd edition (2009).
175. R. Egerton, Physical principles of electron microscopy, *Springer*, 1st edition (2005).
176. J.C.H. Spence, High-Resolution Electron Microscopy, *Oxford University Press*, NY (1988)
177. L.C. Sawyer, D.T. Grubb, G.F. Meyers, Polymer Microscopy, *Springer*, NY (2008).
178. http://en.wikipedia.org/wiki/File:Scheme_TEM_en.svg (Accessed on May 29th, 2014).
179. J. Wang, Analytical Electrochemistry, *VCH Publishers*, NY, page 1 (1994).
180. R. Compton and C. Banks, Understanding Voltammetry, *World Scientific Publishing Co. Inc.*, Singapore (2007).
181. <http://www.gamry.com/application-notes/two-three-and-four-electrode-experiments/> (Accessed on June 1st, 2014).
182. <http://www.gamry.com/application-notes/testing-electrochemical-capacitors-part-1-cyclic-voltammetry-and-leakage-current/> (Accessed on June 1st, 2014).
183. X. Zhao, H. Tian, M. Zhu, K. Tian, J.J. Wang, F. Kang, and R. A. Outlaw, Carbon nanosheets as the electrode material in supercapacitors, *Journal of Power Sources*, **194**, 1208-1212 (2009).
184. E. Frackowiak, F. Beguin, Carbon materials for the electrochemical storage of energy in capacitors, *Carbon*, **39** (6), 937-950 (2001).
185. <http://www.gamry.com/application-notes/testing-electrochemical-capacitors-part-2-cyclic-charge-discharge-and-stacks/> (Accessed on June 5th, 2014).
186. B.E. Conway and W.G. Pell, Power limitations of supercapacitor operation associated with resistance and capacitance distribution in porous electrode devices, *Journal of Power Sources*, **105**, p. 196 (2002).
187. International Electrotechnical Commission (IEC) 62391-2-1, 1st edition (2006).
188. A. G. Pandolfo, A.F.Hollenkamp, Carbon properties and their role in supercapacitors, *J Power Sources*, **157**, 11-27 (2006).
189. http://www.lehigh.edu/~inano/emf_facility.html (Accessed on May 25th, 2014).
190. Y. Zhong, J. Zhang, G. Li, A. Liu, Research on Energy Efficiency of Supercapacitor Energy Storage System. *International Conference on Power System Technology*, 1-4 (2006).

191. L. Demarconnay, E. Raymundo-Piñero, F. Béguin, A symmetric carbon/carbon supercapacitor operating at 1.6 V by using a neutral aqueous solution, *Electrochem. Commun.*, **12**, 1275-1278 (2010).
192. M. P. Bichat, E. Raymundo-Piñero, F. Béguin, High voltage supercapacitor built with seaweed carbons in neutral aqueous electrolyte, *Carbon*, **48**, 4351-4361 (2010).
193. Q. T. Qu, B. Wang, L. C. Yang, Y. Shi, S. Tian, Y. P. Wu, Study on electrochemical performance of activated carbon in aqueous Li₂SO₄, Na₂SO₄ and K₂SO₄ electrolytes, *Electrochem. Commun.*, **10**, 1652-1655 (2008).
194. K. Fic, G. Lota, M. Meller, E. Frackowiak, Novel insight into neutral medium as electrolyte for high-voltage supercapacitors, *Energy Environ. Sci.*, **5**, 5842-5850 (2012).
195. V. Khomenko, E. Raymundo-Pinero, F. Beguin, Optimisation of an asymmetric manganese oxide/activated carbon capacitor working at 2 V in aqueous medium, *J. Power Sources*, **153** (1), 183-190 (2006).
196. L. Demarconnay, E. Raymundo-Pinero, F. Beguin, Adjustment of electrodes potential window in an asymmetric carbon/MnO₂ supercapacitor, *J. Power Sources*, **196**, 580-586 (2011).
197. J.H. Chae, G.Z. Chen, 1.9 V aqueous carbon-carbon supercapacitors with unequal electrode capacitances, *Electrochim. Acta*, **86**, 248-254 (2012).
198. A. Kaithwas, M. Prasad, A. Kulshreshtha, S. Verma, Industrial wastes derived solid adsorbents for CO₂ capture: A mini review, *Chemical Engineering Research and Design*, **90**, 1632-1641 (2012).
199. C. Masarapu, H.F. Zeng, K. H. Hung, B. Wei, Effect of Temperature on the Capacitance of Carbon Nanotube Supercapacitors, *ACS Nano*, **3**, 2199-2206 (2009).
200. S. I. Fletcher, F. B. Sillars, R. C. Carter, A. J. Cruden, M. Mirzaeian, N. E. Hudson, J. A. Parkinson, P. J. Hall, The Effects of Temperature on the Performance of Electrochemical Double Layer Capacitors, *J. Power Sources*, **195**, 7484-7488 (2010).
201. S. Bando, F. Takemura, M. Nishio, E. Hihara, M. Akai, Solubility of CO₂ in aqueous solutions of NaCl at (30 to 60) degrees C and (10 to 20) MPa, *J. Chem. Eng. Data* **48**, 576-579 (2003).
202. Y. Liu, M. Hou, G. Yang, B. Han, Solubility of CO₂ in aqueous solutions of NaCl, KCl, CaCl₂ and their mixed salts at different temperatures and pressures, *The Journal of Supercritical Fluids*, **56** (2), 125-129 (2011).
203. M. Abu-Zahra, L. Schneiders, J. Niederer, P. Feron, G. Versteeg, CO₂ capture from power plants. Part I. A parametric study of the technical-performance based on monoethanolamine, *International Journal of Greenhouse Gas Control*, **1**, 37-46 (2007).

204. Union of Concerned Scientists (UCSUSA),
http://www.ucsusa.org/clean_energy/coalvswind/c02c.html#.VHdghzHF8sA (Accessed
on November 15th, 2014).

205. M.M. Maroto-Valer, Z. Tang, Y. Zhang, CO₂ capture by activated and impregnated anthracites, *Fuel Processing Technology*, **86**, 1487-1502 (2005).

Appendix A

1. The gas/vapor sorption properties of the BPL carbon electrode materials

The measured N₂ isotherm (Figure A1) belongs to type IV, as defined by IUPAC and showed mesoporous structure of BPL carbon with mainly micropores at 0.4nm and mesoporous ranging from 2 to 4nm and with a surface area close to 640 m²/g of material. A CO₂ adsorption isotherm was measured in order to check the CO₂ uptake (how much CO₂ can be adsorbed per gram of material) on BPL carbon. The CO₂ isotherms were measured at 4 different temperatures: 273 K, 298 K, 323 K and 343 K. It was observed that BPL carbon shows diminished sorption capacities at higher temperature (Figure A2). The equilibrium CO₂ adsorption capacity of BPL carbon increased as the temperature decreased giving 66 cm³ of CO₂ adsorbed per gram of BPL carbon at 0 °C, 31 cm³/g at 25 °C, 19 cm³/g at 50 °C and 11 cm³/g at 70 °C. This is due to the fact that increase in the temperature excited the internal energy of the adsorbent which tends to release the CO₂ molecules present on the adsorbent. Maroto-Valer *et al.* [205] reported that physisorption process involves high surface adsorption energy and molecule diffusion at elevated temperatures, which results in instability of the adsorbed gas on the surface of activated carbon and consequently, the desorption process will occur.

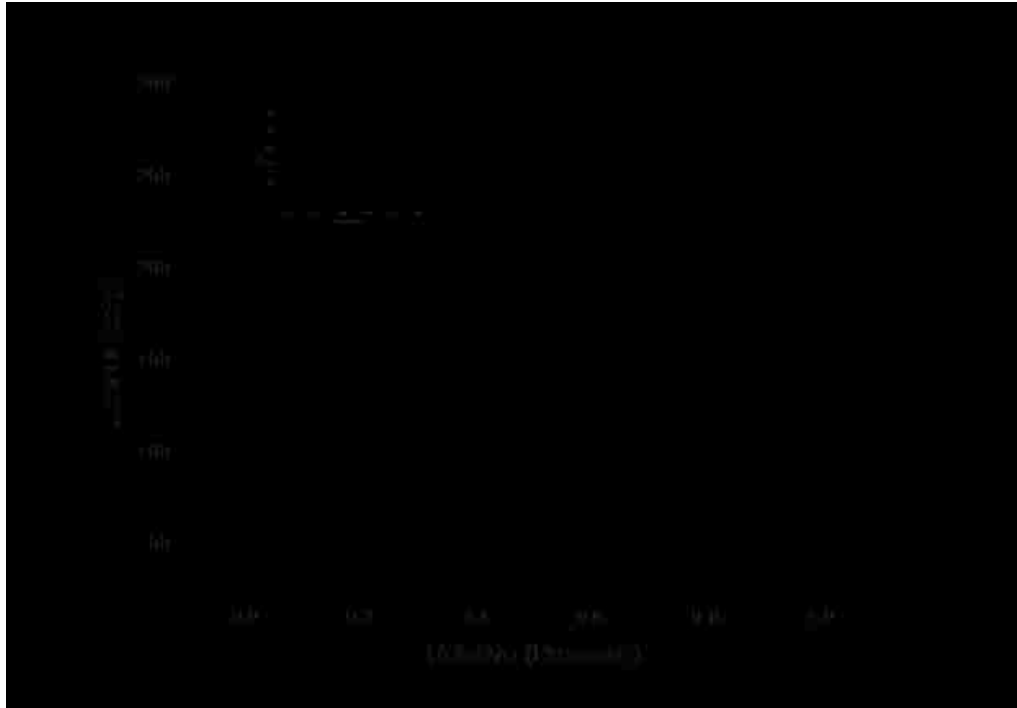


Figure A1. N_2 isotherm of BPL carbon at 77 K (inset: pore size distribution).

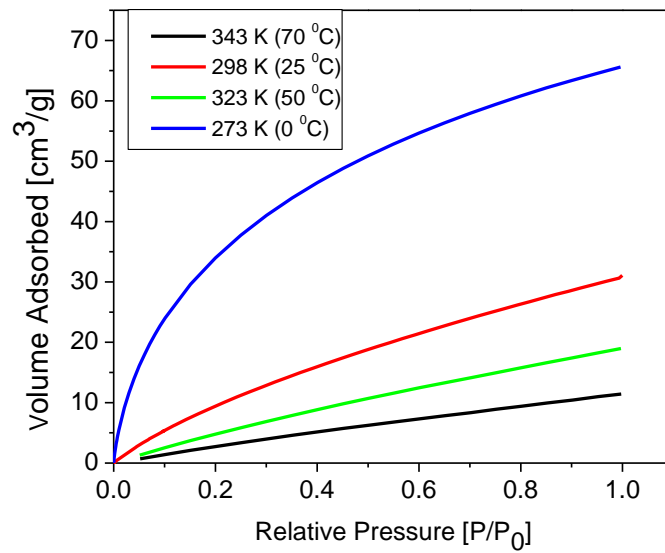


Figure A2. CO_2 adsorption isotherm for BPL HSAC electrodes at three different temperatures.

2. TEM images of BPL carbon

TEM was used to examine the microstructure of the BPL carbon electrode materials prepared for SSA experiments which showed both mesopores and micropores (Figure A3). The results of TEM analyses were consistent with the results of nitrogen adsorption isotherm analysis and confirmed the porous structure of the electrode material.

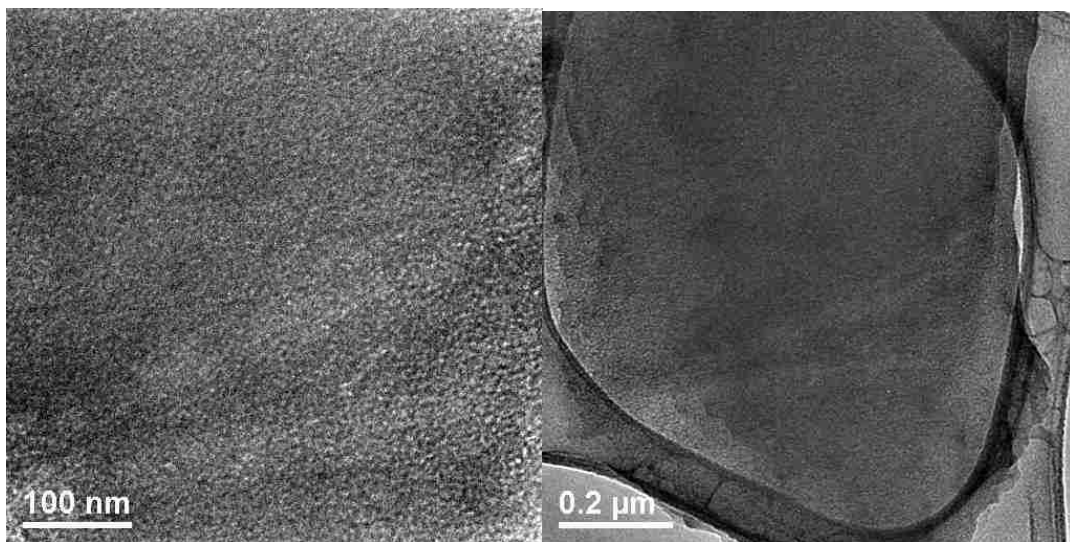


Figure A3. TEM images of BPL carbon.

3. Electrochemical characterization of the BPL carbon electrodes.
 - a) Cyclic Voltammetry (CV)

Cyclic Voltammetry experiments done in a two-electrode configuration confirmed the capacitive behavior of the BPL carbon electrodes prepared for the SSA experiments (static pressure experiments). Since higher scan rate creates lower capacitances, here mostly slow 1 mV/s scan rate was chosen in order to get the full capacitance of the HSAC electrodes. The scan rate must be low to record full capacitance because there are slow electrode processes in the “inner” surface of the BPL carbon electrode pores.

Figure A4 shows typical CV curves measured for the BPL carbon pellets and monoliths prepared for the SSA experiments. It can be seen from this figure that resistance causes a slow rise in the current and rounds two corners of the rectangle at the beginning of the charge and discharge process. The voltammogram adopts a more slanting shape and the current over the potential window is no longer constant. Ideal double-layer capacitance through CV is represented by a rectangle within a voltammetry plot of the current with respect to applied potential as illustrated in Figure 4.5. However prepared supercapacitors deviate slightly from this relation due to diffusion resistances in the initial charging or discharging process of the double-layer for the respective voltage limit.

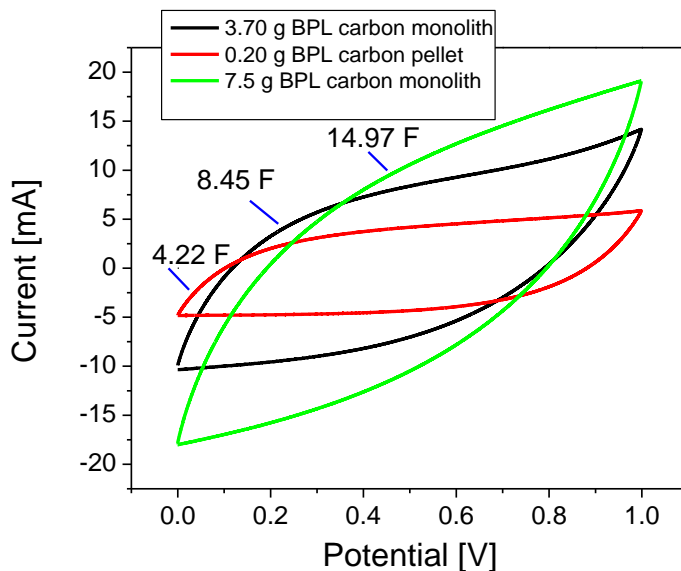


Figure A4. Cyclic Voltammetry curves of 0.20 g BPL carbon pellet (red curve), 3.70 g BPL carbon monolith (black curve) and 7.5 g BPL carbon monoliths (green curve) measured in 1 M NaCl solution at 1 mV/s scan rate from 0V to 1.0V without reference electrode (full cell set up); the counter electrode had the same mass as the working electrode.

b) Galvanostatic Charge-Discharge (GCD)

Galvanostatic Charge-Discharge experiments done in a two-electrode configuration also confirmed the capacitive behavior of the BPL carbon electrodes prepared for the SSA experiments.

Appendix B

1. Method used for the calculation of energy efficiency.

Energy calculations from CCD experiments

$$E_{\text{charge}} = I \times V \times t \text{ [A} \times \text{V} \times \text{s} = \text{J]}$$

$$E_{\text{discharge}} = I \times V \times t \text{ [A} \times \text{V} \times \text{s} = \text{J]}$$

a) CCD at 10mA constant current (cathodic cycle)

$$E_{\text{charge}} = 0.01 \text{ A} \times 2224.07 \text{ Vs} = 22.24 \text{ J} = 6.18 \text{ mWh}$$

$$E_{\text{discharge}} = 0.01 \text{ A} \times 950.83 \text{ Vs} = 9.51 \text{ J} = 2.64 \text{ mWh}$$

$$\text{Efficiency} = 42.72 \%$$

b) CCD at 2mA constant current (0V to 1V) (cathodic cycle)

$$E_{\text{charge}} = 0.002 \text{ A} \times 16539.36 \text{ Vs} = 33.08 \text{ J} = 9.19 \text{ mWh}$$

$$E_{\text{discharge}} = 0.002 \text{ A} \times 12182.44 \text{ Vs} = 24.36 \text{ J} = 6.77 \text{ mWh}$$

$$\text{Efficiency} = 73.67 \%$$

2. Method used to determine relationship between pressure and composition change

As can be seen a 0.93% composition change correlates to a pressure change of 7 Torr.

$$pV = nRT \Rightarrow \Delta n = \frac{\Delta pV}{RT} = \frac{7.00 \times 10^5}{62.36 \times 299.75} \left[\frac{\text{mmHg} \times \text{ml}}{\frac{\text{ml} \times \text{mmHg}}{\text{K} \times \text{mmol}} \times \text{K}} = \text{mmol} \right]$$

$$\Delta n = 3.93 \times 10^{-2} \text{ mmol} \quad (\text{for } \text{CO}_2 \text{ gas})$$

- in the beginning of first cycle: $p = 835 \text{ Torr}$ (mix of CO_2 and N_2)

$$\Delta n = \frac{835 \times 10^5}{62.36 \times 299.75} = 4.69 \text{ mmol}$$

$$\begin{array}{rcl}
 4.62 \text{ mmol} & - & 100\% \text{ of gas mixture} \\
 x \text{ mmol} & - & 15\% \text{ of } CO_2
 \end{array}
 \rightarrow x = 0.70 \text{ mmol of } CO_2$$

$$\Delta CO_2 = 0.70 \text{ mmol} - 3.93 \times 10^{-2} \text{ mmol} = 0.66 \text{ mmol}$$

$$\# \text{mmol of } N_2 = 85\% \times 4.69 = 3.99 \text{ mmol}$$

$$\%CO_2 = \frac{0.66}{0.70 + 3.99} \times 100\% = 14.07\%$$

$$\Delta CO_2 = 15\% - 14.07\% = 0.93\%$$

Where:

V – Volume of the SSA cell filled with gas

R – gas constant ($8.314 \text{ J K}^{-1} \text{ mol}^{-1} = 62.364 \text{ L mmHg K}^{-1} \text{ mol}^{-1}$)

T – temperature inside of the cell which is equal to temperature of the room where experiment was carried on ($26.6^\circ\text{C} = 299.75\text{K}$)

Berenika Kokoszka
84.agnes@gmail.com

EDUCATION

2012 – 2015	Lehigh University, Department of Chemistry, Bethlehem, PA – Ph.D. degree since May 2015
2010 - 2012	Lehigh University, Department of Chemistry, Bethlehem, PA – MS degree since January 2012
2003 – 2008	Warsaw University, Department of Chemistry, Warsaw, Poland - MS degree since April 2008

EXPERIENCE

Research Assistant at Lehigh University (January 2011 to Present)

- Research performed under Professor Kai Landskron.
- Design, synthesis and characterization of electrodes for carbon capture project (ARPA-E financial support).
- Synthesis and characterization of organic-inorganic hybrid nanoporous materials for gas sorption and separation.
- Ph.D. Thesis title: Supercapacitive Swing Adsorption of Carbon Dioxide.

Teaching Assistant at Lehigh University (January 2010 to Present)

- TA for physical chemistry lab
Responsibilities included: grading lab reports and notebooks, running lab practice, monitor students during lab, tutoring students;
- TA for organic lab
Responsibilities included: grading lab reports and notebooks, running lab practice, monitor students during lab, tutoring students.

Research Assistant at Warsaw University (April 2007 – April 2008)

- Research performed under Professor Pawel Kulesza.
- Preparation and characterization of tungsten oxide electrodes for direct ethanol fuel cells application.
- Master's Thesis title: Preparation and characterization of micro- and nanostructured tungsten oxide films on electrodes.

INTERESTS

Electrochemistry, photochemistry, fuel cells and catalysts for them, photovoltaic cells, lithium batteries, nanotechnology, nanomaterials, nanoparticles and carbon nanotubes, surface analysis by different techniques (SEM, TEM), electrocatalysis and modified electrodes

LANGUAGES

- Polish (native)

- English (fluent)

EXTRA CURRICULAR

- Member of American Chemical Society (ACS) (since October 2010).
- Participated in the “242nd ACS National Meeting & Exposition”, August 28-September 1, 2011, Denver, Colorado (poster session in inorganic chemistry division).
- Participated in the “2011 NETL CO2 Capture Technology Meeting”, August 23-25, 2011, Pittsburgh, PA (poster session).
- Participated in the “16th Northeast Corridor Zeolite Association Annual Meeting”, December 14, 2012, Philadelphia, PA (poster session).
- Microporous and Mesoporous Materials, Volume 152, 1 April 2012, Pages 214-218 (second author).
- Angew. Chem. Int. Ed. 53, 2014, Pages 1 – 5 (first author).